UNCLASSIFIED

AD 260 428

Reproduced
by the

ARMED SERVICES TECHNICAL INFORMATION AGENCY
ARLINGTON HALL STATION
ARLINGTON 12, VIRGINIA

UNCLASSIFIED

NOTICE: When government or other drawings, specifications or other data are used for any purpose other than in connection with a definitely related government procurement operation, the U. S. Government thereby incurs no responsibility, nor any obligation whatsoever; and the fact that the Government may have formulated, furnished, or in any way supplied the said drawings, specifications, or other data is not to be regarded by implication or otherwise as in any manner licensing the holder or any other person or corporation, or conveying any rights or permission to manufacture, use or sell any patented invention that may in any way be related thereto.

AD-260428

BMI-2774-FR-Sep 59
Cy HI-2
1

RESEARCH REPORT

LOAN COPY
Property of
Technical Documents Library
Army Ballistic Missile Agency
DO NOT DESTROY

RECEIVED
8 FEB 1960
TECHNICAL DOCUMENTS LIBRARY

ASTIA
RECEIVED
JUL 27 1961
TIPDR

BATTELLE
MEMORIAL INSTITUTE

FINAL REPORT

on

INVESTIGATION OF HIGH-SPEED PARTICLE EROSION OF MELTING AERODYNAMIC SURFACES

to the

ARMY BALLISTIC MISSILE AGENCY

September 15, 1959

by

E. W. Ungar

Performed Under
Contract No. DA-33-019-ORD-2774

BATTELLE MEMORIAL INSTITUTE
505 King Avenue
Columbus 1, Ohio

ACKNOWLEDGMENTS

The test firings conducted on this program were carried out at the Army Ballistic Missile Agency under the direction of J. Cain. The ABMA technical supervisor for the over-all program was D. L. Burrows. The following people are responsible for the work conducted at Battelle Memorial Institute: B. Steginsky and R. A. Stein worked on the analysis of particle impaction; A. E. Weller worked on the initial review of solid-propellant rocket-engine facilities; R. A. Duffee prepared the cloud data presented; C. Hyde and H. D. Sheets assisted in the determination of material properties and the preparation of test specimens; A. A. Putnam provided provocative comments; J. M. Allen, Project Leader, and F. L. Bagby, Division Chief, were in charge of coordination and administrative direction, respectively.

ABSTRACT

The impact of atmospheric moisture particles on ablating hypersonic bodies was studied experimentally and theoretically. Various factors involved in the simulation of impacts with atmospheric-moisture particles during re-entry are discussed. The phenomena was studied experimentally in a rocket exhaust jet using small solid and liquid particles to simulate atmospheric moisture. Factors which could not be simulated in the rocket-exhaust-jet tests were analyzed theoretically. The experimental data were correlated using a mechanism based on the dissipation of particle energy in the melt layer. The results were extrapolated to the conditions of atmospheric re-entry. The results indicate that the ablation rate on a nose cone following a 3000 NM trajectory increases by a factor of 2 during flight through a cloud as a result of impacts with fine ice particles or water droplets.

TABLE OF CONTENTS

TABLE OF CONTENTS
(Continued)

INVESTIGATION OF HIGH-SPEED PARTICLE EROSION OF MELTING AERODYNAMIC SURFACES

by

E. W. Ungar

INTRODUCTION

The re-entry portion of a ballistic missile is subject to extreme heating during passage through the atmosphere. The extent of this heating, which results from dissipation of vehicle potential and kinetic energies, depends on the range of the missile and the weight-to-drag ratio of the re-entry vehicle. The nose of the re-entry vehicle is generally blunted, so that a large amount of vehicle energy is dissipated by heating the air behind a detached shock wave. However, there still may be sufficient energy transferred from the hot gas behind the detached shock wave to the re-entry body to vaporize most materials. Thus, a thermal protection system is required such that the interior of the nose cone remains at a sufficiently low temperature level to allow operation of the equipment contained therein.

Three types of thermal protection system that are considered to be effective are (1) an ablating system, (2) a heat-sink system, and (3) a transpiration cooling system. The most promising of these three systems appears to be the ablating system. In this system, the interior of the re-entry body is protected from the effect of heat transfer from the hot shock-layer gas by the controlled loss of mass from a relatively thin surface coating. The mass loss may result from either (1) melting, (2) sublimation, (3) melting and subsequent boiling, (4) chemical degradation, or (5) oxidation. Furthermore, composite materials may be used in the ablating system that combine two or more of the types of loss listed. The ablation of surface material protects the interior of the nose cone by one or more of the following processes: (1) by utilizing a large portion of the transferred energy to heat liquid or gaseous products of the ablation process; (2) by decreasing the enthalpy gradients in the gaseous boundary layer; and (3) by increasing the radiation from the hot surface layers to the surrounding environment.

A number of studies have been made in recent years to determine design criteria for ablating nose-cone systems under ideal atmospheric conditions. The success of these studies is indicated by the results of recent flight tests and the present operational status of the Jupiter missile. The problem considered in the present investigation is connected with the re-entry of a nose cone under nonideal atmospheric conditions, that is, the effect on an ablating nose-cone system of flight through clouds. The atmospheric-moisture particles that make up these clouds might impact on the nose-cone surface with large relative kinetic energies. The effect of these impacts might be to increase the ablation rate to such an extent that the interior temperature of the vehicle will exceed the limit for reliable operation of the equipment contained within. Furthermore, the increased rate of ablation might occur at nose-cone locations where only small amounts of material loss would be expected otherwise. In an extreme situation, the geometry of the nose cone might be altered sufficiently by particle impacts to affect the accuracy of the missile's flight path. On the other extreme, the effect of the

particles might be to cool the nose-cone surface, resulting in a net decrease in the ablation rate. A study of the vulnerability of a re-entry body to the effects of particle impact also has significant implications for the field of missile countermeasures.

This report begins with a description of the nature of the problem of atmospheric-moisture-particle impacts on a melting surface, followed by a discussion of similarity considerations for simulation of flight phenomena. This is succeeded by a general analysis of various test facilities, and a detailed description of the ABMA 3.5 AHT facility. This is followed by a discussion of the experimental program, the presentation of test results, and a correlation of the data. A discussion of failure mechanisms comes after this presentation of test results. Then various factors involved in the application of the test results to flight conditions are considered; these include particle-impaction efficiencies, water-droplet evaporation in the shock layer, water-droplet breakup in the shock layer, scaling of the liquid-melt layer thickness, and particle heat-sink effects. The results of calculations of particle effects are presented for both a 3000-NM and a 500-NM ballistic trajectory in order to indicate the magnitude of the effect that might be expected in flight.

SUMMARY OF RESULTS

Aerodynamically shaped nose-cone specimens were exposed in the particle-laden exhaust of the ABMA 3.5 AHT engine which burns a mixture of hydrogen peroxide and kerosene. This engine has been modified to allow the injection of a particle-kerosene slurry. Both liquid and solid particles, with average sizes ranging from 6 to 88 microns, were used in the experiments. The majority of the tests were conducted by using Micarta 259-2 as a specimen material, although supplementary tests were conducted by using a calcium aluminate material, a silica material, and a ceramic, Mix 785, developed by Battelle for ABMA. The Micarta 259-2 was chosen for consideration because it is representative of the reinforced plastics in current use.

The test results indicated that the erosion rate of Micarta specimens exposed to a particle-laden hot-gas stream increases with both particle size and concentration in a nonlinear manner. In some instances, the particles inflicted severe damage on the Micarta test specimens. These results were correlated on the basis of a melt-protection mechanism; that is, it was assumed that the particles dissipate a portion of their kinetic energy within the melt layer. Thus, the melt layer to some extent, protects the surface of the nose cone from particle-impact effects, and the extent of this protection depends on the melt-layer thickness and density. The experimental data indicate that this correlation is applicable to both liquid and solid particles.

Theoretical studies were carried out to determine the factors controlling impaction efficiency, droplet breakup in the shock layer, and droplet evaporation in the shock layer. These studies indicated that it is reasonable to assume an impaction efficiency of 100 per cent, and to neglect breakup and evaporation of droplets in the shock layer when order-of-magnitude estimates of particle effects in free flight are being made. Additional study of these factors would be required in order to obtain detailed design data, but these additional studies were beyond the scope of this program.

The liquid-melt-layer thickness was found to be important when considering impact effects; thus, it became necessary to estimate the average melt thickness in free flight. A means of doing this on the basis of rocket exhaust tests was developed, and this method was applied to Micarta 259-2 along two representative ballistic trajectories.

The cooling effect of atmospheric-moisture particles on the ablating body was analyzed within a first-order-approximation. The thermal history of the droplet had to be assumed in order to estimate the decrease in the heat flux to the ablating body due to droplet cooling. Additional studies of droplet-cooling effects would be required in order to obtain good estimates of the effect of droplet cooling on the ablation rate, but these studies were beyond the scope of this program.

Impact effects on free-flight missiles were calculated by using the relations developed in this program. An analysis of a 3000-NM trajectory showed that the ablation rate may be increased, under some conditions, by as much as a factor of 2 during flight through a cloud. Similar calculations showed that the total amount of material ablated along a severe 500-NM trajectory would be increased by almost 8 per cent as a result of flight through a nimbostratus cloud.

OBJECTIVES OF PROGRAM

The principal objectives of this program were (1) to determine the magnitude of the increased erosion of melting aerodynamic bodies resulting from the impact upon these bodies of particles simulating atmospheric moisture, (2) to determine and utilize a test facility which is suitable for use in studying such effects and (3) to extrapolate the results to flight trajectories in order to obtain at least a nominal indication of the magnitude of the particle erosion problem for melting bodies.

NATURE OF THE PROBLEM

A body re-entering the atmosphere along a ballistic trajectory generally is preceded by a detached shock wave. Figure 1 is a schematic sketch of the flow system under consideration. During flight through a cloud, the body encounters atmospheric-moisture particles in the size range from 2 to 100 microns. The relative velocity between the particles and the body is essentially the flight velocity of the body. The particles first feel the presence of the re-entry vehicle when they encounter the bow shock wave. The particles suddenly penetrate the shock wave and enter the shock layer, which to the particle consists of high-velocity, high-temperature air.

The high relative velocity between the particles and the shock-layer gas leads to aerodynamic forces that tend to deflect and decelerate the particles relative to the body and also to disintegrate the particles. Because the shock layer is thin and the initial particle velocity relative to the missile is high, the time during which the particles remain in the shock layer is short, being of the order from 10 to 100 microseconds. Thus, the aerodynamic forces act on the particles for only a short period of time.

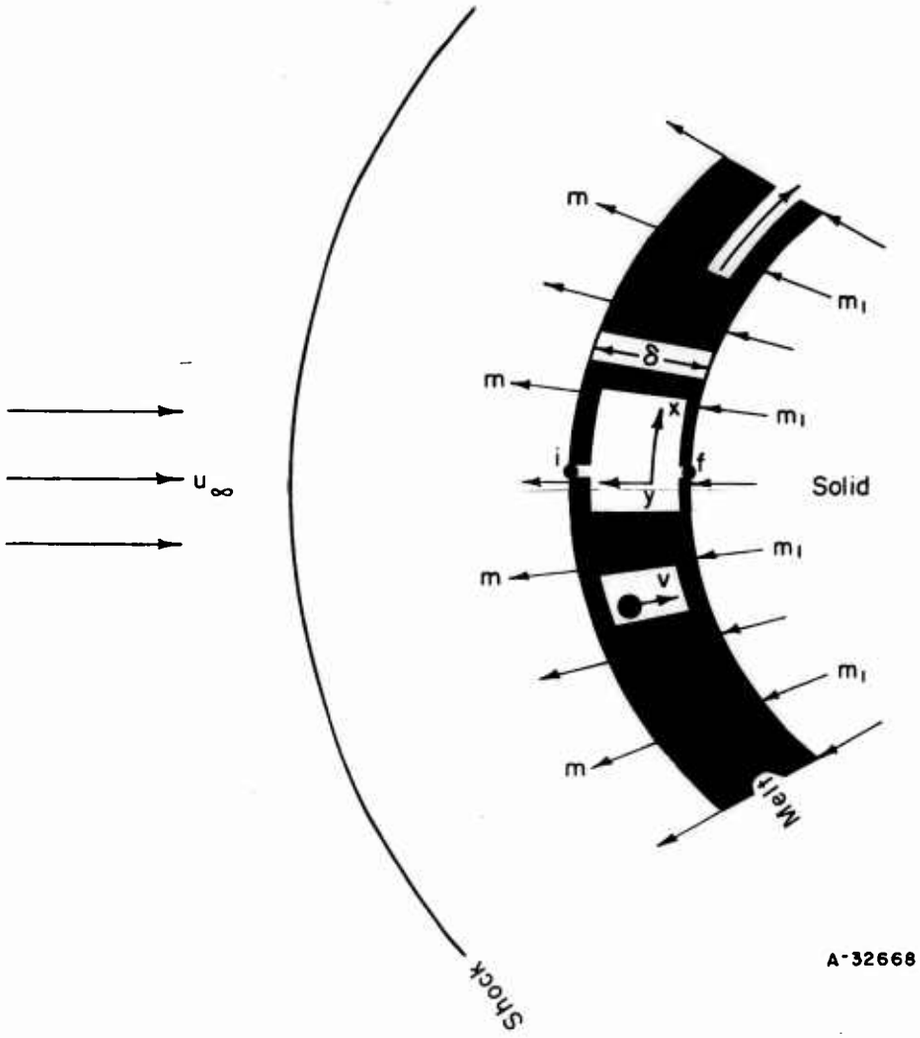

FIGURE 1. SCHEMATIC MODEL OF THE ABLATING SYSTEM

Dimensions in the y direction are exaggerated.

If the particles are in the form of compact ice crystals or if the shock-layer residence time is found to be insufficient for the breakup of liquid droplets, it becomes necessary to determine the fraction of the particles that cross the shock wave, but are not deflected sufficiently by aerodynamic forces to miss the body. This fraction is referred to as the impaction efficiency. Hence, the impaction efficiency is the ratio of the number of particles that hit a selected region of the body to the number of particles ahead of the shock wave in the projected area of the selected region. The energy that these particles transmit to the body depends on their impact velocity, this, in turn, depends on their initial velocity and the deceleration of the particles due to aerodynamic forces in the shock layer.

The high shock-layer temperatures are more than sufficient to vaporize the droplets. It is necessary, therefore, to determine whether sufficient time is available for droplet evaporation in the shock layer. Ideally, the mass evaporated from the droplet and the diameter of the droplet at the time it impacts the body should be determined. For an order-of-magnitude analysis, however, it is sufficient to determine only the relative importance of droplet-evaporation phenomena.

After passing through the shock layer, the particles impact on the liquid-melt layer. The melt layer is generally of the order of several particle diameters thick. The particles are deformed and decelerated by the liquid melt as they penetrate the melt layer, and thus lose a large amount of their energy relative to the re-entry body. This energy loss is such a large fraction of the initial kinetic energy of the particle that it must be accounted for in detail. In fact, the energy dissipation in the melt layer is believed to be the most important single factor involved in the evaluation of particle-impact effects.

After passage through the melt layer, the particle strikes the solid body beneath. The particle imparts the residual kinetic energy not dissipated in the melt to the solid material, causing damage to the body. In the case of Micarta 259-2, it is believed that the particle energy increases the rate of decomposition of the plastic, thus increasing the ablation rate of the entire system.

It should also be noted that the particle impacts affect the heat flux to the body. This can occur in any of several ways, such as (1) a decrease in heat flux due to gas evolved from the plastic decomposed by particle impacts, (2) a cooling effect produced by the evaporation of the droplet following impact, and (3) an undetermined effect resulting from the disturbance of the liquid melt produced by droplet penetration.

Thus, it is evident that particle impacts on an ablating body lead to a complex phenomena of interactions with the thermal protection system. All of these phenomena are discussed in more or less detail in this report depending on their importance to the over-all effect of particles on ablation and also depending on the relative ease with which the phenomena could be analyzed. The investigation reported herein thus, represents, an initial investigation of the effects produced by small-particle impacts on a melting aerodynamic body.

SIMILARITY BETWEEN TEST AND FLIGHT CONDITIONS

As is evident from the preceding discussion, many parameters influence the effect of atmospheric particles on an ablating re-entry body. These parameters must all be considered in the simulation of high-speed-particle impacts on a melting surface in a laboratory device. In fact, to reproduce the physical phenomena accurately, each parameter would have to be simulated. This would necessitate firing a full-scale ballistic missile such that it would re-enter the atmosphere in a location with a known cloud composition. As this is not considered to be practical under the scope of this investigation, the relative importance of each parameter must be determined, and a laboratory exposure scheme must be developed in which the important parameters are properly controlled. The problem of simulation may be subdivided conveniently into three separate categories: (1) the flow field and thermal environment with respect to the nose cone, (2) the flow field with respect to the particle, and (3) the physical effect of the particle on the melting nose cone. Each of these categories is discussed.

Flow Field With Respect to the Nose Cone

The re-entry body under discussion is considered to be traveling along a ballistic trajectory. Thus, the flow conditions vary, in general, as a function of time from those of hypersonic flight to possibly subsonic flight. Because impacts with cloud elements are being considered, considerations were limited to altitudes of less than 40,000 feet. For a severe ballistic trajectory, which is representative of second-generation IRBM's, hypersonic flight is maintained even at altitudes less than 40,000 feet. The discussion that follows is concerned with simulation of a hypersonic flight condition. Simulation of the flow field about the nose cone can be achieved if the following are simulated: (1) Mach number, (2) Reynolds number, (3) properties of high-temperature air, and (4) nose-cone geometry.

The Mach number determines the shock-detachment-distance ratio, λ/R, and influences the pressure and velocity gradients in the shock layer. The shock-detachment-distance ratio decreases rapidly at first, and then slowly, as Mach number increases to values greater than about 3 for the flow around spheres in air[1]*. The slow decrease of detachment-distance ratio as the Mach number becomes much greater than 1 may be considered analogous to the well-known case of the friction factor in a pipe becoming less affected by Reynolds number as the Reynolds number becomes significantly greater than that required for transition. Thus, it becomes necessary only to simulate the shock-detachment distance at some arbitrary hypersonic Mach number. If this can be accomplished, then the difference between the detachment-distance ratio at the test condition and that at any other hypersonic Mach number will be small.

One other parameter influences the detachment-distance ratio, and that is the ratio of specific heats. The detachment-distance ratio decreases slowly with a decreasing ratio of specific heats. Therefore, a Mach number less than 3 may be used to obtain a detachment-distance ratio similar to that obtained for air in hypersonic flow if the gas used in the laboratory device has a ratio of specific heats of less than 1.4. A ratio of specific heats of 1.2 to 1.3 may be considered to be representative for the

*Numbers in parentheses refer to references at the end of this report.

products of combustion of a hydrocarbon fuel with H_2O_2. This leads to similarity with hypersonic flow at a Mach number of about 2.5. Analogous reasoning with a reduced ratio of specific heats leads to similarity of velocity and pressure gradients in the shock layer.

At the altitudes being considered, the Reynolds numbers with respect to the nose-cone radius are extremely high, being of the order of 10^7 to 10^8. Simulation does not require these high Reynolds numbers to be duplicated in the laboratory, but simply that the laboratory Reynolds number be sufficiently high that the flow is well into the turbulent regime not far from the stagnation point[2]. This is easily accomplished in many of the test facilities that might be considered. It is to be noted that this type of reasoning generally precludes the possibility of simulating the exact location of transition to turbulent flow.

The air in the shock-layer region in front of a body at hypersonic velocities is extremely hot. At the shock-layer temperatures, the molecular species of which air is composed may be partially dissociated or even ionized. To achieve both chemical and dynamic similarity with this reacting mixture, the gas used in laboratory studies must be air heated to similar temperatures. The properties of the reacting mixture in the shock layer exert a strong influence on the heat transfer to the body, but fortunately they do not strongly influence the kinematics of the flow field. Scala[3] recently reviewed the parameters necessary for simulation of hypersonic flow, and in addition to the Mach number and Reynolds number, listed five dimensionless groups that should be reproduced in the laboratory to achieve chemical similarity with the reacting gas mixture in the shock layer. Although the kinematics of the flow field about the laboratory test specimens is considered to be important to the simulation of particle effects, the chemistry of the shock-layer gas is not considered critical. The effect of thermochemistry on heat transfer probably can be neglected so long as the heat flux to the model is sufficient to produce a reasonable rate of ablation that would be representative of a practical thermal protection material in hypersonic flight.

The nose region of a re-entry vehicle is generally a portion of a sphere, which leads to an axisymmetric flow field. It is a simple matter to use a spherical-nosed test specimen for laboratory simulation of vehicle geometry. The nose radius may be scaled up or down, depending on other similarity considerations or to accommodate the size of the laboratory facility. As the principal region of interest in this program is the general vicinity of the stagnation point, the model need only geometrically simulate that region of the flight vehicle. Thus, a cylindrical specimen with the nose region composed of only a small portion of a sphere is sufficient for simulation of conditions in the vicinity of the stagnation point. Edge effects at the intersection of the sphere and the cylinder are not felt strongly near the stagnation point. This statement is based on the experimental results presented by Boison and Curtiss[4] for the flow field around hemisphere-cylinders of various degrees of bluntness.

In flight, parallel flow exists ahead of the re-entry body, whereas the direction of flow approaching the body in a laboratory device may not be parallel to the center line of the model. This would be the case, for example, for the exhaust gas from most supersonic nozzles that might be employed for model testing. Difficulties may be encountered if the divergence angle of the nozzle is large. The influence of flow divergence on test results is difficult to evaluate; however, it should be considered when various types of test facilities are reviewed.

Flow Field With Respect to Particles

As has been pointed out already, the particles may be deflected, decelerated, and deformed by aerodynamic forces in the shock layer. Deflection and deceleration affect the impaction efficiency, whereas deformation may lead to droplet disintegration. Furthermore, the particles may lose some mass by evaporation as a result of the high temperatures in the shock layer. In order to establish criteria for simulation of a phenomenon, it is necessary first to determine the parameters that enter into the phenomenon and the relative importance of these parameters. If this is not possible, the phenomenon should be reproduced in entirety in the experiment. Simulation of the impaction efficiency, droplet deformation, and droplet evaporation will be discussed separately.

Particle-Impaction Efficiency

Upon entering the shock layer, the particle originally has a high velocity relative to the shock-layer gases. In some cases, the magnitude of this relative velocity is several thousands of feet per second. Because the shock-layer gas is flowing around the re-entry body, there will be a velocity component normal to the direction of particle motion, except along the streamline to the stagnation point, where only deceleration occurs. Simulation of particle paths requires that both the particle accelerations and the shock-layer time scale be modeled in the experiment.

The deceleration requires the initial particle velocity relative to the shock-layer gas to be reproduced and the ratio of aerodynamic forces to particle mass to be simulated. An approximate analysis of particle deflection and deceleration in order to obtain pertinent parameters follows.

The force on the particle is given approximately by

$$F_p = C_D \frac{1}{2} \rho_g V_r^2 A_p \quad . \tag{1}$$

Conservation of momentum for the particle requires the force to be equal to the time rate of change of linear momentum, which is

$$F_p = \frac{d}{dt} (m_p V) , \tag{2}$$

and, since m_p is assumed to be constant for this analysis,

$$F_p = m_p \frac{dV}{dt} \quad . \tag{3}$$

Combining Equations (1) and (3), and noting that

$$m_p = \rho_p \frac{\pi d_p^3}{6} \quad ,$$

leads to

$$C_D \frac{1}{2} \rho_g V_r^2 \frac{\pi d_p^2}{4} = \rho_p \frac{\pi d_p^3}{6} \frac{dV}{dt} \quad .$$

Solving for the acceleration leads to

$$\frac{dV}{dt} = \frac{3}{4} \frac{\rho_g}{\rho_p} \frac{C_D}{d_p} V_r^2 \quad . \tag{4}$$

The displacement of a particle in the x-direction due to acceleration is proportional to the product of acceleration and the square of time for a constant acceleration, or

$$S \propto \frac{1}{2} \left(\frac{3}{4} \frac{\rho_g}{\rho_p} \frac{C_D}{d_p} V_r^2 \right) t^2 \quad ,$$

which becomes

$$S \propto \frac{1}{2} \left(\frac{3}{4} \frac{\rho_g}{\rho_p} \frac{C_D \lambda^2}{d_p} \right) \left(\frac{V_r}{U_\infty} \right)^2 \left(\frac{t}{\bar{t}} \right) \quad ,$$

where

$$\bar{t} = \frac{\lambda}{U_\infty}$$

and is a characteristic time.

For a uniform particle distribution upstream of the shock wave,

$$\eta = (R - S_{tot})^2 / R^2 \quad ,$$

where S_{tot} is the total displacement of the particle that just misses or just hits the body. Expanding the above expression yields

$$\eta = (R^2 - 2S_{tot} R + S_{tot}^2)/R^2 \quad ,$$

but

$$S_{tot}^2 << R^2 \quad ,$$

except for the extreme situation where the impaction efficiency is close to zero.

Therefore,

$$\eta \approx 1 - 2 (S_{tot}/R) ,$$

which leads to η being approximately a function of the instantaneous particle displacement. Therefore,

$$\eta \simeq \eta \left[1 - B\left(\frac{\rho_g}{\rho_p}\frac{\lambda^2}{d_p R} C_D\right)\left(\frac{V_r}{U_\infty}\right)^2 \left(\frac{t}{\bar{t}}\right)^2\right] . \qquad (5)$$

On the basis of Equation (5), the parameters required for simulation of the particle motion in the shock wave might be considered to be

$$\frac{\rho_g \lambda^2 C_D}{\rho_p d_p R}$$

and a dimensionless group including

$$U_\infty .$$

Hence, the impaction efficiency and impact velocity are functions of these parameters, such that an increase in efficiency is associated with a decrease in the parameter

$$\frac{\rho_g \lambda^2 C_D}{\rho_p d_p R}$$

and an increase in U_∞.

It was felt to be interesting to compare these results with the established similarity criteria for particle impaction in subsonic flow. In order to do this, the inverse of the similarity parameter is used. That is, the impaction efficiency is a function of

$$\frac{\rho_p d_p R}{\rho_g \lambda^2 C_D}$$

In subsonic flow, the drag coefficient is generally taken as the value from Stokes drag law:

$$C_D = \frac{24\mu}{d_p V_r \rho_g}$$

Substitution in the similarity parameter and rearrangement yields, after dropping the numerical constant,

$$\frac{\rho_p d_p^2 V_r}{\mu R (\lambda/R)^2} ,$$

which might be compared with the subsonic similarity parameter[5]:

$$\frac{\rho_p d_p^2 V_r}{\mu R} .$$

Comparison of the two parameters shows the difference to be in the term $(\lambda/R)^2$ in the denominator of the supersonic parameter. As the $(\lambda/R)^2$ is less than 1, the value of the impaction parameter for supersonic flow is greater than that for subsonic flow. This is to be expected, because, in subsonic flow, the presence of the body affects the motion of particles at great distances, whereas, in supersonic flow, the presence of the body affects the particle motion only when the particle encounters the shock wave, a distance λ from the body. Particle impaction efficiency would thus appear to lend itself to analytical evaluation.

Particle Deformation

The similarity parameters for liquid-particle deformations in the size range being considered are not well defined, as indicated later in this report. Hence, an experimental apparatus for studying impact effects should accurately reproduce flight phenomena in order to account for particle deformations. At this time, it can be said only that the aerodynamic forces acting on deforming liquid droplets need be scaled with respect to the response of the droplet to these forces.

Particle Evaporation

The temperatures in the shock layer are sufficient to vaporize the water droplets. However, the residence time in the shock layer is usually not sufficient for equilibrium conditions to be obtained; hence, it is expected that droplets impinge on the melt layer as water droplets, although some evaporation does occur. The similarity parameters that should be utilized in devising an experiment will be reviewed briefly.

If the time required to heat the surface of the particle to its boiling point is neglected, then the quantity of material evaporated from the droplet is evidently proportional to the ratio of the energy transferred from the shock-layer gas into the droplet to the energy required for vaporization of the mass lost and for heating that mass to a mean boundary-layer temperature. The boundary layer referred to here is the boundary layer on the droplet. At shock-layer temperatures, the heat-transfer rate is proportional to the enthalpy difference across the boundary layer. Thus, the ratio of the enthalpy difference across the boundary layer to the enthalpy rise of the vaporized water is probably a pertinent parameter.

A second pertinent parameter would be the shock-layer residence time, which might be taken as proportional to the ratio of shock detachment distance to the particle velocity relative to the re-entry body at the free-stream condition. Droplet evaporation is considered later in this report in order to determine the magnitude of the effect.

The Effect of the Particle on the Nose Cone

In considering the effect of the particle on the nose cone, two parameters of interest are particle momentum and particle energy. In addition, it is necessary to consider the melting surface, the relative size of the particle with respect to some dimension in the ablating system, such as the depth of melt, and finally the question of simulation of the over-all ablation rate on the nose cone and the thermodynamic states of the atmospheric moisture-particles.

It is desirable to simulate both particle momentum and particle energy simultaneously in an experimental device. This requires that particles of the same mass as atmospheric-moisture particles be accelerated to velocities comparable to re-entry velocities. If the test facility does not allow particle acceleration to such high velocities, the mass of the particle must be adjusted to simulate either momentum or energy. As it is desirable, for other reasons, to use particles of the same size as those found in flight, it is probably most convenient to use particles of density greater than water for the tests.

The test facility used in the experimental studies must provide a sufficiently high stagnation temperature to produce a melting surface on the nose-cone specimen. As the effects of various material properties are unknown prior to testing, it is desirable to use the same material for test specimens as that used for thermal protection of the actual re-entry vehicle. Thus, if Micarta 259-2 is accepted as the specimen material, stagnation temperatures of the order of 3500 R are required of the test facility in order to produce a melting surface. It is not felt to be necessary, at least at the present, to reproduce the thermal ablation rates encountered in flight. The requirement of a melting surface establishes the general physical environment in which particle impacts occur and is not rigorously a similarity parameter in the same sense as those previously discussed.

The relation between the particle size and a characteristic dimension of the re-entry body should be simulated in the experiment. As the melting of the body is considered to be important to the impact phenomenon, it is reasonable to presume that the ratio of particle size to melt thickness is an important similarity parameter. It is shown later in this report, on the basis of the data analysis, that the ratio of the product of particle density and diameter to the product of average melt thickness and melt density is of primary importance to the phenomenon of small-particle impact. As the importance of this ratio is evident from the analysis of the data produced during this program, detailed discussion of this ratio will be withheld until the analysis of the data is discussed later in this report. The scaling of the particle-size ratio to free-flight conditions will be covered when the application of results to a free-flight vehicle is discussed. As the exact formulation of this parameter was unknown prior to testing, it was decided to attempt simulation of the particle sizes to be encountered in the atmosphere, and also, within the limitations of the facility, simulation of the melting-surface characteristics. Thus, in accord with previously discussed similarity considerations, the test-specimen material should be the same as that used for protection of the re-entry vehicle, and a reasonable or comparable rate of ablation should be maintained during the experiment.

As atmospheric-moisture particles can be either liquid water or ice, both solid- and liquid-particle impacts should be simulated in order to reproduce the effects produced by impacts with atmospheric-moisture particles. This can be done by using two particle materials of different melting points, such that one material is solid and the other is liquid as they impact onto the surface.

Some cooling effect should be expected as a result of the introduction of either liquid water or ice into the ablating system. This cooling effect depends largely on the thermal properties of water and the rate at which the particles interact with the ablating system. As the energy-transfer mechanisms involved in this cooling process are not yet well understood, it would be desirable to reproduce this phenomenon in the test facility. This requires the use of water or some other low-boiling-point liquid as a particle material. The difficulty here is that a practical test facility should allow the completion of a large number of tests at reasonable cost. A facility so refined that it reproduces the thermodynamic state of the atmospheric-moisture particles at every point in the ablating system was not a practical facility for this program. This is discussed in the next section of this report.

TEST FACILITIES FOR STUDYING PARTICLE IMPACTS ON A MELTING AERODYNAMIC BODY

Various test facilities that might be used for simulation of the impact of atmospheric-moisture particles on the melting surface of a re-entry vehicle are discussed in this section. The similarity parameters relating test to flight conditions that were presented in the preceding section are referred to in connection with each of the facilities discussed. As the conditions for similarity between test and flight are stringent, it is not expected that any one ground facility can provide complete similarity. The most important parameters to be simulated are those that (1) are considered to be critical to the impact phenomena itself, and (2) are not well understood on the basis of previous impact studies. The major types of test facilities are reviewed, and then the ABMA 3.5 AHT facility used in this program is discussed.

General Review of Test Facilities

The suitability of various test facilities to a study of high-speed particle impacts on melting bodies is discussed in this section. In particular, the types of facilities reviewed are (1) rocket engines, (2) plasma jets, (3) shock tubes, (4) hydrogen gas acceleration, and (5) small projectile accelerators. In addition, flight testing in connection with particle-impact studies is reviewed briefly.

Rocket-Engine Facilities

Rocket engines provide a stream of high-velocity, high-temperature gas into which particles may be introduced. High stagnation temperatures, of the order from 3000 R to 6000 R, are easily obtained through the release of chemical energy within the combustion chamber. Although these temperatures are less, in some cases, than those at the re-entry condition being simulated, they are sufficient to melt most materials. Exhaust Mach numbers between 2 and 4 are obtainable at reasonable chamber pressures for sea-level operation. When compared with the cost of other high-temperature test facilities, the cost of running tests in a rocket-engine facility is low. After the capabilities of rocket engines for simulation of the impaction of atmospheric-moisture particles on the melting surface of a re-entry body are reviewed in general, the use of liquid- and solid-propellant engines is discussed separately.

Similarity Considerations. Agosta[6] has shown theoretically that, in some cases, combustion products can be used to simulate pressure ratio across the shock, the ratio of specific heats, the Mach number, and the Reynolds number in hypersonic flow. Mach numbers up to 12 are possible in such a facility without condensation of the expanded working fluid. Of course, the realization of this simulation requires the construction of a specialized wind tunnel utilizing combustion products as the working fluid. The present discussion emphasizes the use of existing rocket-engine facilities, which can be modified to fit the objectives of a particle-impact study.

Although the Mach number in a rocket-engine exhaust at sea level is generally not so high as those experienced by a missile during re-entry along a ballistic trajectory, it is sufficiently high to produce a flow about a properly located blunt body that is geometrically similar to that obtained in flight. That is, the flow in the stagnation region of a properly shaped test specimen can be characterized by the schematic model shown in Figure 1.

The ratio of specific heats for products of combustion is generally around 1.3. Thus, although the Mach number of the gas is less than that being simulated, the shock-detachment-distance ratio, λ/R, may be close to that obtained at higher re-entry Mach numbers in air. Furthermore, as pointed out in the discussion of similarities, unless detailed information regarding the shock-layer flow is required, it is necessary only that the Mach number be significantly greater than 1 for adequate simulation. The Mach numbers produced by a rocket-engine facility can be considered to be sufficient for adequate simulation of the flow field around blunt bodies when particle-impact phenomena are being studied.

The Reynolds number referred to length measured from the stagnation point for rocket-engine exhaust gases is less in most cases than those expected in re-entry. The effect of a lower Reynolds number on boundary-layer turbulence is somewhat counterbalanced by the high level of free-stream turbulence found in a rocket exhaust. However, the location of the point of transition to turbulent flow in the boundary layer on the test specimen is generally not the same as that in free flight. Although this is an important consideration in heat-transfer studies, its effect on particle impacts is considered to be negligible. The same might be said for the chemical composition of the exhaust gas. Thus, a reasonable approximation to the aerodynamic conditions in flight can be obtained in a rocket facility.

It is generally more difficult to simulate the flow field with respect to the particles in a rocket facility than the flow field with respect to the nose cone. Two primary reasons for this are that the aerodynamic forces on the particles in the shock layer are less in the test facility than in flight and that these forces may act for a shorter period of time. One reason for the forces being less than in flight is that the density of the shock-layer gas in the test facility is considerably less than that obtained in flight for altitudes below 40,000 feet. A second factor is that the initial relative velocity between the particle and the shock-layer gas will usually be less in the rocket-engine facility than in flight, since rocket-engine exhaust velocities are of the order of 7000 feet per second at sea level resulting in even slower particle velocities.

As has been mentioned previously, the shock-detachment-distance ratio, λ/R, can be simulated reasonably in a rocket-engine facility; however, the absolute value of the detachment distance depends on the radius of curvature of the nose of the test specimen. If the ratio of the detachment distance to the free-stream gas velocity is considered as a characteristic time in which aerodynamic forces act on the particle, then the rocket facility supplies considerably less time for these forces to act than is available in free flight. This, of course, assumes that the radius of curvature of the nose of the re-entry vehicle will have to be scaled down in order to allow the placement of aerodynamically shaped specimens into the rocket exhaust. Because of the smaller aerodynamic forces and characteristic time in a rocket facility, the impaction efficiency and the particle impact velocity might be higher than at flight conditions, unless particles of much smaller mass than those encountered in flight are used in the experiments.

Energy and momentum considerations, however, require particles of greater mass than atmospheric particles.

The deformation of liquid particles in a rocket-engine facility will not be the same as the deformation of liquid particles in flight. Hence, in addition to the smaller aerodynamic forces and shorter characteristic times provided by a rocket engine, consideration must be given to droplet deformations in the combustion chamber and exhaust nozzle. Finally, it is not considered to be feasible to use water as a particle material in rocket-engine tests, because the size and shape of the particles that impact on the test specimens after passage through the engine would be unknown. The scaling of particle deformation from one liquid to another is not possible at the present state of the art in the field of droplet breakup. For analogous reasons, particle evaporation in the shock layer is not simulated in a rocket exhaust.

When the effect of the high-velocity particles on a melting body is considered, a rocket-engine facility shows up well. Although impact velocities are not so great as those that might occur in flight, the particle energy or momentum can be simulated by adjusting the particle density. Furthermore, the stagnation temperatures and heat fluxes available in a rocket-engine exhaust jet are sufficient to maintain a reasonable test-specimen thermal-ablation rate. By controlling the size of the particles used in the experiment, it is possible to maintain the relationship between particle size and melt-layer thickness required for simulation. Solid- or liquid-particle impacts might be obtained by varying combustion temperature or particle material. For the same reasons that hamper simulation of droplet deformation and evaporation in the shock layer, the cooling effect of water droplets on an ablating nose cone is not simulated adequately in a rocket-engine test facility.

Liquid-Propellant Rocket-Engine Facilities. One of the advantages of the liquid-propellant engine over the solid-propellant engine is relative ease of control. Within certain limits, chamber temperature, chamber pressure, and composition of exhaust products can be varied. Furthermore, the engine can be turned off at any time by stopping the flow of one or more of the propellants. In some cases, it might be convenient to use one or more gaseous propellants in conjunction with a single liquid propellant.

For the purposes of this study, it is desirable to introduce small particles into the combustion chamber of the engine and allow the exhaust gases to accelerate the particles to high velocities. Particles can be introduced into the combustion chamber by slurrying the particles with one of the liquid propellants. Another means of introducing particles into the combustion chamber might be with a fluid-bed feeder or a vibratory feeder in a pressurized chamber. Either method would allow close control of the particle size and concentration in the exhaust stream.

One disadvantage of the liquid-propellant engine for particle-impact studies is that it is not always possible to obtain a uniform distribution of particles in the exhaust. The degree of uniformity depends on the injector design and the nozzle expansion angle.

A detailed discussion of the liquid-propellant engine facility used in this program is presented later in this report.

Solid-Propellant Rocket-Engine Facilities. The solid-propellant engine offers the advantage that particles can be mixed and cast directly with the propellants. Thus, the distribution of particles in the exhaust should be more uniform than in a liquid-propellant engine, although the nozzle expansion angle will lead to some nonuniformity in the particle distribution, as is the case for the liquid-propellant engine.

It is common practice to operate solid-propellant engines at up to 2000-psi chamber pressure. This is considerably in excess of the chamber pressures generally used in liquid-propellant engines, although high chamber pressures are being used for special applications of liquid-propellant engines. Higher chamber pressures, of course, allow expansion to higher Mach numbers and exhaust velocities than are generally obtained from sea-level operation of liquid-propellant engines.

One important disadvantage of using solid-propellant engines for particle-impact studies is the lack of versatility of these engines. Once the propellant is cast, the combustion characteristics or particle-exposure conditions cannot be altered. In a program of this sort, where it may be desirable to change test conditions after observing the results of a preliminary test, the lack of versatility of the solid-propellant engines on hand can be a major deterrent to the research.

In the preceding discussion, it was assumed that the propellant combination considered is clean burning; that is, the combustion products are all gaseous. This assumption is sometimes questionable, especially for propellant combinations that yield high combustion temperatures, and can lead to uncertainty concerning the nature of the exhaust gas.

Plasma-Jet Facilities

Plasma-jet facilities are similar in many respects to rocket-engine facilities, except that the gas is heated to high temperatures by means of a stabilized electric arc. Thus, electrical energy replaces the chemical energy in a rocket engine. Air may be used as a working fluid in a plasma jet, allowing duplication of the high-temperature properties of air behind the bow shock wave on a re-entry body. Temperatures available in plasma jets are considerably higher than those available from rocket-engine facilities.

The quantity of electric power required to heat air to high temperatures is quite high. This high power requirement, plus the fact that power conversion efficiencies greater than 50 per cent are difficult to attain, usually leads to the use of low-weight flows of air, at relatively low pressures, in a plasma-jet facility. For example, the electrical power required to heat 1 pound per second of air at 20 atmospheres to about 13,000 R (7200 K) is roughly 16,800 kilowatts, assuming an energy conversion efficiency of 50 per cent. This corresponds to a nozzle outlet area of approximately 4 square inches.

The high-temperature air produced by the plasma jet is generally not expanded to Mach numbers as high as those attained in a rocket motor, although it is certainly possible to attain high Mach numbers through the use of high chamber pressures.

It is considered to be feasible to introduce particles into a plasma jet. This technique is now being used in the formation of coatings using a plasma jet. However, a development program is needed to determine the effect of the particle injection on the plasma-jet operation. One problem that will be encountered is that any particle material that might be considered could be vaporized at the higher plasma temperatures, and it might prove difficult to determine the amount of particle material lost during passage through the device. Lowering the plasma temperature to minimize particle degradation in effect compromises the advantage of a plasma-jet facility over a rocket-engine facility.

Although the plasma jet can produce heat-transfer rates to test specimens comparable to low-altitude re-entry conditions if a high gas density can be attained, this probably is not of primary importance to the simulation of particle-impact effects. The advantage of a plasma jet over a rocket engine lies in the simulation of the thermodynamic properties of the shock-layer air. However, as was pointed out previously, these are not the most important considerations in the simulation of particle impacts on ablating re-entry bodies

Shock-Tube Facilities

The shock tube, like the plasma jet, is capable of producing high temperatures in air, comparable to those encountered during atmospheric re-entry. The shock tube uses shock-wave phenomena to obtain high temperatures. By combining the shock tube with an expansion nozzle, hypersonic Mach numbers and high stagnation temperatures can be attained in a test section. Nagamatsu, Geiger, and Sheer[7] recently presented a detailed discussion on a device of this type and some of the experimental results obtained with it.

The difficulty in the use of this device is that test times are only of the order of milliseconds, and such short testing times are not considered to be useful in a study of material response to its environment. Thus, even if it were proved possible to introduce particles into the device, the advantages accruing from the use of the device would not be considered worth the efforts involved. It should be noted, however, that this type of device is considered to be extremely useful to studies of the flow around bodies at hypersonic Mach numbers, and the effects produced on a droplet as it passes through a shock wave.

Hydrogen Accelerator

A means of obtaining high-velocity particles in a controllable manner has been suggested recently at Battelle, whereby velocities of from 4000 to 15,000 feet per second can be attained by the expansion of hydrogen. The accelerator would be essentially a blowdown device utilizing the low molecular weight of hydrogen to obtain high gas velocities using reasonable stagnation pressures. Particles would be injected into the high-pressure gas and then be accelerated by the gas to high velocities.

The simplest such device would be a tube with a diverging nozzle attached to its downstream end. Blowdown would be to atmospheric pressure, and gaseous hydrogen would be supplied by a bank of gas cylinders. Particles might be fed into the tube by a fluid-bed feeder or by a vibratory feeder in a pressurized chamber. Stagnation

pressures of around 1500 psi appear to be practical in this device. To improve the performance of the device, the hydrogen could be heated either electrically or by burning a small fraction of the hydrogen with gaseous oxygen. Preliminary calculations based on electric heating to a stagnation temperature of 1500 R show that a velocity of 13,600 feet per second is possible. If the gas is heated to a stagnation temperature of 2000 R, then a velocity of 15,700 feet per second is possible. The electric-power requirements depend on the gas flow contemplated. A 1/2-square-inch throat would allow a 4-square-inch exhaust area, which is more than enough for model tests.

Although high temperatures were not required for the original use contemplated for the hydrogen accelerator, they are required for the present study. By using a low-melting-point model material, a melting surface can be obtained. However, as pointed out in previous sections, it is desirable to study particle impacts on the same material as that being used for thermal protection of re-entry vehicles. Electrically heating the hydrogen to temperatures greater than 2000 R leads to heater and power consumption problems. If the heating were done by combustion, the molecular weight of the combustion products would increase to decrease the exhaust velocity eventually as temperatures greater than 2000 R are obtained. Although a hydrogen accelerator is probably not applicable to the present investigation, it might be worth considering for future studies.

Small Projectile Accelerators

All of the devices considered above have utilized a stationary test specimen and relied on acceleration of the particles to achieve high relative velocities between the particle and the gas. Furthermore, the high stagnation temperatures required for this study are attainable in those devices by raising the energy level of the working gas, using either electrical or chemical energy. The device to be discussed in this section is based on the opposite philosophy, that is, the acceleration of the test specimen to high velocities. High stagnation temperatures are obtained from aerodynamic heating if the specimen velocity is sufficiently high. The philosophy behind this sort of test facility is somewhat similar to that behind actual flight testing. However, the specimen size and the flight range are scaled down considerably.

A facility of this type has been described by McDonough and Hegge[8]. In their facility, small specimens are fired from a gun aimed down a short range, and particles are dropped into the path of the spin-stabilized projectiles by means of a hopper. The projectiles are subsequently recovered for examination. Velocities up to 7000 feet per second can be attained in this facility. However, specimen recovery is a major problem. McDonough[9] has recently shown that high-velocity projectiles can be recovered over a short range by using mild soap flakes to stop the projectile.

The high projectile velocities lead to high temperatures, although they are available only for a short period of time. Thus, specimen melting probably never reaches any reasonable rate during the test. The particle impacts also occur for only a short period of time. Finally, in order to achieve these high velocities, the nose-cone specimens have to be scaled down by large factors.

The use of this type of test facility can be expected to yield interesting qualitative information regarding high-velocity particle impacts on melting bodies. It is not recommended, however, for the quantitative data required in the present program.

Flight Testing

The flight test represents the most sophisticated of all the various types of tests that might be considered. It is only in full-scale flight testing, for example, that perfect similarity can exist between model and prototype. The major problem involved in the extensive use of flight testing is the cost per test.

There are several types of flight tests, however, that are less costly than full-scale missile tests and yet that might yield important information on the effects of atmospheric-moisture particles on an ablating re-entry body. These flight tests depend on the use of smaller, less costly vehicles than ballistic missiles. Both ground-launched and aircraft-launched vehicles could be considered for small-scale flight-test use.

The Jupiter-C and X-17 vehicles have been used successfully in the past for initial flight tests. A still smaller vehicle, such as the six-stage vehicle developed by NASA for Wallops Island firings[10], might be considered for studies of atmospheric-moisture-particle impacts on ablating re-entry bodies. The primary concern in the choice of a test vehicle should be the ability of the vehicle to achieve sufficiently high velocities that ablation occurs. Suitable calculations can be made to scale the results of such tests up to full-scale nose cones. Depending on the versatility of the test vehicle, various re-entry trajectories can be studied under a variety of atmospheric conditions.

Another type of flight-test vehicle that might be considered for studies of particle impacts on melting aerodynamic bodies is a modified small air-to-air missile. It is felt that the required velocities can be achieved with air-to-air vehicles by suitable choice of first-stage and sustainer motors, and also by keeping payload weight to a minimum. Actually, if recovery of the vehicle is planned, the instrumentation required in the model nose cone can be kept to a minimum. If the vehicle can be tracked accurately over a short range, the recovery equipment might also be minimized. As vehicle recovery would represent a major problem to this type of testing, this subject would require close scrutiny if such tests were undertaken. A study of methods of measuring ablation rate during flight and then telemetering these data could also be undertaken. If a method of obtaining this information from telemetered data is developed, then recovery requirements could be eased.

Flight tests were not considered for the present program. However, if the effect of atmospheric-particle impacts on re-entry bodies is considered to be of importance to the design of thermal protection systems, then the eventual use of some type of a flight test will probably be warranted.

The 3.5 AHT Facility

After a survey of possible test facilities, it was concluded that an existing ABMA facility should be utilized for the experimental program. This facility, the 3.5 AHT rocket engine, burns kerosene and hydrogen peroxide, and provides a high-temperature high-velocity stream of gas that can be used to heat aerodynamically shaped test specimens. In addition, particulate matter can be fed into the combustion chamber in the form of a kerosene slurry, resulting in an exhaust stream laden with high-velocity particles of known composition, size, and concentration.

Fused aluminum oxide particles were used in a large number of the tests in the 3.5 AHT exhaust. Since these particles remain solid during passage through the engine, they were used to simulate the impacts of solid ice particles. Particles composed of a low-melting-point glass were used in the remainder of the tests conducted with the 3.5 AHT facility. The glass particles melted in the exhaust jet and thus simulated the impact of liquid droplets.

Specimens are held in the exhaust jet of the 3.5 AHT engine by a remotely controlled, V-shaped model holder. The model holder, which is hydraulically actuated, allows the exposure of two test specimens during each firing of the engine. Steel stingers attached to the specimens are threaded into each of the two arms of the holder. In the neutral model-holder position, the exhaust gases pass between the two arms of the V. Each arm of the V is swung into the gas jet to expose the attached test specimen for the desired time.

The 3.5 AHT engine is fitted with an injector that was designed for the use of three separate propellant components. The particle-kerosene slurry is injected along the axis of the burner through a hole in the center of the injector. Additional clear kerosene is injected radially. This clear kerosene is mixed with decomposed hydrogen peroxide which has been passed through a catalyst bed located upstream of the fuel injector. With operation at 350-psi chamber pressure, the gas stream expands smoothly to the exit of the nozzle, there reaching sea-level pressure with an exhaust Mach number of 2.65. The area of the nozzle exit is 3.48 square inches, and the nozzle has a divergence angle of 15 degrees.

In order to determine the performance of the 3.5 AHT engine with the special injector, it was necessary to operate the engine for several calibration firings. It was hypothesized that the slurried fuel injected into the chamber does not burn, and the fuel injected radially burns with an efficiency of 95 per cent. Combustion temperatures calculated on this basis agree with experimental data obtained during the 3.5 AHT calibration firings. The calibration firings showed that reliable operation at combustion temperatures around 3800 R was practical when small particles were slurried in the fuel on a 1:1 weight basis. This combustion temperature is sufficient to cause ablation of Micarta 259-2. The particles used in the calibration firings constituted a maximum of 5 per cent of the total weight of the exhaust products. A discussion of the analysis and calibration of the 3.5 AHT engine is presented as Appendix A to this report.

In addition to the performance studies discussed in Appendix A, photographs taken during calibration firings were used to determine the shock pattern in the 3.5 AHT exhaust jet. The usual diamond shock pattern found in supersonic free jets results in subsonic regions exterior to the diamonds and supersonic regions interior to the diamonds. It was desired, of course, to locate the test specimens in a reasonably uniform supersonic gas stream in order to simulate the flow field with respect to a free-flight nose cone. It may be recalled from the general discussion of rocket-engine facilities earlier in this report that adequate simulation of the flow field with respect to the nose-cone specimen is achieved in the supersonic rocket-engine exhaust. This uniform supersonic gas stream is most closely approximated at the center of a shock diamond. Thus, after observing the photographs, it was decided to place the test specimens 6 inches downstream of the nozzle exit, which corresponded to the center of the first full shock diamond.

A combustion temperature of 3800 R and a chamber pressure of 350 psi result in an exhaust velocity of about 6700 feet per second. This represents the maximum particle velocity attainable in the exhaust of the 3.5 AHT engine. An analysis of the acceleration of small particles in a rocket exhaust is presented as Appendix B. Numerical results for the 3.5 AHT engine are shown in Appendix B, for particles with a density of 4 g/cc. This density corresponds to aluminum oxide, which, as was previously mentioned, is sufficiently refractory to withstand the 3.5 AHT combustion-chamber temperature. Furthermore, the particle density is sufficiently high to allow reasonable simulation of atmospheric-particle energies relative to a re-entry body even though the particle velocity is less than the velocity of the re-entry body.

Figure 2 shows the calculated particle kinetic energy at the specimen location in the 3.5 AHT engine exhaust as a function of particle size for aluminum oxide. The energies shown on the figure were computed on the basis of the particle velocities obtained in Appendix B. The kinetic energy of water droplets relative to the re-entry body is expected to vary roughly from 10^{-6} to 3×10^{-4} ft-lb. Therefore, it is evident that the particle kinetic energies at the specimen location in the 3.5 AHT engine are of the same order of magnitude as those expected in flight if the particles used in the test are aluminum oxide between 16 and 88 microns in diameter.

Figure 3 shows the calculated particle momentum at the specimen location in the 3.5 AHT exhaust jet. The particle momentums shown in the figure were computed on the basis of the particle velocities obtained in Appendix B. The momentum of atmospheric-moisture particles relative to free-flight missiles ranges roughly from 10^{-9} to 3×10^{-7} lb-sec and are thus of the same order as those obtained by aluminum oxide particles in the 3.5 AHT exhaust.

As has been mentioned earlier in this report, it is not possible to simulate the motion of atmospheric particles in the shock layer, the deformation of droplets in the shock layer, or the evaporation rate of droplets in the shock layer in a rocket-engine facility when the particles used in the tests are denser than atmospheric-moisture particles. However, it is necessary to determine the impaction efficiencies for the particles used in the 3.5 AHT tests. This is done as described in Appendix C to this report. The particle velocities used in Appendix C are those obtained in Appendix B. Because of the use of simplifying assumptions, which all lead to particle deflections greater than actually occur, the impaction efficiencies found in Appendix C are minimum possible values. It is concluded, on the basis of the numerical results presented in Appendix C, that the impaction efficiency for aluminum oxide particles in the 3.5 AHT exhaust will always be close to 100 per cent, and may be taken to be 100 per cent in the analysis of the test results.

The aerodynamic forces acting on the melt layer will be less in the 3.5 AHT tests than in flight at altitudes less than 40,000 feet, where clouds are commonly expected. This is because the stagnation density of the gases in the shock layer in front of the test specimens is approximately 2.3 slugs/cu ft, whereas densities ranging from roughly 5 to 11 slugs/cu ft can be expected along a re-entry trajectory below the 40,000-foot altitude. Similarly, the stagnation pressure behind the bow shock wave in the 3.5 AHT tests is roughly 8 atmospheres, whereas stagnation pressures from 6 to 65 atmospheres can be expected during re-entry at altitudes less than 40,000 feet. Although smaller aerodynamic forces on the specimen surface can lead to relatively thick melt layers in the tests, this is compensated for by a lower thermal ablation rate than is attained in flight. This is discussed in detail later in this report when a melt-thickness

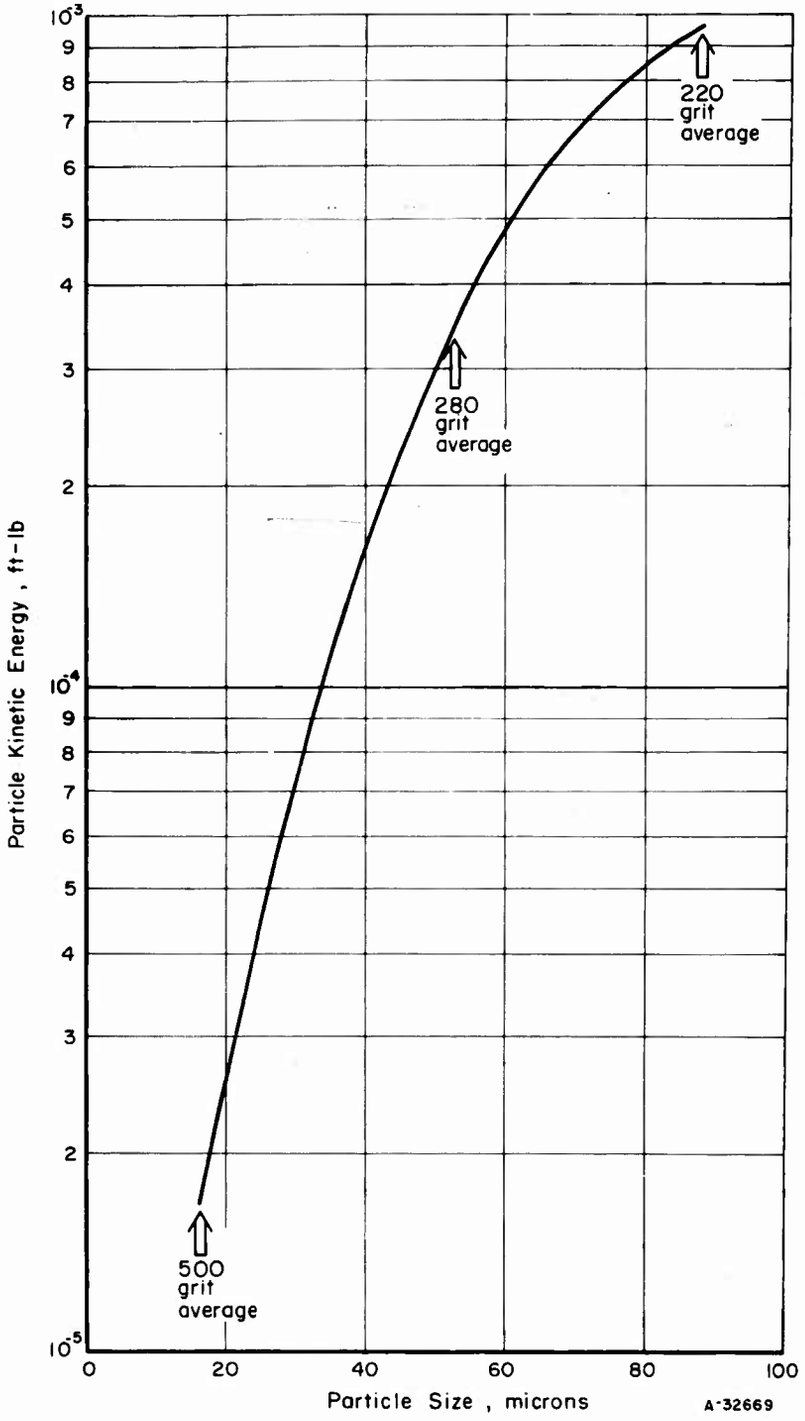

FIGURE 2. PARTICLE ENERGY AS A FUNCTION OF SIZE FOR ALUMINA IN THE 3.5 AHT EXHAUST JET

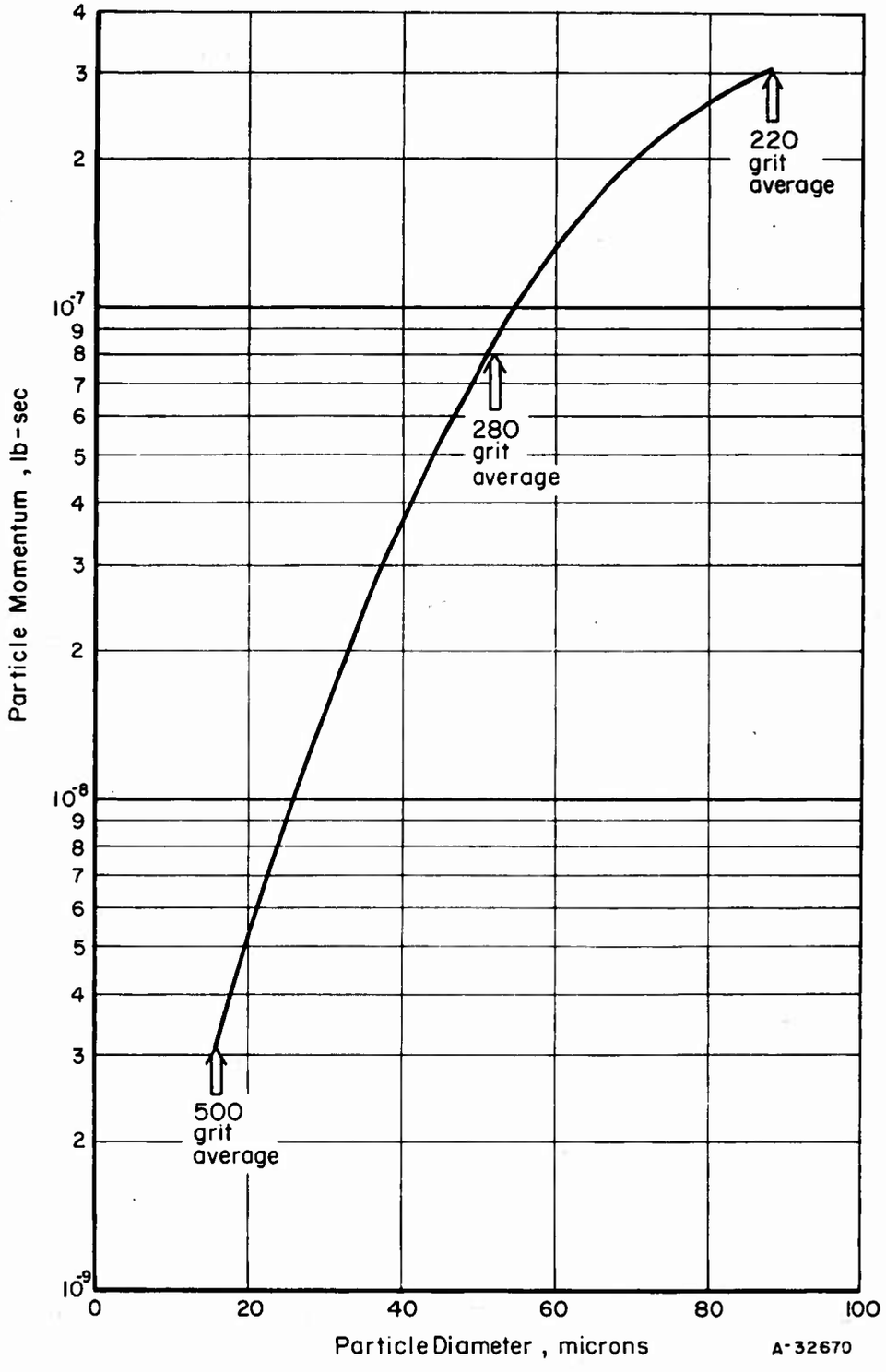

FIGURE 3. PARTICLE MOMENTUM AS A FUNCTION OF SIZE FOR ALUMINA IN THE 3.5 AHT EXHAUST JET

scale factor between test and flight is developed. It turns out that the 3.5 AHT facility adequately simulates the melt thickness on Micarta 259-2 that might be expected in flight.

EXPERIMENTAL PHASE OF RESEARCH

Tests were conducted in the ABMA 3.5 AHT facility in order to determine the effects produced by high-velocity particle impacts on melting aerodynamic bodies. Following these tests, the test specimens and data were analyzed extensively. Although the major emphasis during the program was on Micarta 259-2, other materials were studied in order to obtain qualitative information on the effects of various material properties.

All of the specimens used in the test program had cylindrical bodies with a 2-inch-diameter. The exposed end of the specimen was spherical with a 2.6-inch radius; the other end had a hole to receive the stinger used to attach the specimen to the model holder. This type of specimen presents a reasonably large surface area that can be considered typical of a stagnation region of an actual nose cone. The specimen also permits reasonable simulation of the flow field about the free-flight nose cone.

The exposure conditions used are reviewed, and then the data obtained from the tests are presented. The data presentation is followed by a discussion of the observations made of the test specimens and a quantitative analysis of the test results.

Exposure Conditions

It was shown during the calibration firings that the effect of particles as a heat sink in the 3.5 AHT combustion chamber was negligible in comparison with the effect produced by unburned kerosene. It was decided, therefore, to make all firings with a stoichiometric pilot flame and with a constant quantity of fuel injected in the slurry. That is, the over-all mixture ratio was held constant at approximately 5.5:1, and the flow rate of particles was varied by changing the concentration of oxide in the slurry. This led to the combustion temperature and chamber pressure being approximately constant at 3800 R and 350 psi, respectively, throughout all of the specimen firings. Thus, the heat flux to the specimen was expected to remain approximately constant. This heat flux was computed to be roughly 3 Btu/sec-sq in.

Clear kerosene was used instead of the particle-kerosene slurry for control firings with Micarta 259-2 and the other materials tested. These control firings were used to determine the ablation rates of the specimens and the general response of the material when exposed to the thermal environment produced by the 3.5 AHT engine in the absence of particles.

A particle concentration of 5 per cent by weight of the total flow was the maximum practical commensurate with a high combustion temperature. A particle concentration greater than 5 per cent by weight would have necessitated a slurry thickness greater than 1 pound of particles per pound of fuel. Prior to the calibration runs, it had been found that 1:1 was the maximum slurry concentration that could be used for the largest particles being considered and still allow flow without severe deposition or erosion in the slurry-handling equipment. An increase in the kerosene flow through the central slurry injection hole results in a decrease in the flame temperature. This limitation of the 3.5 AHT facility was established prior to the firings. It is a limitation inherent to any combustion device, although the maximum permissible particle concentration might vary with propellants and injector design.

Two series of tests were conducted under this program using the 3.5 AHT facility. During the first series of tests, only Micarta 259-2 test specimens were used. Particle concentrations of 0.625 per cent and 5 per cent by weight were used. The factor of eight between these two concentrations permitted a determination of whether or not particle concentration produces a linear variation in the ablation rate resulting from particle impact.

The particles used in the first series of tests were fused aluminum oxide in three size groups: 500 grit (16.4-micron diameter average), 280 grit (52.2-micron diameter average), and 220 grit (87.8-micron diameter average). The density of alumina is roughly 4 g/cc, and, as shown in Figure 2, by using this size range, the impact energies obtainable in the 3.5 AHT facility are comparable to those that might be expected in flight. This size range is also comparable to the range of sizes that might be expected for atmospheric-moisture particles.

Figure 4 shows 100X photographs of a sample of each of the three grit sizes used in the first series of tests. The particles are crystalline and roughly approximate spheres. It is considered that these particles adequately simulate the dense type of atmospheric ice particles, as they impact onto a melting body.

As a part of the second series of tests, the range of the experimental data was extended to smaller sized particles. Thus, 1000-grit aluminum oxide particles, which have an average size of 6 microns, were used in the slurry for several of the tests in the second series. As the range of oxide-particle concentration in the gas stream was extremely large in the first series of tests, the second series also included an intermediate concentration of particles, namely, 1-1/2 per cent by weight of the total exhaust stream.

The alumina adequately simulates ice-particle impaction, but the question remained as to whether it also simulates water-droplet impacts. In order to answer this question, a low-melting-point glass powder was used as the particle material during several of the tests in the second series.

The glass, a sodium-potassium-lead glass (light flint glass), had a specific gravity of 3, and was ground to a fine powder. The final product obtained was sorted into two size classifications by water sedimentation techniques. The average particle sizes in these two classifications were 7.6 and 14.1 microns, respectively. Both of these sizes of powdered glass were used in test firings with Micarta specimens and concentrations of 0.625 per cent and 1-1/2 per cent.

It was desirable to determine qualitatively the effects of several properties of the nose-cone material on the particle-impact phenomenon during the second series of tests. As a contrast to the Micarta, it was decided to utilize a homogeneous material that fails in a manner different from the Micarta failure, bearing in mind that the Micarta both forms a liquid melt and discharges gas into the boundary layer. Two ceramic materials were chosen to provide this contrast.

One of these materials is a silica-bonded silica developed by the Georgia Institute of Technology. It was believed that this material would be heated to its plastic point in the 3.5 AHT environment but would not melt. Thus, the particles would impact directly onto a solid surface. A disadvantage of using this material was the unknown response of a deforming surface to impact. A number of specimens made from this

a. 500 grit

b. 280 grit

c. 220 grit

FIGURE 4. 100X PHOTOGRAPHS OF FUSED ALUMINUM OXIDE PARTICLES

material were supplied by the Georgia Institute of Technology. These specimens were exposed to a control condition, 500-grit alumina at 0.625 per cent concentration, and also 280-grit alumina at 0.625 per cent concentration.

The second material that was tested consists of calcium aluminate bonded with calcium aluminate cement. The calcium aluminate aggregate was fired and finely ground, and all moisture was removed. The resulting material, after being ground, was bonded with calcium aluminate cement. Chemically the mixture is 80 per cent alumina, Al_2O_3, and 20 per cent calcia, CaO, whereas physically it consists of 50 per cent free alumina, the remaining alumina having combined chemically with the CaO. The material was made at Battelle specifically for the purpose of this program.

The calcium aluminate mix was intended to melt in the 3.5 AHT exhaust jet without the discharge of any gas into the boundary layer. Although composed of an aggregate and a binder-like concrete, the resultant material is effectively homogeneous, both constituents being the same.

As this material had never been exposed in a rocket-engine exhaust, it was necessary to conduct a preliminary test to determine whether the material actually did melt and also whether the material was desirable for testing from the viewpoints of thermal shock and mechanical properties. This preliminary test was conducted using the 3.5 HT facility at ABMA. This facility is identical to the 3.5 AHT except that the 3.5 HT injector is not equipped for the injection of a particle-laden slurry. The test was conducted at a combustion-chamber pressure of 253 psig, burning 9.86 pounds of peroxide per pound of kerosene. The exposure time was 5 seconds and the weight loss was 8.3 grams. The surface eroded smoothly, but radial cracks did develop along the cylindrical portion of the specimen in the region of the attachment stinger. These cracks did not reach the spherical nose of the specimen. The cracks were not considered to be a detriment to the present work, as they did not lead to material loss. As a result of this preliminary exposure, it was decided to include the material in the second series of tests, where the material was exposed to 0.625 and 5 per cent concentrations of 280- and 500-grit aluminum oxide.

An additional material that was studied in the second series of tests was Battelle Mix 785, which is a ceramic developed under Contract DA-01-021-ORD-4961 for ABMA. Four test specimens were made from this material using the same molds as were used to cast the calcium aluminate specimens. These specimens were fired in two tests, using the condition of no particles in the exhaust and the condition of a 1.5 per cent concentration of the 500-grit aluminum oxide particles.

Observed Erosion Data

Upon completion of the particle-impact tests in the 3.5 AHT facility, the nose-cone specimens were analyzed at the Battelle laboratories. The first step in this analysis was the accurate measurement of material loss, from which ablation rates were calculated. Three different calculations of ablation rates were used for specimens fired in the first series of tests: (1) linear displacement of material or depth of penetration, (2) volume loss of material, and (3) mass loss of material. Only the latter measurement was considered necessary for specimens fired in the second test series.

Figure 5 shows the variation of ablation rate at a radial distance of 0.505 inch from the stagnation point of the Micarta specimens exposed during the first series of tests. Point A corresponds to the top of the specimen, and Point C to the bottom, with respect to the manner in which they were mounted during firing. The similarity of the profiles leads to the observation that the profiles reflect the temperature and particle distribution in the exhaust jet. On the basis of the appearance of specimens fired without particles, it is suspected that the patterns result from the particle distribution. This effect is very striking when the specimens are paired and observed visually.

Figure 6 shows photographs of several typical pairs of Micarta test specimens. Each specimen shown was exposed during the same firing of the 3.5 AHT engine as the other specimen shown with it. There seems to be a particle-size effect in that the specimens fired with the larger particles tended to have craters in the center. That is, the stream of larger particles did not expand to the full width of the gas jet. Thus, the concentration was higher at the center than at the edges of the gas jet. The crater in the specimens fired with a 5 per cent concentration of 220-grit particles was roughly 1-1/4 inches in diameter, which is only slightly larger than the nozzle-throat diameter of 1.064 inches, indicating only slight dispersion of these large particles.

Because of the nonuniformities in ablation presumably resulting from the jet nonuniformities, it appeared that measurements of volume or weight loss would be more indicative of the over-all ablation than linear displacement measurements. The volume- or weight-loss measurements average the ablation and tend to cancel the effects of jet nonuniformities. Because the specimens were almost the diameter of the jet, these measurements probably account for dispersion of the particles satisfactorily.

Table 1 shows the results of the nose-cone-specimen tests conducted under this program. The ablation rates shown in the table are based on weight-loss measurements. One important observation based on Table 1 is that erosion due to particles formed a large part of the material removed, emphasizing the possibility of missile defenses based on the impact of small particles. Erosion rates increased by as much as a factor of 17 in some instances.

As is indicated in Table 1, the thermal ablation rates found in the control firing of Micarta test specimens were 1.5 grams per second in the first series of tests and 1 gram per second in the second series. The reasons for this disparity are not immediately apparent. Propellant flow rates were presumably the same in both series of tests, although the chamber pressure was generally slightly less in the second series of tests than in the first. There were also minor differences in the injector. This disparity in thermal ablation rates may be the result of a decreased chamber temperature and a small difference in the distance between the nozzle exit and the specimen. However, the disparity in ablation rates does not cause any difficulty in the data evaluation because each series of tests is consistent within itself. Furthermore, the decrease in the thermal ablation rate found in the second series of tests affords a fine opportunity to determine the effect of thermal ablation rate on particle erosion.

The results obtained for each of the specimen materials tested is discussed separately from the viewpoint of Table 1 and visual observations of the fired specimens.

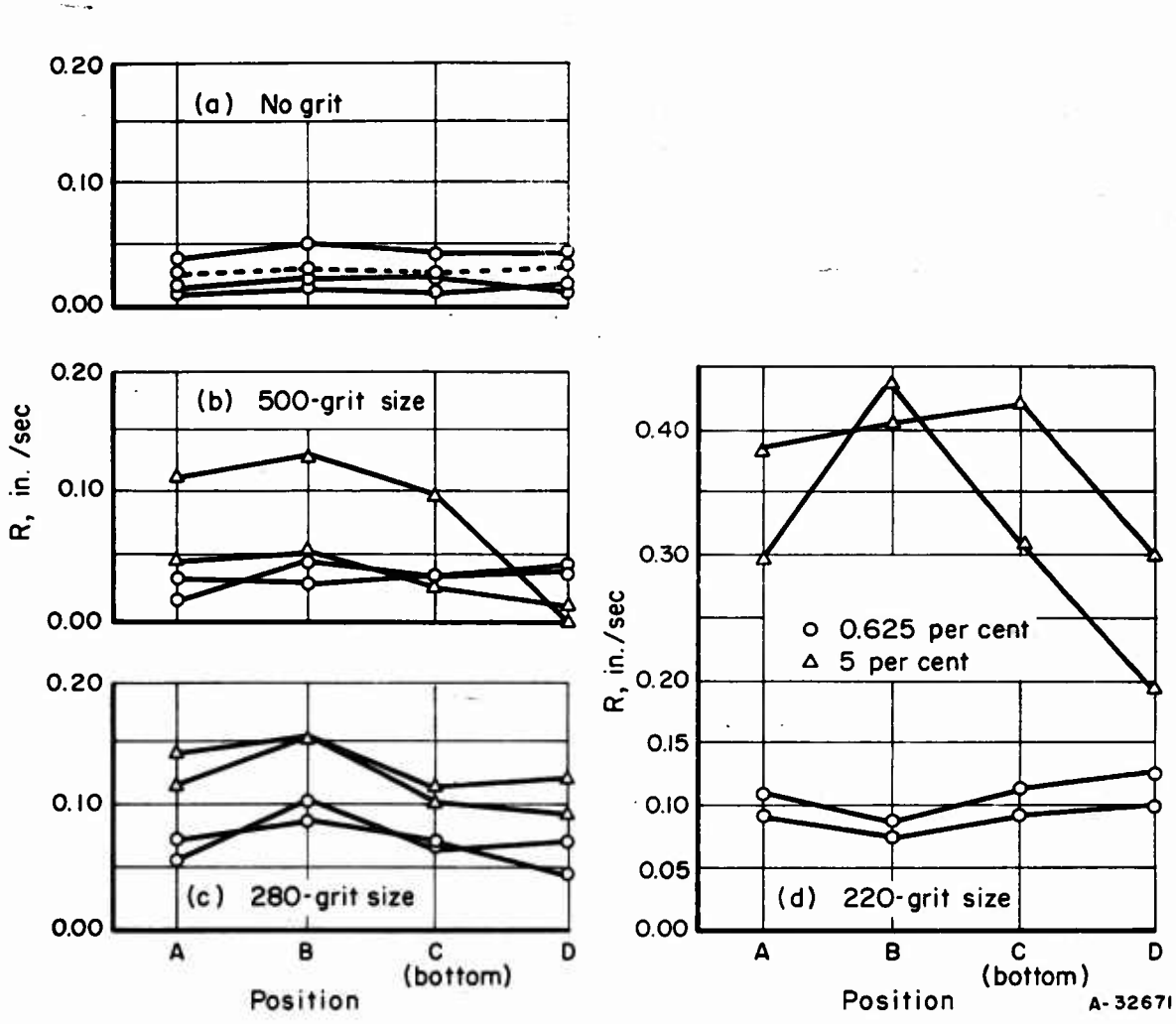

FIGURE 5. ABLATION-RATE PROFILES FOR MICARTA SPECIMENS AT A RADIAL DISTANCE OF 0.5 INCH FROM THE STAGNATION POINT

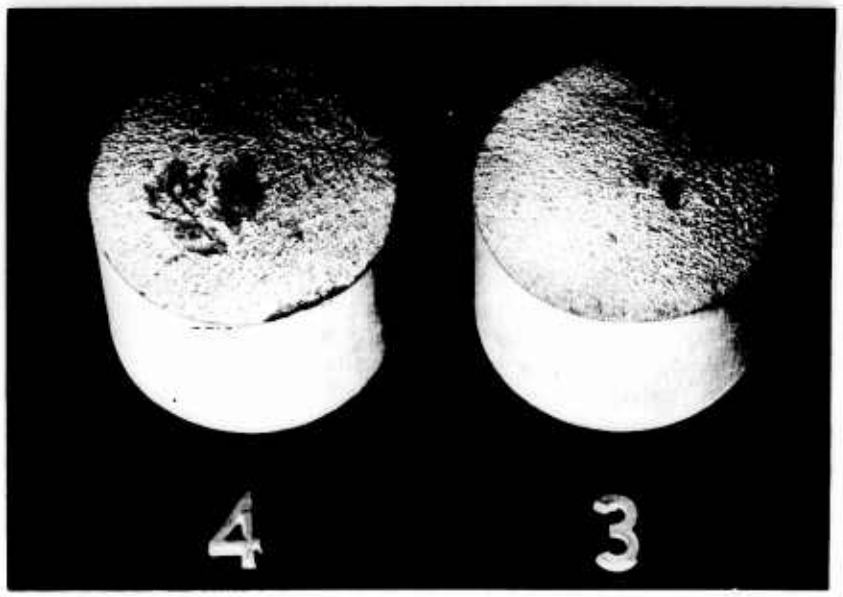

N57355

a. No particles in jet

N57350

b. 5% concentration of 280-grit alumina particles

FIGURE 6. PHOTOGRAPHS OF TYPICAL PAIRS OF TESTED MICARTA SPECIMENS

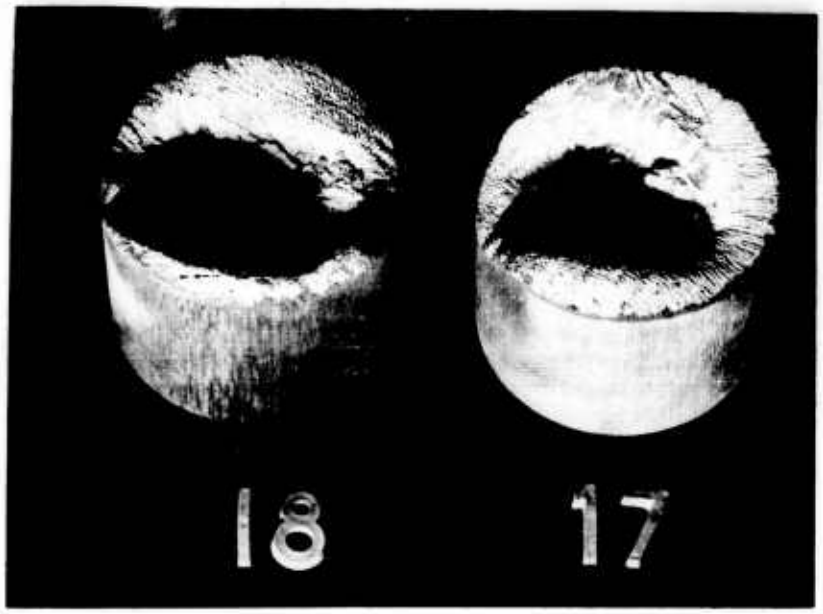

N57354

c. 5% concentration of 220-grit alumina particles

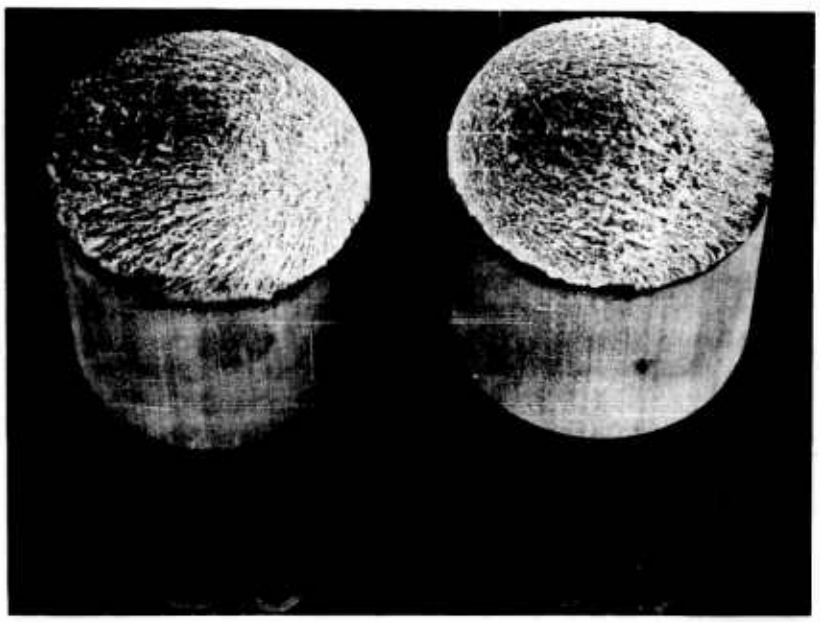

N59649

d. 1.5% concentration of 7.6-micron average size glass particles

FIGURE 6. (CONTINUED)

TABLE 1. RESULTS OF PARTICLE EROSION TESTS IN THE ABMA 3.5 AHT FACILITY

Run[a]	Specimen Material	Particle Material	Particle Concentration (Nominal), per cent	Average Particle Size, microns	Chamber Pressure, psig	Particle Weight Flow, lb/sec	Slurry Fuel Flow, lb/sec	Pilot Fuel Flow, lb/sec	H_2O_2 Flow, lb/sec	Ablation Rate, gr/sec	
										Specimen A	Specimen B
A-41-C[b]	Micarta	–	0	–	371	0	0.121	0.239	1.918	1.52	1.52
A-41-E	Micarta	Al_2O_3	0.625	16.4	374	0.015	0.122	0.238	1.912	3.29	3.60
A-41-F	Micarta	Al_2O_3	5	16.4	368	0.118	0.118	0.239	1.912	7.99	6.29
A-41-H	Micarta	Al_2O_3	0.625	52.2	373	0.015	0.123	0.238	1.914	7.32	6.25
A-41-I	Micarta	Al_2O_3	5	52.2	365	0.126	0.126	0.238	1.912	11.40	11.25
A-41-J	Micarta	Al_2O_3	0.625	87.8	356	0.015	0.122	0.238	1.912	7.72	7.28
A-41-L	Micarta	Al_2O_3	5.0	87.8	361	0.125	0.125	0.239	1.912	21.9	25.9
A-65-D	Micarta	–	0	–	358	0	0.124	0.240	1.92	0.945	1.066
A-64-E	Micarta	Al_2O_3	0.625	6.0	363	0.015	0.122	0.241	1.93	1.32	1.354
A-64-F	Micarta	Al_2O_3	1.5	6.0	362	0.035	0.122	0.238	1.93	1.59	1.773
A-64-G	Micarta	Al_2O_3	1.5	16.4	363	0.035	0.123	0.240	1.92	3.48	4.07
A-65-A	Micarta	Al_2O_3	1.5	52.2	364	0.035	0.123	0.240	1.91	6.32	7.8
A-63-C	Micarta	Glass	0.625	7.6	362	0.016	0.125	0.240	1.93	1.432	1.47
A-63-D	Micarta	Glass	1.5	7.6	363	0.036	0.113	0.242	1.92	1.838	1.49
A-64-C	Micarta	Glass	0.625	17.2	364	0.0149	0.122	0.240	1.93	2.47	2.35
A-64-D	Micarta	Glass	1.5	17.2	367	0.0355	0.123	0.241	1.92	1.53	1.28
A-62-C	Silica	–	0	–	338	0	0.122	0.238	1.93	0	0
A-63-A	Silica	Al_2O_3	0.625	16.4	354	0.0155	0.122	0.237	1.93	6.12	6.1
A-64-B	Silica	Al_2O_3	0.625	52.2	366	0.0141	0.115	0.241	1.92	14.6	16.1
A-63-E	Calcium aluminate	–	0	–	364	0	0.124	0.241	1.92	0.161	0.302
A-63-B	Calcium aluminate	Al_2O_3	0.625	16.4	357	0.0155	0.122	0.238	1.93	−0.056[c]	0[c]
A-63-G	Calcium aluminate	Al_2O_3	5	16.4	370	0.123	0.123	0.241	1.93	−0.486[c]	−0.695[c]
A-64-A	Calcium aluminate	Al_2O_3	0.625	52.2	368	0.014	0.114	0.241	1.92	5.35	3.13
A-65-C[d]	Calcium aluminate	Al_2O_3	0.625	52.2	362	0.0148	0.121	0.243	1.92	7.43	(d)
A-65-B[d]	Calcium aluminate	Al_2O_3	5	52.2	363	0.124	0.124	0.238	1.92	Disintegrated	Disintegrated
A-63-F	Mix 785	–	0	–	367	0	0.125	0.240	1.93	(e)	(e)
A-64-H	Mix 785	Al_2O_3	1.5	16.4	364	0.035	0.114	0.241	1.93	(e)	(e)

(a) Run numbers correspond to those used at ABMA.
(b) The A-41 series of tests are the first series of tests in this program; the other tests were in the second series.
(c) Particles deposited on specimens.
(d) Only one specimen exposed in A-65-C.
(e) These data classified; reported to ABMA under contract DA-01-021-ORD-4961.

BATTELLE MEMORIAL INSTITUTE

Micarta Test Specimens

Micarta 259-2 is the material that was tested most extensively under this program, as it is considered to be typical of the thermal shield materials used on some re-entry vehicles. Hence, the analysis of the test results for Micarta was more extensive than for the ceramic materials. The ceramic materials were qualitatively compared with Micarta to determine the effect of material properties on the response of the specimens to particle impact. The discussion in this section will be concerned with a detailed analysis of the Micarta specimens and data that was carried out during this program.

Thermal ablation of Micarta in the 3.5 AHT exhaust took place as a result of the glass laminates melting and the melamine resin filler decomposing. The melting glass resulted in the generation of a thin layer of flowing molten glass on the surface of the specimen, whereas the thermal decomposition of the plastic filler resulted in the blowing of gaseous decomposition products through this molten glass and into the gaseous boundary layer.

A microscope analysis of the test specimens was carried out. The specimens were first studied under a binocular microscope using powers of magnification from 2 to 150 diameters. Comparisons were made between specimens fired without particles and specimens fired with particles. Particles could not be found in the specimens exposed in the 3.5 AHT facility by this type of examination. The solidified melt was observed to become more dense as the particle exposure becomes more severe. Some unmelted glass fibers could be seen in the melt layer on specimens exposed to particle impact; this was not observed on control specimens.

Samples were scraped from the melted layers of representative specimens and analyzed microscopically. Such examination of samples from the specimens impacted by aluminum oxide particles showed aluminum oxide was present in the melt as discrete particles. The index of refraction of the melt was affected only slightly by the presence of the oxide. In addition, the size of the alumina particles found in the samples was measured, and it was found that the average size of these particles was less than the original size by 35 to 50 per cent. Cracks were also noticed in these alumina particles. The inferences to be drawn from these observations are that (1) the alumina did not melt in the rocket engine and (2) many of the particles fracture on impact. Thus, it is felt that solid-ice particle impacts were adequately simulated by alumina in the 3.5 AHT facility.

Microscope examination of samples taken from the melt layer on Micarta specimens impacted by the low-melting-point glass particles in the 3.5 AHT facility showed that particle melting had occurred prior to impact on the test specimens during the tests. It is to be recalled that liquid-particle impacts were desired, to provide simulation of liquid-water impact. The reason for believing that the glass particles impinged on the test specimens while in the liquid state is that the microscope examination indicated an intimate mixing of the glass from the Micarta and the glass particles. If the particles had struck the surface as a solid, then the last particles to impact as the specimen was removed from the test would be found in discrete particles. The melt layer on the test specimens impacted by glass particles had indices of refraction that were consistently less than either the index of refraction of the glass particles prior to the tests or the index of refraction of the melt on a Micarta test specimen that was not exposed to particle impact. The decreased index of refraction is believed to be the result of some volatilization of the lead and boron constituents of the mixed glasses.

In addition, observations of cross sections of the melt on several Micarta specimens were made. The cross sections were obtained by cutting the specimens with a diamond saw. Melt thicknesses were found to be generally of the order of 70 microns. A charred layer was beneath the melt; its thickness was 3 to 5 times the melt thickness, and generally greater on specimens that were hit with particles. The particles might carry energy more deeply into the body than normal thermal conduction. Microscope examination of samples scraped from the charred layer showed the presence of aluminum oxide particles in the charred layer of those specimens that were impacted on by aluminum oxide particles.

Figure 7 shows 30X photographs of the cross section through two typical test specimens. The melt layer on the specimen exposed to particle impact is considerably more nonuniform than the one on the specimen not exposed to particles. This is believed to have occurred during cooling. The melt is probably relatively uniform in thickness during the test; however, the melt layer on the specimen exposed to particles is probably thicker than on the control specimen during exposure. Several unmelted glass fibers can be seen on the specimen that was exposed to the particle-laden gas stream.

Figure 8 shows the fractional increase in ablation rate due to particle impacts as a function of particle diameter for the Micarta test specimens hit by aluminum oxide particles. The additional erosion resulting from particle impacts is seen to increase in a nonlinear manner with both increasing particle size and increasing particle concentration. Figure B-1 in Appendix B shows that the absolute particle velocity decreases with increasing particle size. Therefore, the total energy and momentum transport for a fixed weight concentration of particles decreases with increasing particle size. Thus, at first glance, an increase in the particle size with a fixed weight concentration of particles would not be expected to cause an increase in ablation rate. Figure 8, however, shows that an increase in ablation rate was obtained with the larger particle sizes. This cannot be explained on the basis of increasing impaction efficiency with increasing particle size, because, as is shown in Appendix C, the impaction efficiency in these tests was close to 100 per cent. Extremely large variations in impaction efficiency would be required to explain the results shown in Figure 8.

The cause of the nonlinear variation of the ablation rate with concentration also was not immediately apparent, as both particle energy and momentum transport vary in a linear manner with particle concentration. These data are discussed further in the next section.

Correlation of Data for Micarta Specimens

A melt-protection mechanism is proposed to explain the results presented in the preceding section for Micarta. In some respects, the proposed protection mechanism is similar to the protection mechanism for thermal ablation. According to the proposed mechanism, an increase in the ablation rate resulting from particle impact results in a thicker melt layer. This thicker melt layer offers resistance to the particle and decelerates it, thus decreasing the impact energy and momentum of the particle as it strikes the solid underlying surface. A correlating equation based on this mechanism has been developed.

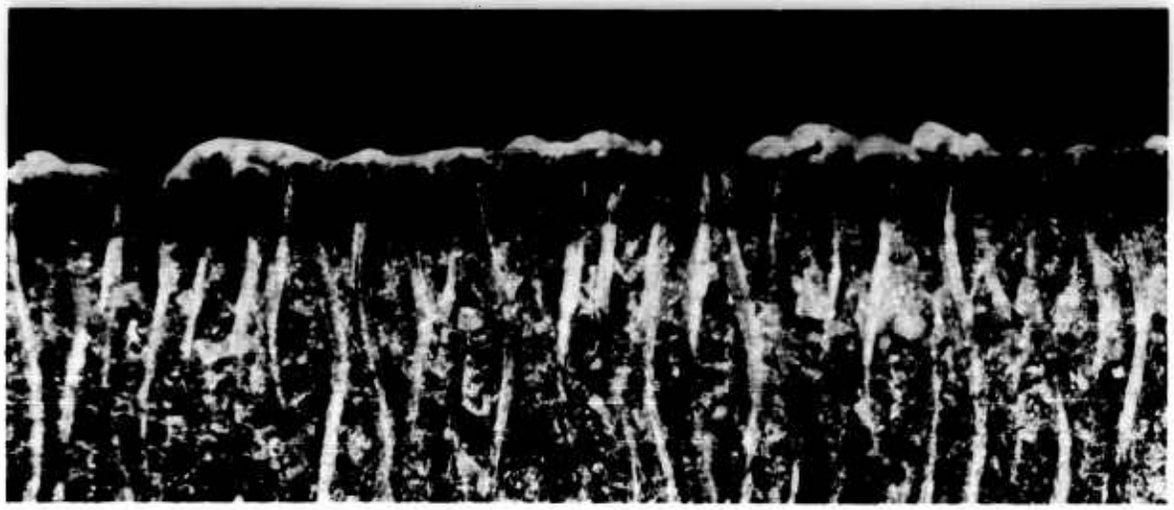

N60099

a. No particles

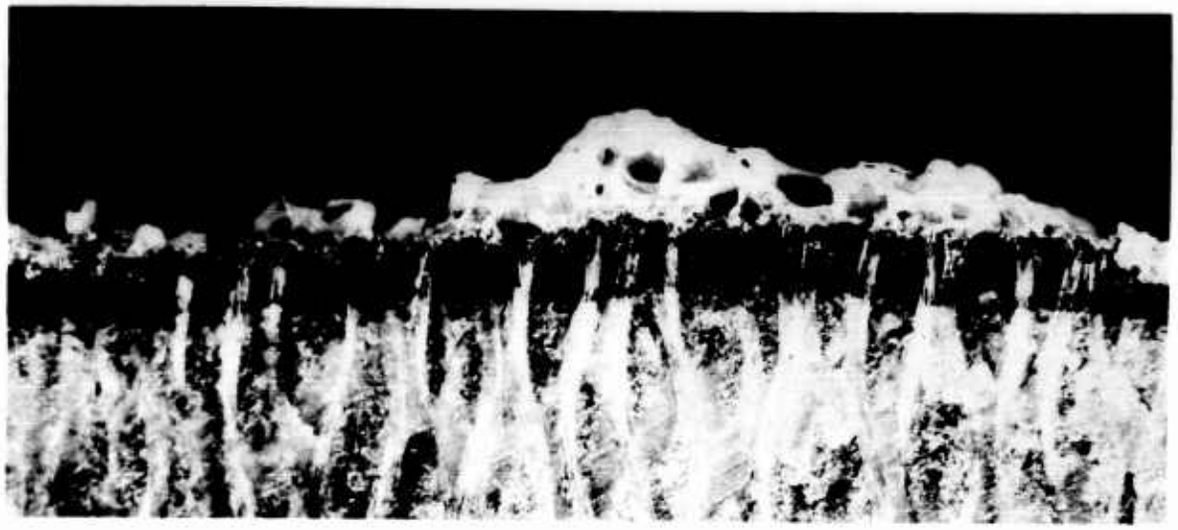

N60101

b. 0.625 per cent concentration of 7.6-micron glass particles

FIGURE 7. 30X PHOTOGRAPHS OF CROSS SECTIONS THROUGH MELT LAYER ON MICARTA SPECIMENS

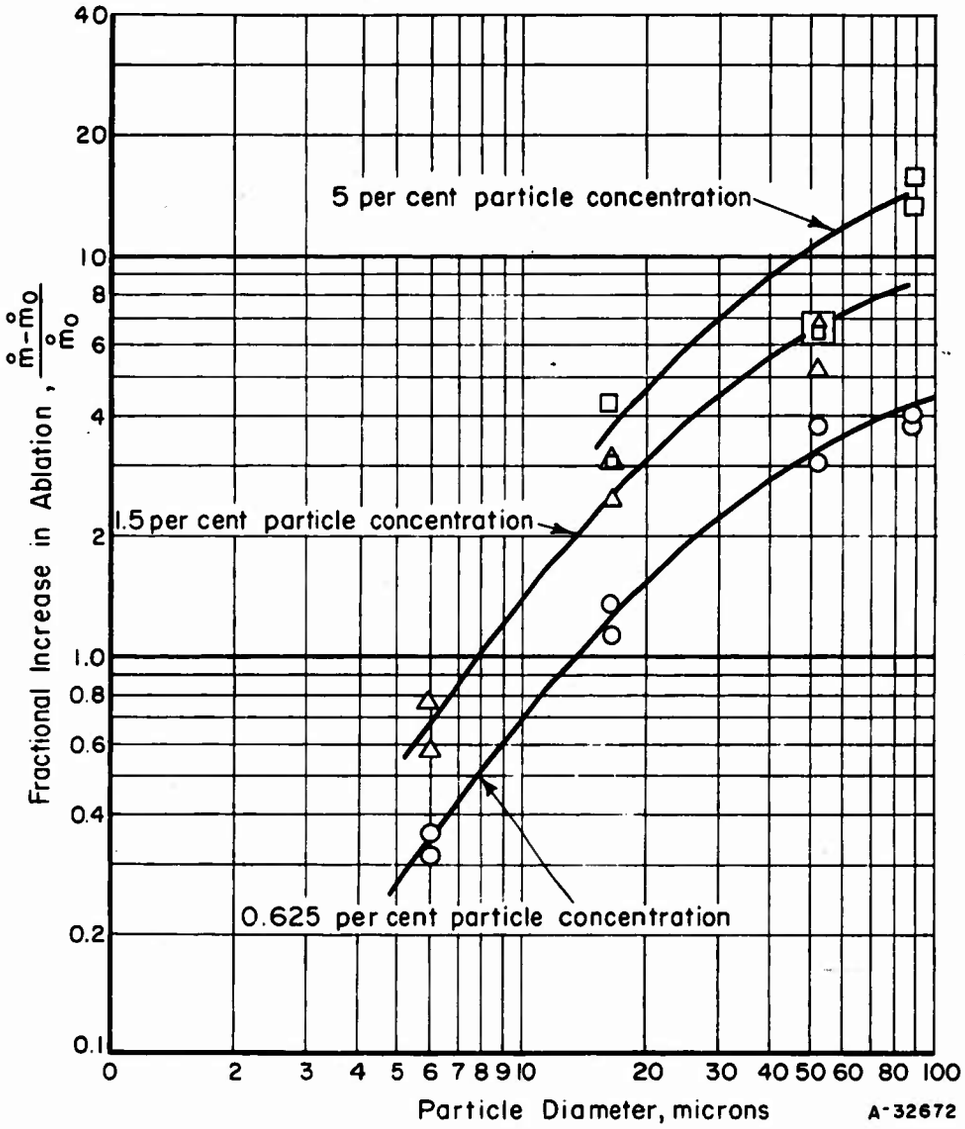

FIGURE 8. FRACTIONAL INCREASE IN ABLATION RATE FOR MICARTA TEST SPECIMENS AND ALUMINUM OXIDE PARTICLES

During the course of analysis based on the melt-protection mechanism, it was found that the particle kinetic energy that is not dissipated in the liquid-melt layer may be accounted for if it is assumed that a fraction of this energy is used to decompose the melamine plastic filler in the Micarta. The decomposition of the plastic results in the evolution of a large quantity of gas; this gas has an effect on the thermal flux into the body. The energy required of the particles is only that necessary to start the melamine decomposition, because the decomposition itself is exothermic. The fraction of the impact energy that is transferred to the melt depends on the probability of a particle striking the melamine plastic filler. This means of accounting for particle energy can be checked, because the energy dissipated in the melt layer can be computed independent of any particular Micarta failure assumption. This check was actually carried out during this program.

After passing through the melt layer, the energy of the particle is not sufficient to melt all of the glass-fiber material that is eroded from the surface of the specimen. The microscope observation disclosed the presence of unmelted glass fibers in the melt. The quantity of unmelted glass found in the melt region generally increased as the severity of particle erosion increased. This observation supports the theory that the particles break down or decompose the melamine. Additional support comes from the observation that the layer of charred plastic on fired test specimens generally was thicker when the specimen was hit by particles. The particles might extend the decomposition of melamine to greater depths than would ordinarily be accounted for by heat transfer.

The system to be analyzed is characterized schematically in Figure 1.

The total ablation rate, $\dot{m}$, is given by

$$\dot{m} = \dot{m}_l - \dot{m}_{stored} \quad . \tag{6}$$

A quasi-static state is assumed; that is, the melt thickness is assumed not to be a function of time. The origin of the coordinate system is assumed to be on the solid surface, and thus recedes with the surface during ablation. For the quasi-static state, the simplification

$$\dot{m}_{stored} = 0$$

may be applied to the ablating system. Therefore, for the quasi-static state:

$$\dot{m} = \dot{m}_l \quad .$$

It is now assumed that $\dot{m}_l$ may be divided into two components, a mass loss due to particle erosion, and a mass loss due to thermal failure of material. Therefore,

$$\dot{m} = \dot{m}_p + \dot{m}_{th} \quad . \tag{7}$$

On the basis of the assumed failure mechanism for the reinforced plastic, the following energy balance may be written

$$Hf\dot{m}_p = F\,(KE)_{impact} \quad ,$$

where F, the fraction of the particle impact kinetic energy transmitted to the plastic filler, may be taken as the volume fraction of plastic material in the composite reinforced plastic. Thus, F essentially is the probability of an impacting particle directly impinging on the plastic, as opposed to the glass filaments.

The energy balance may be rewritten as

$$Hf\dot{m}_p = 1/2\ F\ \frac{w_p}{g_c\ J}\ \eta\ V_f{}^2 \quad .$$

Rearrangement yields

$$\dot{m}_p = \frac{F}{2\ g_c\ Hf}\ \eta\ w_p\ V_f{}^2 \quad . \tag{8}$$

The impact velocity at the solid surface must now be found as a function of the melt-layer thickness, δ, and the initial particle velocity, V_i. It is assumed that the particle passes through the melt layer before the cavity it forms as a wake has time to close. This assumption is consistent with the order of magnitude of the melt thickness observed during the microscope analysis of Micarta test specimens. The particle velocity, V, is assumed to be normal to the surface of the body and not to vary with distance from the stagnation point. Newton's law,

$$F_p = \frac{d}{dt}\ (m_p V) \quad ,$$

becomes, for this case of cavity flow,

$$\left(\frac{\pi d_p{}^2}{4}\right)\left(\rho_L\ \frac{V^2}{2}\right) = \rho_p\ \frac{\pi d_p{}^3}{6}\ \frac{dV}{dt} \quad .$$

Algebraic manipulation yields

$$\frac{dV}{dt} = \frac{3}{4}\ \frac{\rho_L}{\rho_p}\ \frac{V^2}{d_p} \quad . \tag{9}$$

Equation (9) can now be written as

$$V\ \frac{dV}{dy} = \frac{3}{4}\ \frac{\rho_L}{\rho_p}\ \frac{V^2}{d_p} \quad ,$$

or as

$$\frac{dV}{V} = \frac{3}{4}\ \frac{\rho_L}{\rho_p}\ \frac{d_y}{d_p} \quad . \tag{10}$$

Integration of Equation (10) from V_i to V_f and from $y = \delta$ to $y = 0$ yields

$$\frac{V_f}{V_i} = e^{-3\,\rho_L\,\delta/4\,\rho_p\,d_p} \tag{11}$$

The value of V_i will be taken in most cases as the free-stream velocity of the particle relative to the body. The expression for the material loss due to particle impact may now be written as

$$\dot{m}_p = \frac{F}{2 g_c J Hf} \eta w_p V_i^2 e^{-3\rho_L \delta / 2 \rho_p d_p} , \quad (12)$$

and the total ablation rate is

$$\dot{m} = \frac{F}{2 g_c J Hf} \eta w_p V_i^2 e^{-3\rho_L \delta / 2 \rho_p d_p} + \dot{m}_{th} . \quad (13)$$

Expressions relating the melt thickness, δ, and also $\dot{m}_{th}$ to known parameters are still required. The thermal material loss, $\dot{m}_{th}$, will be considered first. Because there is an interaction between the particle impacts and thermal effects, $\dot{m}_{th}$ is not equal to $\dot{m}_o$. It is now assumed that $\dot{m}_{th}$ is equal to the ablation rate obtained when no particles are present in the free stream, $\dot{m}_o$ minus the mass that would have been ablated by the energy used up in heating to the mean boundary-layer temperature the gases resulting from additional decomposition of the plastic. Thus, an interaction between particle and thermal effects is considered. The effect of these additional gases on the boundary-layer thickness is not considered. The interaction may be expressed approximately as

$$\dot{m}_{th} = \dot{m}_o - 0.6 (T_e - T_f) c_{gf} \dot{m}_p / H_e , \quad (14)$$

where the 0.6 factor arises from Prandtl number effects in the boundary layer. Substitution of Equation (12) into Equation (14), algebraic manipulation, and finally substitution into Equation (13) yields

$$\dot{m} - \dot{m}_o = \left[1 - \frac{0.6 (T_e - T_f) fc_g}{H_e} \right] \frac{F}{2 g_c J Hf} \eta w_p V_i^2 e^{-3 \rho_L \delta / 2 \rho_p d_p} . \quad (15)$$

The only term now remaining to be evaluated in Equation (15) is the average liquid-melt thickness, δ. It will be assumed that all of the gas generated during the ablation process leaves the melt by flowing in the y-direction, and all of the liquid and solid in the melt flow in the x-direction. Furthermore, the flow in the melt is assumed to be one-dimensional. The use of a one-dimensional approximation of the continuity equation yields a relation for δ in terms of δ_o that is in agreement with the more exact form of the continuity equation used later in this report for the determination of δ_o at flight conditions; the difference is in a term that brings in angular position. The one-dimensional approximation allows a simple closed-form solution that is useful in the expression for $\dot{m}$. The fact that the one-dimensional equation is used at this point does not affect the final result, because the ratio δ / δ_o is sought. The total ablation rate may be expressed as

$$\dot{m} = \rho_L \bar{u}_L \delta + f \dot{m} ,$$

which, after rearrangement, yields

$$\dot{m} (1 - f) = \rho_L \bar{u}_L \delta , \quad (16)$$

where the barred value represents an average over the thickness of the melt.

The common assumption is now adopted that the shear stress is not a function of the melt thickness and would be the same if the melt were not present. This implies a linear velocity gradient in the y-direction through the melt. Thus,

$$\bar{u}_L = \frac{\bar{u}_{Lo}\,\delta}{\delta_o} \quad . \tag{17}$$

Substitution of Equation (17) into Equation (16) yields

$$\dot{m}\,(1 - f) = \rho_L \frac{\bar{u}_{Lo}}{\delta_o}\,\delta^2 \quad ,$$

and solving for δ yields

$$\delta = \sqrt{\frac{(1 - f)\,\delta_o\,\dot{m}}{\rho_L\,\bar{u}_{Lo}}} \quad . \tag{18}$$

It may be noted that, for the condition of no particles in the free stream,

$$\dot{m}_o = \rho_L\,\bar{u}_{Lo}\,\delta_o + f\,\dot{m}_o \quad ,$$

which may be solved for $\rho_L\,\bar{u}_{Lo}$ to yield

$$\rho_L\,\bar{u}_{Lo} = \frac{\dot{m}_o\,(1 - f)}{\delta_o} \quad .$$

This may now be substituted in Equation (18) to yield

$$\delta = \delta_o \sqrt{\frac{\dot{m}}{\dot{m}_o}} \quad . \tag{19}$$

An expression has now been obtained for the melt-layer thickness that may be substituted into Equation (15) to yield the final result

$$\dot{m} - \dot{m}_o = \left[1 - \frac{0.6\,(T_e - T_f)\,f\,c_g}{H_e}\right] \frac{F}{2\,g_c\,J\,Hf}\,\eta\,w_p\,V_i^2\,e^{-3\,\rho_L\,\delta_o\sqrt{\frac{\dot{m}}{\dot{m}_o}}\Big/2\,\rho_p\,d_p} \quad . \tag{20}$$

This equation may also be expressed in log form as

$$\ln\left\{\frac{2\,g_c\,J\,Hf\,(\dot{m} - \dot{m}_o)}{\left[1 - \frac{0.6\,(T_e - T_f)\,f\,c_g}{H_e}\right] F\,\eta\,w_p\,V_i^2}\right\} = -\,3\,\rho_L\,\delta_o\sqrt{\frac{\dot{m}}{\dot{m}_o}}\Big/2\,\rho_p\,d_p \quad . \tag{21}$$

Equation (21) implies that a semi-log plot of

$$\frac{\left(\frac{\dot{m}}{\dot{m}_o}\right) - 1}{\eta\,w_p\,V_i^2}$$

as a function of

$$\left(\frac{\dot{m}}{\dot{m}_o}\right)^{1/2} \Big/ d_p$$

should correlate the data for Micarta specimens in the 3.5 AHT exhaust jet for one particle density and for one thermal ablation rate, $\dot{m}_o$. The negative of the slope of the resulting straight line should be the factor

$$\frac{2\,\rho_p}{3\,\rho_L\,\delta_o} \quad .$$

Knowing this factor for one particle density and thermal ablation rate should allow the determination of the factor for other conditions by adjustment of ρ_p for other particle materials and δ_o for other thermal ablation rates.

Figure 9 is the semi-log plot just described. All of the data plotted in Figure 9 are for Micarta specimens that were impacted by alumina particles, ρ_p = 4 g/cc, and $\dot{m}_o$ = 1.5 g/sec, which corresponds to the conditions in the first series of tests. The impaction efficiency, η, is taken as unity. The correlation of the data shown in Figure 9 is considered to be good. A slope of -29.1 microns^{-1} is obtained, which yields a value of 77.7 micron-g/cc for the product $\rho_L\,\delta_o$. If ρ_L is taken to be of the order of unity, then δ_o becomes 77.7 microns, which agrees with the order of magnitude of the melt thickness observed on cross sections through Micarta test specimens. As expected, it is less than the 400 microns mentioned by Sutton[11] for Pyrex glass exposed in a rocket exhaust. The value of δ_o for Micarta in the 3.5 AHT should be less than that for Pyrex in some other facility because the 3.5 AHT gives relatively low thermal ablation rates and roughly half of the ablated Micarta enters the melt as a gas, rather than as a liquid.

The equation used for the correlation of all of the Micarta data is obtained from rearrangement of Equation (21):

$$\frac{\rho_L\,\delta_o}{\rho_p\,d_p} = -\ln\left\{\frac{2\,g_c\,J\,Hf\,(\dot{m}-\dot{m}_o)}{\left[1-\frac{0.6\,(T_e-T_f)\,f\,c_g}{H_e}\right]F\,\eta\,w_p\,V_i^2}\right\}^{\frac{2}{3}\left(\frac{\dot{m}}{\dot{m}_o}\right)^{-1/2}} = -\ln E_R \quad . \quad (22)$$

Equation (22) was checked for all of the Micarta specimen tests conducted in the 3.5 AHT facility, including the tests wherein glass particles were used. The density of the glass particles was 3 g/cc, instead of the 4 g/cc for the alumina particles, and the glass particles struck the specimen surface while in the liquid state.

The value of $\rho_L\,\delta_o$ must be corrected to the thermal ablation rate obtained in the second series of tests (see p 30). Assuming that the melt density and shear stress were the same as in the first series, the value of $\rho_L\,\delta_o$ for the second series of tests should be corrected by the square root of the ratio of the new to the old ablation rate, that is, by $\left(\frac{1}{1.5}\right)^{1/2}$, which is 0.816. The value of $\dot{m}_o$ for the second series was taken at the value found from control firings during those tests.

Figure 10 is a plot of the right-hand side of Equation (22) as a function of the inverse of the left-hand side of the equation. The plot is presented on log-log coordinate

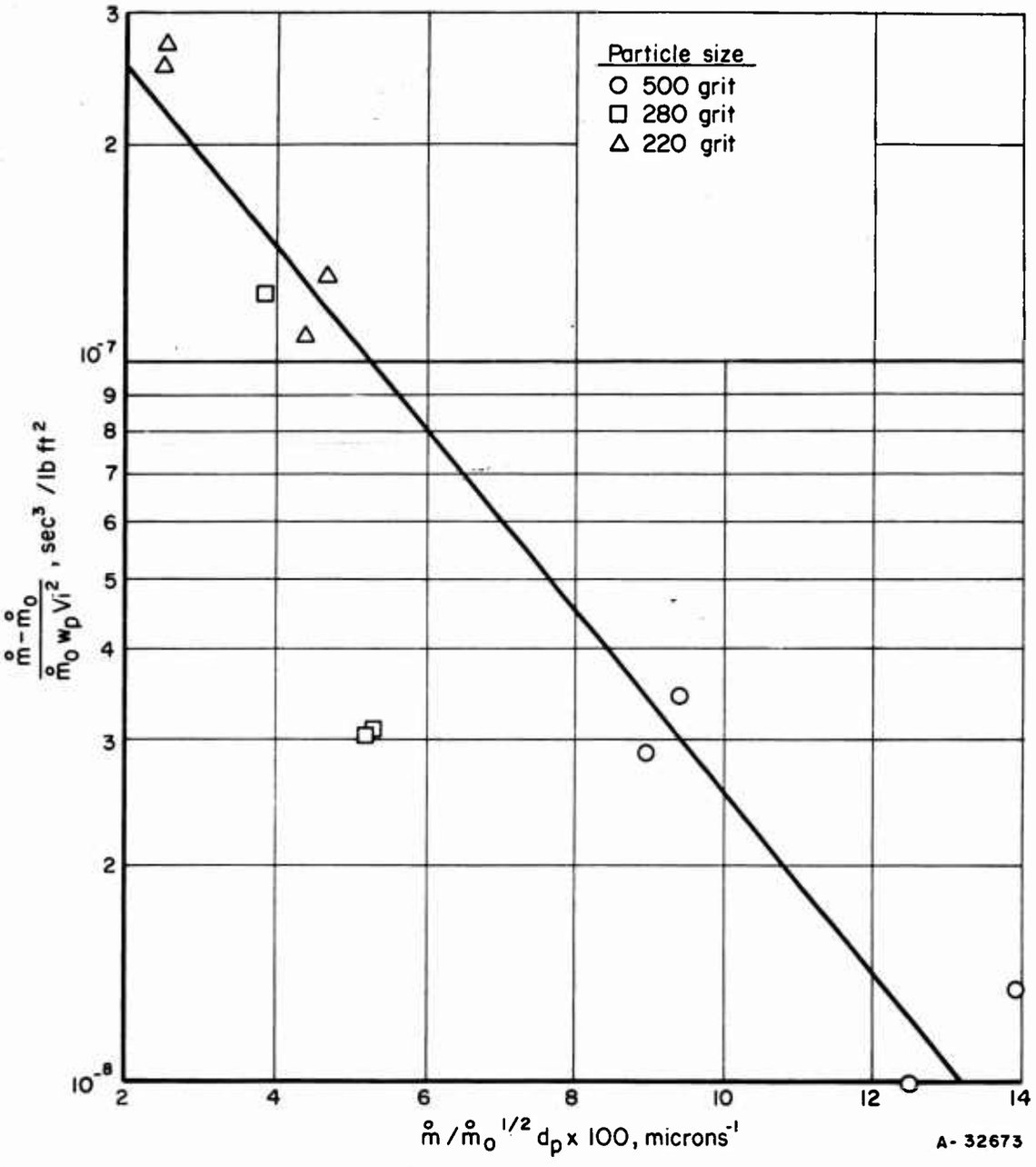

FIGURE 9. CORRELATION OF EROSION DATA FOR MICARTA TEST SPECIMENS IMPACTED BY ALUMINA PARTICLES AT CONCENTRATIONS OF 0.625 AND 5 PER CENT AND WITH AVERAGE SIZES OF 16, 52, AND 88 MICRONS

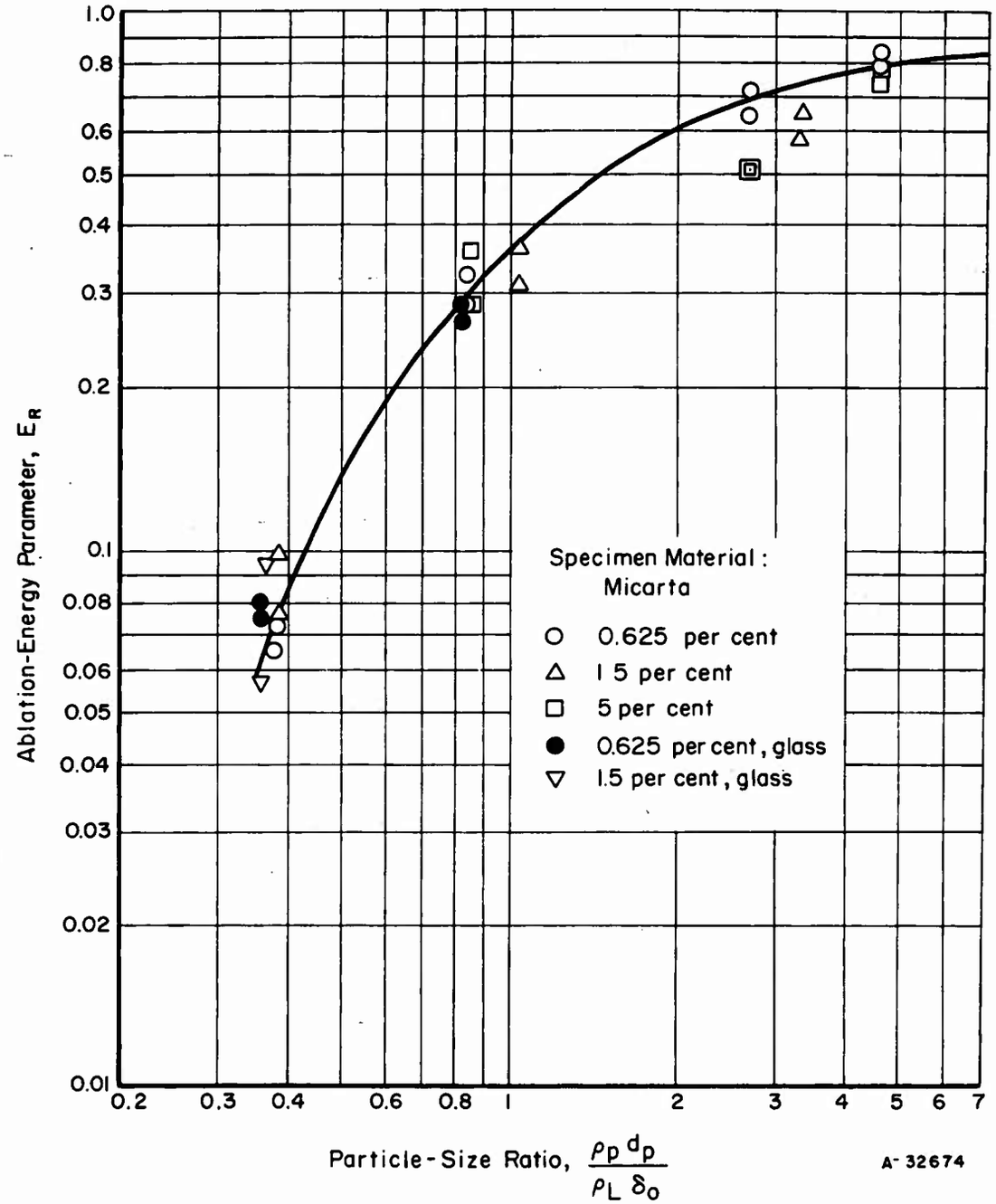

FIGURE 10. ABLATION-ENERGY PARAMETER AS A FUNCTION OF THE PARTICLE-SIZE RATIO

paper because of the range of $\rho_p\, d_p/\rho_L\, \delta_o$ that was tested. Had the left-hand side not been inverted, and had the plot been made on semi-log coordinates, a straight line would have been obtained that would have passed through unity when $\rho_L\, \delta_o/\rho_p\, d_p$ was zero. Instead of this happening, however, the inverse plot of E_R in Figure 22 approaches unity asymptotically as $\rho_p\, d_p/\rho_L\, \delta_o$ becomes very large. The plot implies that, for a fixed impact velocity and flow rate of particles, the ablation rate approaches a constant value as the particle size is increased. This should be expected, because it indicates that the effect of the melt layer on the particle-impact energy becomes very small when the particles get over some certain size. The variable E_R may be interpreted physically as an energy ratio, being roughly the ratio of particle energy utilized in bringing about failure of material to the particle energy immediately outside the melt layer.

All of the data obtained for Micarta test specimens in the 3.5 AHT facility were plotted in Figure 10. The correlation achieved with Equation (22) is considered to be good. The impaction efficiency was taken as 100 per cent, and the value of V_i was taken to be the particle velocity at the specimen location, neglecting deceleration in the shock layer. This is consistent with the results presented in Appendix C.

The results presented in Figure 10 show that the effects of the liquid glass and of the solid alumina particles on Micarta are of the same type. That is, it doesn't appear to make any difference whether the particles are liquid or solid when they impact on melting surfaces with high velocities.

Silica Test Specimens

Three test firings were made using slip-cast silica test specimens fabricated by the Georgia Institute of Technology. The test conditions and the ablation rates obtained with these specimens are listed in Table 1. The specimens fired without particles showed no ablation, only a glazing of the surface. Hairline cracks appeared on the surface of the specimens; the cracks are believed to have formed during cooling.

Figure 11a shows the specimens fired with a 0.625 per cent concentration of the 500-grit alumina particles. They have deep craters that are elliptical and lie in the same relative position on each of two specimens. The specimens are shown in the figure in the same orientation that they had while exposed in the 3.5 AHT exhaust. There is a yellow and gray deposit on the areas of the specimens that do not have craters. These deposits were studied by microscope and are discussed later in this section; however, it might be noted at this point that the deposits were found to consist mostly of aluminum oxide crystals. The deposit on the specimens and the results of tests on the other materials seem to indicate that the particle distribution was not so nonuniform as might be inferred from just studying these specimens. It is possible that the silica is more sensitive to the particle distribution than the Micarta.

Figure 11b shows the silica specimens fired with a 0.625 per cent concentration of 280-grit alumina. These specimens also had craters, but no noticeable deposits. Microscope examinations of the silica test specimens revealed several interesting points. For instance, the yellow deposit was found to be primarily aluminum oxide, and the silica glass in the region studied had been molten during the test. Microscope examination of the gray portion of the deposits similarly showed aluminum oxide and previously molten silica glass, but also showed from 2 to 5 per cent of mullite phase,

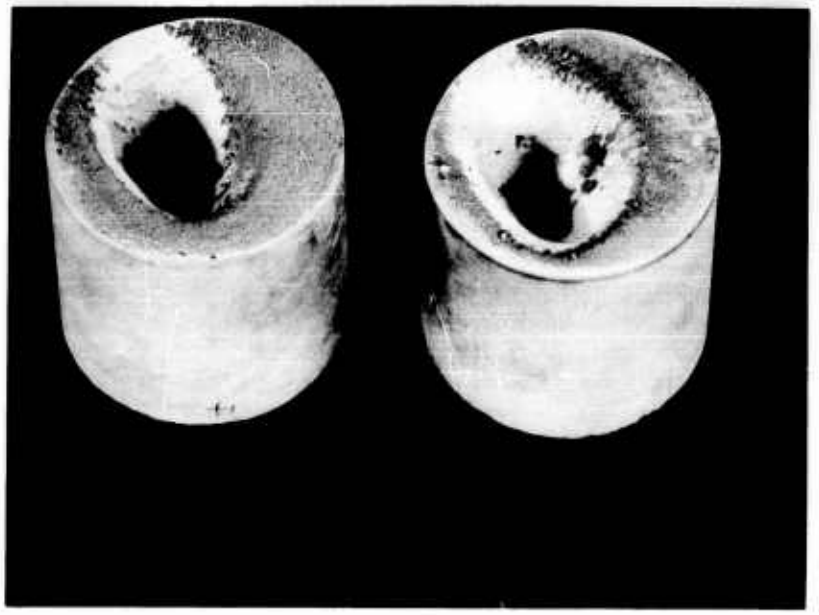

N59643

a. 500-grit, 0.625 per cent concentration

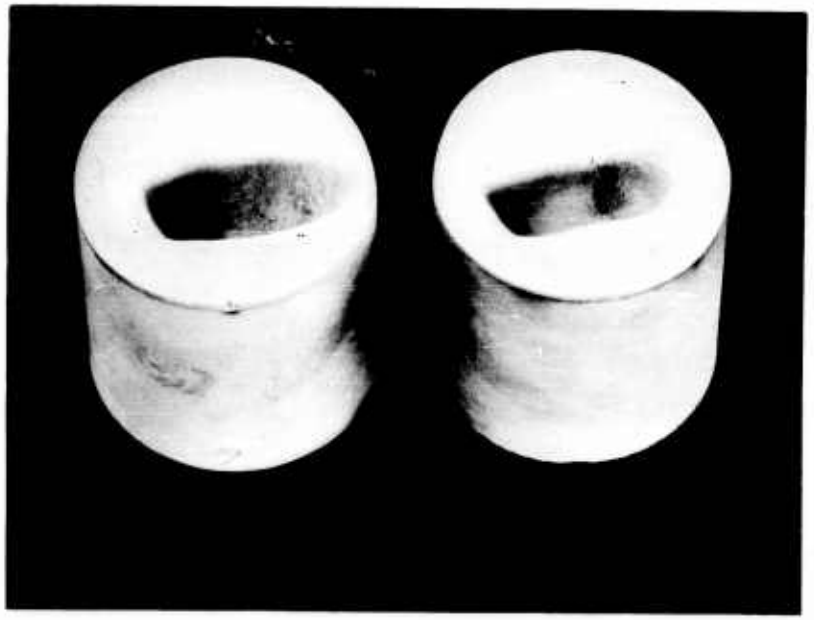

N59652

b. 280-grit, 0.625 per cent concentration

FIGURE 11. SILICA TEST SPECIMENS FOLLOWING EXPOSURE TO ALUMINA-PARTICLE-LADEN 3.5 AHT EXHAUST JET

which is a chemical combination of silica and alumina ($3\ Al_2O_3 \cdot SiO_2$). The low concentration of mullite found on the specimen and the fact that mullite is usually formed during a long-time, high-temperature reaction indicates that chemical attack was not a significant factor in the failure of the specimen material. Molten silica glass found on the test specimen substantiates the explanation of the failure of the test specimens offered below.

It is hypothesized that a thin melt layer was present on the surface of the silica specimens. The glazed surface on the specimens that were exposed only to the thermal environment indicates that either melting or a solid-phase change had occurred during the test. If the glazed surface was not molten, the particle energy may have precipitated melting on the specimens exposed to the particle-laden stream. The presence of the thin melt layer on the specimens exposed to particle impact provided some protection for the surface from the effect of particles. This is the same protection mechanism that is postulated for Micarta test specimens. The quantity of data that are available for the silica specimens is insufficient to allow detailed analysis such as was carried out for the Micarta test-specimen results. However, if the melt-layer protection mechanism is considered to be operative, then the effect of particle size on the erosion rate should be the same as for Micarta. A comparison may be made, therefore, between the Micarta specimens tested with two sizes of alumina particles at a concentration of 0.625 per cent and the silica specimens tested with the same two sizes of alumina particles at the same concentration. The ratio of the average ablation rate for silica specimens with 280-grit particles to that obtained with the 500-grit particles is 2.5, whereas the corresponding ratio for Micarta is 2.8. The effect of particle size on erosion rate depends on several factors, but the values of the ratios compare well to a first-order approximation. The high ablation rates found for silica result from high-energy particles impacting on the solid body beneath a thin melt layer. The absolute value of the ablation rates of the silica specimens were roughly twice that obtained for Micarta at similar firing conditions. This factor of 2 might be decreased at more severe thermal conditions as the silica melt layer becomes thicker.

A larger quantity of melt could be observed in the craters than could be observed elsewhere on the fused silica specimens. The presumably high rate of melting in the craters resulted either from a higher heat flux associated with geometric factors or from additional energy carried to the material by the particles. There is not sufficient evidence to allow correlation of the failure of the silica during particle impact with either particle momentum or with particle energy.

Calcium Aluminate Test Specimens

In all, eight test firings were made using the calcium aluminate as the specimen material. The conditions at which these firings were made and the resulting ablation rates are listed in Table 1. The ablation rates obtained at the "no-particles" control condition were found to be low, being 0.1 to 0.4 gram per second. The weight losses of these specimens appear to be the result of chipping rather than of melting of the material. It should be recalled from a previous section that it was decided to test the calcium aluminate material because it was thought that a melt layer would form but that there would be no gas blowoff into the boundary layer during the test. Micarta, on the other hand, develops a liquid-melt layer and also blows gas into the boundary layer during ablation. The calcium aluminate specimen, however, showed no visual evidence of a liquid-melt layer having formed during the 3.5 AHT tests.

None of the calcium aluminate specimens fired with a slurry containing 500-grit alumina showed any weight loss. A thin yellow deposit was observed on the surface of each of these specimens. Microscopic observations of the deposits showed that they consist of crystalline alumina. There was no chipping on the specimens fired with 500-grit alumina, and the deposit layer on the surface may have protected the specimens from chipping. It should be noted that atmospheric-moisture particles presumably would evaporate before a deposit layer could form, even if the particles were ice.

The calcium aluminate specimens fired with a slurry containing 280-grit alumina had markedly different appearances from the other calcium aluminate specimens. Those specimens fired with a particle concentration of 0.625 per cent exhibited large craters near the surface.

Figure 12 shows two of the specimens fired at this condition. The specimens shown were exposed during a single firing of the 3.5 AHT engine. They are shown oriented in the same manner as they were during exposure. Microscope observations showed the presence of crystalline alumina on the surface of the damaged specimens. Microscope observations also showed that no melting of the calcium aluminate had occurred, even during particle impact.

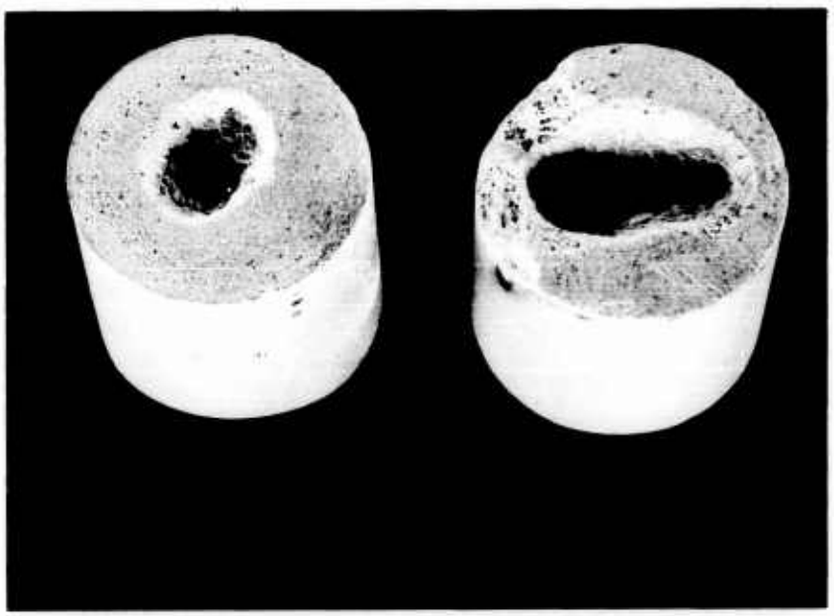

N59639

FIGURE 12. CALCIUM ALUMINATE SPECIMENS FIRED IN THE 3.5 AHT FACILITY WITH A 0.625 PER CENT CONCENTRATION OF 280-GRIT ALUMINA

As indicated in Table 1, high ablation rates of 3.1, 5.4, and 7.4 grams per second were obtained on each of the three specimens fired with a 0.625 per cent concentration of 280-grit alumina particles. The scatter in the ablation rates seems to indicate a lack of reproducibility in the results. As the results for the other materials are reproducible with the 280-grit alumina particles, this lack of reproducibility is considered to be inherent in the calcium aluminate at high rates of failure.

The specimens fired with the 280-grit alumina at a 5 per cent particle concentration disintegrated during the test. Slow-motion movies taken during this test indicated that the specimens first began to erode in a nonuniform manner. It is believed that this nonuniform erosion allowed the exhaust jet to exert a side thrust on the specimens which was sufficient to cause the specimens to fail mechanically in the region of the stinger connection.

The results of the calcium aluminate tests seem to indicate that the 500-grit alumina particles did not have sufficient momentum to cause damage to the surface. On the other hand, the 280-grit particles, being larger, presumably did have sufficient momentum to cause damage. In analyzing these tests, momentum is used as a criterion, rather than energy, which was used in discussing Micarta failure. It is to be recalled that microscopic observations showed that no melting had occurred on the calcium aluminate specimens, even those that were heavily damaged by particles. On a material like calcium aluminate, where the particle impacts cannot precipitate any chemical reactions, the effect of an energy transfer from the particles can cause damage only by inducing melting, which was not observed. Actually, this might be generalized slightly to the statement that impact damage will be associated with particle energy if the ratio of impact energy to the energy necessary to melt the material in the immediate vicinity of the impact is equal to or greater than unity. Conversely, the damage will be associated with momentum if the impact pressure is greater than the maximum stress that the material can withstand in the vicinity of the impact. It is clear that, over a certain particle velocity range, both types of failures are possible. However, when ultra-high-velocity impacts occur, energy effects probably dominate because the they probably take place more rapidly than mechanical damage. Furthermore, as the temperature of the material is raised, the energy increment required to precipitate melting decreases and the energy effects of particle impacts should become more dominant. If melting is already in progress prior to impact, then any increment of particle energy will increase the rate of melting. It is felt that, in the case of the solid calcium aluminate, the damage produced by particle impacts in the 3.5 AHT facility depends on the time rate of change of linear momentum of the particles. Had the calcium aluminate been closer to its melting point, then particle energy might have been the dominant factor in the damage. In contrast to the calcium aluminate, it is interesting to note that the melamine filler in the Micarta material requires only a small amount of energy to cause decomposition.

The total momentum transport to the specimen surface is a first-order function of particle concentration and only a second-order function of particle size. However, the momentum per particle is primarily a function of particle size, as can be seen from Figure 3. It would be expected that, before the total momentum transport can become an important parameter, the individual particle momentum must exceed some limiting value. That value is the momentum required by a single particle to cause damage. Obviously, the 500-grit alumina particles did not have this critical momentum required to cause damage during the test, whereas the 280-grit alumina particles did have the required momentum. It is obvious from the test results that particle concentration, and thus total momentum transport, was an important factor in the 280-grit tests.

Once damage was precipitated by the particles, the severity of the damage, as compared with Micarta, and the strong effect of particle concentration might be explained on the basis that there was no melt layer on the specimen surface to protect it from particle damage. Thus, the importance of the protection offered by the melt layer is accented by the results of the tests wherein 280-grit alumina particles impacted on calcium aluminate specimens.

Mix 785 Test Specimens

The results of the tests with the Mix 785 ceramic specimen material will be covered here only briefly, in a qualitative manner. Mix 785 is a ceramic material developed for ABMA under Contract DA-01-021-ORD-4961. The results of the 3.5 AHT tests for this material have been reported in more detail under that contract.

The test conditions used for this specimen material are listed in Table 1. The thermal ablation rate of the Mix 785 at the "no particles" condition was practically negligible. The introduction of particles caused an increase in the ablation rate. This increased rate was, however, less than that obtained when using Micarta in a purely thermal test at the same operating conditions in the 3.5 AHT exhaust. The aluminum oxide appears to have formed a deposit layer in several places on the specimen noses, while at the same time causing increased erosion at other places.

Projectile-Acceleration Tests

The facility described earlier in this report for the acceleration of small projectiles to high velocities has been used by McDonough and Hegge[8] to study the effect of the impacts of sand particles on high-velocity bullets. In order to extend this work, McDonough, in cooperation with Battelle, studied the impact of Micarta projectiles with 280-grit alumina particles. The projectiles, which had diameters of 0.4 inch and ogival-shaped noses, were accelerated to 5260 ft/sec in these tests[9]. After being accelerated to high velocities, the specimens passed through a mechanically created cloud of alumina particles. The projectiles decelerated rapidly because of atmospheric drag and were recovered after 100 yards of flight while still retaining a velocity of roughly 1500 ft/sec.

A small amount of melting was found to occur at the tip of Micarta specimens. There was some roughening of the specimen nose, presumably due to particle impacts. It is difficult to compare the results of these tests with the other results presented herein because of the short period of time during which aerodynamic heating and particle impacts occurred, of the order of milliseconds, and also because these effects occurred at only a small region of the specimen nose. The over-all material loss was found to be small. The reinforcing fibrous material in the Micarta did begin to melt, but microscope examination showed that no actual melt layer had formed. These tests demonstrate the limitations imposed by the short exposure times inherent in this type of facility. The facility appears, though, to be well suited to the determination of the after-effects of particle impacts, such as surface roughening, on the flow field about the projectiles.

APPLICATION TO FLIGHT VEHICLES

The application of the results presented in this report to the actual condition encountered in flight received some consideration in this program. Special consideration is given to those aspects of atmospheric-moisture-particle impacts that unfortunately could not be closely simulated in the tests conducted with the 3.5 AHT facility. The atmospheric conditions considered herein are presented in Table 2. The clouds listed in Table 2 are considered to be the clouds that are most likely to be encountered during a particular mission. The data listed in the table are based on the results of a survey of available data conducted at Battelle for this program.

The average sizes shown in Table 2 represent mean sizes based on a number count. That is, 50 per cent of the particles will be larger than the mean and 50 per cent smaller. However, the size distribution is expected to be peaked; that is, the mean size represents a favored size and a large number of the particles within a particular cloud will tend to have sizes within a few per cent of the mean. It is justified, therefore, to assume that the mean size is representative of the particular cloud under consideration. Thus, the size range that will be considered in this discussion of particle breakup will be the range of the mean sizes encountered in various common clouds.

Because of the large frontal area and low density of the cloud elements found in the high clouds listed in Table 2, impact with these elements was not considered. It is probably safe to assume that these cloud elements are deflected and evaporated by the shock-layer gases. Thus, particles considered in this discussion are from 8 to 15 microns in diameter. At altitudes greater than 7 kilometers, these moisture particles are probably ice, whereas, between 3 and 7 kilometers, both supercooled water and ice are common. Below 3 kilometers, water droplets predominate for most of the year in temperate zones.

Two re-entry profiles were used for sample calculations. One of these, a 3000-NM trajectory with a ballistic factor of 0.002 cubic meters/kg-sec^2, was chosen for these calculations because the severity of this particular trajectory is indicative of what might be expected for second-generation IRBM re-entry vehicles. The environmental conditions and the thermal ablation rates for Micarta along this trajectory were available from ABMA. A radius of curvature of 1 foot will be assumed for the stagnation-point region of the nose cone.

The second trajectory chosen for sample calculations was a severe 500-NM profile. The environmental conditions and the thermal ablation rates for Micarta along this trajectory were also available from ABMA calculations. A nose radius of curvature of 0.84 inch was used in the calculations for this trajectory.

Several aspects of the particle-impact phenomenon that were not simulated adequately during the experimental phase of this program are discussed in some detail. These aspects are impaction efficiencies, droplet breakup in the shock layer, droplet evaporation in the shock layer, and moisture-particle cooling effects. Analysis of the experimental results showed that the average liquid-melt-layer thickness was an important parameter. A means of obtaining this average melt-layer thickness is described, following the discussions of the aforementioned aspects of the particle-impact phenomena. Finally, the results of sample calculations carried out along the 3000-NM and the 500-NM trajectories are presented.

TABLE 2. DATA FOR FREQUENT CLOUDS

Cloud Type	Base Altitude, km	Thickness, km	Particle Mean, microns	Size Range, microns	Particles/ Cm^3	Water Phase	Cloud-Element Form	Occurrence of Cloud
				High Clouds				
Cirrus and cirrostratus	7-15	1/3	50	10-100	10^2	Ice	Hexagonal prisms, dendritic columns	Common all year
Cirrocumulus	7-15	1/8-1/4	50	10-100	10^2	Ice	Hexagonal prisms or dendritic columns	Infrequent
				Middle Clouds				
Altostratus and altocumulus	Winter, 2-5 Summer, 3-7	3	11	2-30	10^2-10^3	Liquid, ice	Small, compact crystals	Frequent, especially from late fall through spring
				Low Clouds				
Stratus	Near surface to 1	1	13	2-42	10^2-10^3	Liquid	Droplets or flakes	Same as altostratus
Nimbostratus	Surface to 2	1.3-7	13.5	2-42	10^2-10^3	Ice	Compact crystals, snowflakes	Same as stratus
Stratocumulus	1/3-2	1	8	2-42	10^2-10^3	Liquid	Droplets	Very frequent in temperate latitudes
				Vertical Development Clouds				
Cumulus congestus	1/3-2	5	15	3-100	10^2	Liquid	Droplets	Common in tropics and summer

Impaction Efficiency for Atmospheric-Moisture Particles on a Free-Flight Missile

A blunt-nosed re-entry vehicle in flight at supersonic velocities is preceded by a detached bow shock wave. Atmospheric-moisture particles, which might be encountered by the missile, first feel the effect of the vehicle when they are struck by the bow shock. Once the particles pass through the shock wave and enter the shock layer, they are in a predominantly high-velocity, nonuniform flow field. As a result of the shock-layer flow field, forces act on the atmospheric particles that tend to deflect them from the surface of the nose cone. Furthermore, the flow-field forces decelerate the particles with respect to the re-entry vehicle.

In order to facilitate the analysis of this fluid-dynamics system, it is generally convenient to fix the origin of the coordinate system some place on the moving nose cone. The impaction efficiency is defined to be the fraction of the particles within the projected area of the vehicle that impact on the nose cone. If the concentration of particles is assumed to be uniform in space, and if the particles are assumed to be of uniform size, then the impaction efficiency may be considered as a geometric factor. That is, the impaction efficiency may be expressed as the ratio of that portion of the frontal area ahead of the vehicle that contains particles that impact on the vehicle to the entire frontal area. Furthermore, the curve bounding this portion of the projected area is similar to the curve bounding the frontal area, if the flow system is symmetric about the stagnation point. For round nose cones, these curves would be concentric circles. The determination of impaction efficiency thus reduces to the determination of the initial location of the particle that just misses (or hits) the vehicle.

A considerable amount of research has been done on the problem of subsonic impaction of fluid-borne particles on a target in a uniform flow field. This work was reviewed during a recent Battelle program conducted for AEDC[5]. The determination of impaction efficiency is usually started with the momentum equation for the particle. It is assumed that a drag force acts on the particle, given by Stokes' drag law, and thus the drag is proportional to the first power of the particle velocity relative to the fluid. In a subsonic flow field, the disturbance produced by the presence of the target body is felt, theoretically, out to infinity. Thus, the calculation of the path of a particle moving toward the target body is started a large distance ahead of the body. Because the drag force acting on the particle depends on relative velocity, the equations of motion are generally nonlinear. This nonlinearity generally leads to the use of digital or analog computers to obtain numerical results.

The results of subsonic impaction studies show that impaction efficiency varies primarily as a function of the ratio of particle-stopping distance to target radius. This ratio is usually referred to as the impaction parameter and was referred to previously when similarity parameters were discussed. A second parameter, which is the ratio of the square of the particle Reynold's number to the impaction parameter, usually has a second-order influence on the impaction efficiency.

Several important differences exist between the subsonic and supersonic impaction problems. First, as previously pointed out, the particle feels the effect of the vehicle only when it encounters the bow shock. Thus, any calculation of the motion of the particle should be initiated at the shock-wave location. As it is not expected that small particles, such as might be found as cloud elements, will affect the shock-wave

location, the initial point at which to begin calculations is well defined. This is considered to be a simplification to the subsonic case.

It must be borne in mind that the particle velocity just within the shock layer will not be equal to the gas velocity at that point. In fact, under many conditions, the particle is initially supersonic with respect to the gas in the shock layer. A discussion of drag laws for spheres in supersonic flow is presented in Appendix B, as are drag laws for spheres in subsonic flow. The drag force on the particle is expected to vary as some power of the relative velocity; this power can be between the limits of 1 for Stokes' law and 2 for supersonic flow. The influence of the exponent on velocity will vary, in general, as the particle traverses the shock layer.

The flow field in the shock layer differs considerably from that which would be found about a similarly shaped body in subsonic flow. The shock-layer flow field is characterized by steep gradients of the primary flow variables. An appreciable force may act on the particle in addition to the usual drag force as a result of the large pressure gradients in the shock layer. Furthermore, the available mathematical expressions describing the shock-layer flow field are not considered to be so reliable as those available for subsonic velocities of the body. This is especially true at locations removed from the stagnation point. Thus, in an over-all sense, the supersonic impaction problem must be considered to be more complex than the subsonic problem.

In a recent note, Friedlander[12] suggested a means of obtaining the size of the largest particle that will have an impaction efficiency of zero on a sphere traveling at a hypersonic velocity. Friedlander suggests that, if the impaction efficiency is low, then a particle that enters the shock layer along the stagnation stream line will be acted on by a drag force that is given by Stokes' law when the particle is close to the surface of the sphere. Thus, if the particles are slowed down sufficiently for Stokes' law to be valid, Friedlander's analysis can be used. It will be assumed that the Friedlander analysis is valid along the 3000-NM and 500-NM trajectories under consideration.

Using a Stokes' law drag force, Friedlander presents the equations of motion for the particle. The condition for a zero particle velocity at the stagnation point and therefore a value of the impaction efficiency of zero is found from the equations of motion to be

$$K = \frac{U_\infty}{4Rb_1}, \tag{23}$$

where the impaction parameter, K, is the same as that commonly used in subsonic impaction problems. The value of b_1 used by Friedlander is that obtained by Lighthill[13], and is a function of density ratio across the shock wave, shock-wave location, and sphere radius.

The zero-efficiency value of the impaction parameter can be expressed as a function of the density ratio across the shock wave and the ratio of shock-detachment distance to sphere radius. The zero-efficiency value of K may be found, therefore, as a function of density ratio or Mach number along a missile trajectory. For a Stokes' law drag force, K is by definition

$$K = \frac{\rho_p d_p^2 U_\infty}{18\,\mu R}. \tag{24}$$

Therefore, when K is calculated for an efficiency of zero on the basis of density ratio across the shock wave, the defining equation for K can be solved to yield the maximum particle size that produces an impaction efficiency of zero.

This technique was followed in the current program for altitudes below 40,000 feet along the 3000-NM trajectory that was used as a representative example. The particle sizes for a zero impaction efficiency were found to vary between 5.40 and 6.15 microns when the particle specific gravity was taken to be unity.

It is assumed that the impaction efficiency varies rapidly with particle size. This assumption is in agreement with experimental and theoretical results obtained for spheres in subsonic flow[5]. Average particle sizes ranging from 8 to 17 microns are expected to be encountered in common clouds. It is assumed, for calculation purposes, that the impaction efficiency of these cloud elements on the missiles under consideration is 100 per cent and that the particles are decelerated only a negligible amount in the shock layer. That is, the impact velocity is essentially the same as the free-stream velocity.

An alternative approach to the problem of computing impaction efficiencies and impact velocities is to solve simultaneously the exact equation of motion in the shock layer, the equations for the fluid-flow field in the shock layer, and a relation between the drag coefficient and relative velocity. The solution to these equations can be obtained by using either numerical or analog methods. It was expected that reasonably accurate results might be obtained from this computation. However, such an extensive computation program was considered to be beyond the needs of the present program.

In philosophy, this computer approach to the free-flight problem is the same as that discussed in Appendix C to this report, wherein minimum impaction efficiencies were calculated for conditions in the tests conducted in the 3.5 AHT exhaust jet. The minimum efficiencies obtained from that analysis are too low to be useful in computations for the free-flight missile, although they are useful in the analysis of the experimental results.

Droplet Deformation and Breakup in the Shock Layer

Atmospheric-moisture particles that might be encountered by a supersonic blunt re-entry vehicle pass rapidly through the bow shock wave that precedes the vehicle in flight, and enter the shock layer at large velocities relative to the shock-layer gases. These relative velocities are almost as great as the vehicle flight velocity. As a result of these relative velocities, aerodynamic forces act on the droplets that tend to decelerate, deflect, and deform the droplets. The droplet deceleration and deflection were discussed in the preceding section in this report. Droplet deformation is discussed at this time. It must be borne in mind that deformation beyond some limit leads to the breakup of the original droplet into two or more smaller droplets.

The particular physical mechanism that controls the deformation and breakup of droplets depends on the size range of the droplets initially. These droplets are seen from Table 2 to be from 8 to 15 microns in diameter. It is assumed that ice particles retain their original shape during passage through the shock layer. Thus, the discussion is limited to the altitude range where liquid droplets are expected.

The literature on droplet deformation was reviewed in order to determine (1) whether the results of any existing theoretical development could be applied to the present problem, and (2) where there are any experimental data available in the 8- to 15-micron size range. Prior to a discussion of the findings of the literature review, it would be well to describe the type of information required.

First of all, it was desirable to determine the particle size that is stable at the high initial relative velocities encountered in the shock layer. If droplets in the 8- to 15-micron size range were found to be stable at these relative velocities, then no further information would be required. However, if the droplets were found to be unstable, then the time required for the droplets to break up would have to be determined. This is because the shock-layer residence time for the droplet is of the order of from 20 to 40 microseconds, and if breakup does not occur within this time, the droplet will impact on the vehicle while still in one piece.

The breakup of raindrops in the region behind Mach 1.3, 1.5, and 1.7 shock waves was studied experimentally and theoretically by Engel[14,15]. For the large drops considered by Engel, 1.4- and 2.7-mm diameter, it was valid to neglect the vibrations of the droplet because the period of free vibration for these large drops is large compared with the time required for breakup. This is not the case for drops in the size range from 8 to 15 microns, where the period of oscillation is sufficiently short that the oscillations contribute significantly to the droplet deformation. For example, the natural period of oscillation for a 10-micron particle is computed to be 2.9 microseconds. Thus, it should be expected that the actual physical mechanism of breakup for the large drops is different than that for the small drops. Thus, data obtained for large drops should not be extrapolated to the 8- to 15-micron size range.

Before leaving the discussion of the work done by Engel, it is considered worthwhile to mention that Engel determined the time required for raindrops to disintegrate in the shock layer. Although all of the conditions studied by Engel lead to unstable drops, the breakup times were sufficiently long to allow the drops to impact intact on supersonic spheres with diameters of 2 feet or less. The data presented by Engel are for sea-level conditions; extrapolation to altitude or higher Mach numbers may be carried out if the shock-layer density is assumed to be the same as at the condition studied[16]. It might be found that large raindrops would impact intact on a hypersonic vehicle, even though they are unstable at the shock-layer conditions. This situation might also apply to the 8- to 15-micron droplets. That is, even though they are unstable, insufficient time is available for breakup.

Hinze[17] theoretically studied the deformation of liquid drops in the size range where the deformation rate is dependent on the natural period of oscillation for the droplet. The period of oscillation depends on droplet diameter and surface tension. Hinze obtained a solution to the equation of motion and the continuity equation within the droplet for the cases of small and large viscosity. In order to make the equations tenable, Hinze assumed that only small deformations of the droplet take place. It should be noted immediately that the case for the shock layer is probably one of large deformations that occur in a short time. The errors introduced by this assumption will be discussed later in this section. In a following paper[18], Hinze applied his solutions of the flow equations within the droplet to the determination of critical droplet diameters and breakup times. The experimental data used by Hinze for comparison with his results are for drops much larger than 15 microns at velocities much less

than those encountered in re-entry. Calculations based on Hinze's equations show that the droplets being considered here are unstable in the shock layer and the breakup times are of the order of a microsecond, assuming a small viscosity.

At this point, the applicability of the assumptions made by Hinze to the present problem will be questioned. Those assumptions that are questioned are (1) small deformation and (2) viscosity effect on the small-viscosity case. The natural period of oscillation for a liquid drop was found by Rayleigh[19]. The expression derived by Rayleigh is the one used by Hinze and others to determine the natural period of oscillation for liquid drops. However, Rayleigh conducted an experiment where he broke up a 19.7-cubic-centimeter-per-second stream of water with a tuning fork making 128 vibrations per second. The period of vibration for the resulting drops was found from the experiment to be 0.0612 second, whereas the computed value was 0.0494 second. Rayleigh attributed this large discrepancy between the measured and predicted periods of oscillation to excessive amplitude, that is, large departures from the assumption of a small disturbance to the drop. The large deformations to be expected for a particle in the shock layer should yield an even greater discrepancy than that found by Rayleigh. Thus, a period of oscillation much greater than that predicted by Rayleigh's equation, and hence, a breakup time greater than that predicted by Hinze's equation, should be experienced by the droplets in the shock layer.

The effect of viscosity on the breakup time should also be considered. According to the criteria set forth by Hinze for the large- and small-viscosity cases, water droplets should be considered using the approximation of small viscosity. This is consistent with the assumption of small deformations. However, in the shock layer, large rates of deformation are predicted by Hinze's theory. These rates of deformation are sufficiently high that the effect of viscosity on the deformation rate probably should be considered. That is, when high rates of deformation are present, the resistance of the fluid to shear no longer can be considered to be negligible. Carrying this to an extreme leads to the obvious statement that an infinite rate of deformation is impossible because this implies an infinite shear stress within the fluid. Viscosity effects should increase the time required for droplet breakup.

Hanson, Domich, and Adams[20] experimentally studied drop breakup at subsonic and supersonic velocities. The size range covered by their experiments was from 100 to 700 microns for both water and methyl alcohol. Photographs of the droplets showed that the drops initially are flattened in the stagnation region; then the entire drop is flattened and becomes a disk; then a bag forms in the center of the drop; then the bag breaks, leaving a ring, which later breaks up into smaller droplets.

Hanson, Domich, and Adams presented extrapolations of their data down to a particle size of 10 microns. Depending on the means of extrapolation, the critical relative velocity between the particle and the gas is found to be either 800 fps or 1300 fps. The greater of these two velocities is obtained from an extrapolation on log-log paper of the results of Hanson, Domich, and Adams, whereas the lower velocity is based on a constant critical Weber number, as predicted by Hinze. The Weber number is the ratio of fluid impact to surface tension forces. A theoretical analysis by Masugi[21] showed agreement with the variable critical Weber number result. In this analysis, the classic results of Rayleigh[19] were extended to include the influence of the gas forces, and, to some extent, the liquid viscosity.

At altitudes below 3 kilometers, all of the cloud elements that might be encountered are normally in the liquid state. At this altitude, the velocity of the 3000-NM missile that is being used for sample calculations is 5900 fps, which leads to a relative velocity between the particle and the gas of 4810 fps at the location immediately inside the shock wave. The shock-layer residence time for the droplet condition lies between 20 and 40 microseconds.

At this 3-kilometer condition, the maximum relative velocity between the particle and the gas is roughly 3-1/2 times the critical velocity determined from the data of Hanson, Domich, and Adams. However, the expected breakup time is longer than 40 microseconds. This statement is based on observation of the breakup photographs shown in Reference 20. For example, Figure 36 of Reference 20 shows that a methyl alcohol drop suspended in an air stream with a velocity about 2-1/2 times the critical velocity takes roughly 100 microseconds to reach the point where it can be said to act as a multitude of droplets. Observation of water droplets 1500 microseconds after impact further substantiates this assumption on breakup time.

Lane[22] studied the breakup of large drops in air streams with Mach numbers up to 2.1 in a shock tube, and determined the stable size resulting from the atomization of the drops. He could not obtain droplets of dibutyl phthalate smaller than 15 microns in his experiments, although this size was attained at a shock-tube diaphragm bursting pressure as low as 20 atmospheres, whereas he used pressures up to 80 atmospheres, corresponding to the maximum Mach number of 2.1. Lane concluded that the rate of decrease in size is lower than might be expected from a constant critical Weber number analysis when a supersonic air blast is encountered. Water is expected to yield a similar result, possibly with a larger stable size. "Supersonic" refers here to the conditions in Lane's experimental setup, droplet breakup being a function of relative velocity, and not Mach number. Hanson, Domich, and Adams stated as one of their conclusions that the mere passage of a drop through a normal shock will not of itself cause breakup. It is the relative velocity between drop and air on the high-density side of the shock wave that, if sustained long enough, will shatter drops above the critical size.

On the basis of the results presented by Hanson, Domich, and Adams, and those presented by Lane, it is considered reasonable to assume that droplets in the 8- to 15-micron size range will remain intact during passage through the shock layer. That is, even though the phenomena of small-droplet breakup are not very well understood, it is reasonable to assume that, if the droplets are unstable, there is insufficient time available in the shock layer for breakup.

It is assumed that droplet breakup is not an important factor affecting the particle erosion of the nose cone along the 3000-NM and the 500-NM trajectories for which sample calculations are made. The 3-kilometer-altitude condition for the 3000 NM trajectory was used as an example in the preceding discussion. Shock-layer residence times greater than 40 microseconds occur below 3 kilometers; however, the relative velocities between the particles and the gas are less than that at 3 kilometers. Because of its smaller nose radius the shock layer residence times associated with the 500 NM missile should be less than those for the 3000 NM missile.

Droplet Evaporation in the Stagnation Region of the Shock Layer

Atmospheric-moisture particles, which might be encountered by a ballistic reentry body, pass rapidly through the bow shock wave that precedes the vehicle in flight, and then pass through the shock layer while traveling at large velocities relative to the vehicle. Subsequently, the particles will impact on the surface of the vehicle if aerodynamic forces acting on the particle are not sufficiently great to deflect the particle from the surface or to stop the particle relative to the vehicle. It is well known that the temperature of the gas in the shock layer may be extremely high. Thus, it becomes necessary to consider the mass loss of the water droplets due to evaporation during passage through the shock layer in order to determine the actual particle mass that may ultimately impact on the surface of the vehicle.

It is assumed that, prior to encountering the missile, the particles under consideration are in the liquid state, which is a conservative assumption when it is considered that high-altitude particles probably will be ice. "Conservative" implies here that the assumption will lead to an overestimate of the loss of particle mass by evaporation; by overestimating the mass loss, the total mass that reaches the body surface is underestimated. Furthermore, it is assumed that the droplets remain spherical during the initial part of the heating cycle in the shock layer. This assumption is considered to be a reasonable one and was discussed in detail in the preceding section of this report. Thus, the problem may be separated into two parts: (1) the heating of the surface to its boiling point, and (2) the rate of evaporation of the droplet at a constant surface temperature.

First, the time required to heat the surface of the particle to its boiling point must be determined. For small particles, it is considered to be reasonable to neglect convection within the droplet. This allows the use of an available solution to the transient-heat-conduction equation for a solid sphere. Jakob[23] presented a solution that allows for a finite but uniform heat-transfer coefficient at the surface of the sphere. Jakob's solution is for a solid sphere that is suddenly placed in a new thermal environment, which is essentially the same situation as is now being analyzed. Jakob presented a curve that can be used to compute the surface temperature as a function of sphere diameter, thermal diffusivity, heat-transfer coefficient, time, initial temperature, and gas temperature. The only unknown still required for the calculation of surface temperature is the heat-transfer coefficient.

Calculation of the Reynolds number, based on particle diameter, for the gas flowing past the particle immediately after passage through the shock layer shows that the flow is well within the laminar regime. For example, along the 3000-NM trajectory that is one of those used for sample calculations, at an altitude of 7 kilometers, the Reynolds number for the flow about a 15-micron particle is 2180; at an altitude of 3 kilometers, the Reynolds number for the flow about an 8-micron particle is 255. Transition to turbulent flow on a sphere occurs at a Reynolds number around 500,000. The value of the Reynolds number for the particle immediately downstream of the shock wave is the maximum value that can be applied to the particle during passage through the shock layer. Thus, if the heat-transfer coefficient is calculated on the basis of this Reynolds number, it too will be a maximum, yielding a conservative result. The heat-transfer coefficient was computed on the basis of the maximum Reynolds number for the particle in the shock layer.

Values of the heat-transfer coefficient were obtained from the following equation, which was presented by McAdams[24] for spheres in the Reynolds number range from 17 to 70,000:

$$\frac{h' d_p}{kg} = 0.37 (Re_p)^{0.6}. \qquad (25)$$

By using this heat-transfer coefficient in conjunction with the solution to the conduction problem mentioned previously, it is possible to compute the time required to heat the surface of the particle to its boiling point.

It is to be noted that, by using this equation for determination of the heat-transfer coefficient, the effect of recombination of the dissociated gases present in the boundary layer is neglected. Atom recombination would increase the heat-transfer rate to the particle because of its associated energy release. Accounting for atom recombination would represent an improvement to the method described herein. The effect of atom recombination can lead to an increase in the heat-transfer rate by a factor of 2 at the higher flight Mach numbers under consideration. The altitudes at which these high Mach numbers occur are greater than 7 kilometers for the 3000-NM trajectory. Evaporation at altitudes greater than 7 kilometers is not considered in this section. Atom-recombination effects at altitudes less than 7 kilometers are counterbalanced somewhat by choosing a maximum Reynolds number for the calculation of the heat-transfer coefficient. It will be seen later in this discussion that the time required to heat the surface of the particle to its boiling point is usually a small fraction of the residence time for the particle in the shock layer. It will be shown that the mass loss of the particle is controlled by the second phase of the heating cycle, that is, the part of the heating cycle wherein evaporation is occurring. The calculation procedure that is advocated for the second phase of the heating cycle accounts for dissociation and recombination of gas molecules.

Consider that the time required for the surface of the particle to be heated to its boiling point has been computed on the basis of the method described above. It now remains to compute the mass evaporated during the remainder of the particle residence time in the shock layer, that is, the difference between the total residence time in the shock layer and the previously discussed initial heating time. During the remainder of the shock-layer residence time, the surface temperature will remain at the boiling temperature associated with the shock-layer pressure.

As before, internal convection currents in the droplet are neglected. This is reasonable for the small droplet sizes being considered. Thus, the liquid droplet may again be considered to act as a solid body. Water evaporates from the droplet and interacts with the high-temperature air in the boundary layer around the particle. The steam both cools and thickens the boundary layer around the particle. This is analogous to the ablation of a solid sphere that forms a gas when heated by high-temperature shock-layer gases. The analogy is strong enough to allow the utilization of the solution to the problem of determining the ablation rate of a subliming solid sphere in a hypersonic flow field presented by Roberts[25]. This solution, presented graphically by Roberts, is utilized in the computation of the mass loss of the particle while in the shock layer. This solution accounts for real gas effects, such as dissociation and recombination of the gas molecules. It is assumed for these calculations that both the Prandtl and the Schmidt numbers are unity.

It is well to discuss briefly the flow field assumed by Roberts and the actual flow field about the water droplet in the shock layer. First of all, Roberts considered only the laminar-flow region near the stagnation point of a sphere in hypersonic flow. Here, the boundary-layer flow about the particle is always laminar because of the low particle Reynolds numbers. Thus, there is no difficulty, as there might be if one or the other of these two cases were based on a turbulent boundary layer.

It should be mentioned that the Roberts solution does not account for the effect of the wake flow on the rear of the sphere. This is not considered serious, because the heat-transfer coefficient in the wake region behind the particle is probably less than that at the stagnation point. Eckert[26] showed that this is the case for a cylinder with the axis normal to the flow at a Reynolds number of 4000. Thus, the use of a stagnation-point value probably leads to a conservative value for the average rate of evaporation. The stagnation-point value will be assumed to be equal to the average evaporation rate for the calculation now being considered.

An additional point should be mentioned before Roberts' analysis is utilized for computations of droplet evaporation. The heat-transfer rate to the stagnation point of a sphere depends on the square root of a velocity coefficient. This coefficient is the stagnation-point-velocity gradient for potential flow. Although a value based on the pressure distribution in hypersonic flow would be used ordinarily in conjunction with Roberts' analysis, it is considered more reasonable to use a subsonic value for the present calculations because the particle only sees the subsonic flow field in the shock layer. That is:

$$C = \left(\frac{du}{dx}\right)_{x=0}, \tag{26}$$

which is

$$C = \left(\frac{du}{dx}\right)_{x=0} = \frac{3}{2}\,\frac{V_r}{R_p} \tag{27}$$

for a sphere in subsonic flow. As the evaporation phase of the heating cycle occurs after the particle has been in the shock layer for a period of time during which surface heating is occurring, it is reasonable to assume that the droplet has been flattened at the stagnation point by aerodynamic forces and, furthermore, that there has been some reduction in the relative velocity between the particle and the gas. For the purposes of computing reasonable evaporation rates, it is assumed that the radius of curvature of the particle at the stagnation point is reduced from its initial value by a factor of 10, which is consistent with the results in the preceding section. Furthermore, in order to compute the stagnation-point velocity gradient, the relative velocity between the particle and the gas is reduced to 75 per cent of its initial value during evaporation.

When the ablation rate of an aerodynamically heated body is determined from an energy balance, as was done by Roberts, it is presumed that all of the energy that enters the solid body eventually shows up as ablated material. That is, the thermal effect is confined to a thin layer on the surface of the nose cone. This is reasonable in that the ablating materials being considered for use as nose-cone thermal shields are generally poor heat conductors. However, the water droplets being considered herein are good heat conductors. The result is that a portion of the energy transferred to the particle during the evaporation phase of the heating cycle serves only to heat the center of the particle, thus raising its temperature. This energy is carried as sensible

energy of the liquid out of the shock layer and into the liquid-melt layer on the nose-cone surface unless, of course, complete evaporation takes place prior to impact. Thus, from this point of view, the calculated evaporation rates will be conservative.

It is assumed that, at altitudes below 3 kilometers, where the ambient temperature is 483 R, all droplets that might be encountered will be in the liquid state. Between 3 and 7 kilometers, both ice and supercooled water might be encountered, whereas, at altitudes greater than 7 kilometers, only ice particles will be encountered by the missile. The results of evaporation calculations for several conditions along the 3000-NM trajectory used for sample computations will now be discussed.

At the 3-kilometer altitude, stratocumulus and cumulus-congestus types of clouds are considered in the present calculations. The average particle sizes associated with these clouds are 8 and 15 microns, respectively. These particle sizes represent the minimum and maximum sizes considered for 3-kilometer altitudes. The stagnation temperature at the 3-kilometer altitude for the trajectory under consideration was found from the calculation to be 2920 R (1662K), whereas the stagnation pressure was found to be 375 psia. The boiling point of water at a pressure of 375 psia is 898 R.

Initial Reynolds numbers of 255 and 478 were computed for the 8- and 15-micron particles, respectively. By using the curves presented by Jakob and the expression for the heat-transfer coefficient discussed previously, the time required to heat the surface of the droplets to the boiling point was computed. The required times were found to be 3.7 microseconds for the 8-micron droplet and 6.5 microseconds for the 15-micron droplet.

The amount of mass loss due to evaporation for the remainder of the shock-layer residence time remains to be computed. Two assumed shock-layer residence times are used for the calculation at each condition: (1) a time based on the assumption that the particle remains at the free-stream velocity during travel through the shock layer, and (2) a time based on the assumption that the particle velocity varies linearly across the shock layer from a maximum equal to the initial particle velocity relative to the nose cone to a minimum of zero. The actual residence time is probably between these two assumed times. The two residence times for the 3-kilometer altitude were computed to be 20.3 and 40.6 microseconds, respectively. The shock-detachment distance used in the computation was calculated from the results of Li and Geiger[1] for a Mach number of 5.4 and an assumed radius of curvature for the nose cone of 1 foot.

The evaporation rates were computed on the basis of the analysis presented by Roberts[25], with the stagnation-point velocity gradient modified to suit the conditions of the present problem, as was discussed previously. By assuming constant evaporation rates, the mass losses for the 8-micron droplet were found to be 21 and 71 per cent of the initial mass at each of the two assumed residence times; whereas the mass losses for the 15-micron particle were found to be 11 and 26 per cent of the initial mass at each of the two assumed residence times. More accurate knowledge of the residence time for the droplets probably would lead to computed values between those presented herein.

A similar calculation carried out at the 7-kilometer altitude for a supercooled 15-micron droplet yielded a mass loss between 24 and 48 per cent of the initial mass for the two assumed residence times.

When it is considered that the calculation method discussed herein should yield a maximum for the mass evaporated, the results of these sample calculations indicate that evaporation might be neglected in an attempt to evaluate the damage to be expected from cloud-element impacts. The calculated mass loss of the droplets would have been considerably less had ice been considered, rather than liquid water. The probability of encountering ice between 3 and 7 kilometers' altitude is high. Droplet evaporation will be neglected in the calculation used to estimate the effect of droplets on free-flight vehicles.

Moisture-Particle Cooling Effects

When water droplets impact on the vehicle surface, they are vaporized and then heated to some temperature greater than their boiling point. Because water has both a high specific heat and a high latent heat, a relatively large quantity of energy is required to account for the enthalpy increase of the water droplets subsequent to impact. Thus, the water droplets act as a heat sink. This was not the case for either the aluminum oxide or glass particles used in the 3.5 AHT experiments.

It is necessary to determine (1) the quantity of energy absorbed by the water droplets and (2) the means by which the water droplet heat sink influences the ablation rate in free flight. In order to account for the particle thermal effects in the calculations to follow, it becomes necessary to make several assumptions. The basis for the assumptions, especially with regard to the second item, may be open to some question. A more refined attack on this problem is discussed later in this section.

A physical model of the chronology of events leading up to the final state of the water in the gas boundary layer must be assumed. It is assumed that the particles, while moving through the shock layer, are heated to the condition of saturated water by the shock-layer gases. This assumption agrees with the heating cycle assumed in the discussion of droplet evaporation. The particles, as saturated water, then impact on the liquid-melt layer. The particles dissipate a substantial portion of their kinetic energy while passing through the melt layer. The particles then impinge on the solid surface below the liquid-melt layer, thereby dissipating their remaining kinetic energy and damaging previously unaffected plastic. The water droplets then evaporate, and the resulting steam diffuses out of the solid body, through the melt layer, and into the gas boundary layer. It can be assumed that the steam is heated to some mean boundary-layer temperature. Although all of the kinetic energy dissipated by the particles while passing through the melt layer probably does not go directly into particle heating, it may be assumed for the energy balance that it does. That is, the additional thermal energy brought into the melt layer by the particles can be balanced out by assuming that it is transferred back to the particles.

On the basis of the preceding physical model, the particle heat-sink capacity may be considered to be

$$\Delta H_w' = \left[h_{fg} + 0.6\,(h_e - h_g) - \left(\frac{V_i^2}{2g_o J} - \frac{V_f^2}{2g_o J} \right) \right] \eta w_p , \qquad (28)$$

where $0.6\,(h_e - h_g)$ is the approximate enthalpy rise of the steam that is required to bring the vaporized droplet to the mean boundary-layer temperature,

$$\left(\frac{V_i^2}{2g_oJ} - \frac{V_f^2}{2g_oJ}\right)$$

is the kinetic energy dissipated in the melt, η is the impaction efficiency, and w_p is the total weight of water that passes through the shock wave per unit time.

It will be noted that the energy required to heat the droplets to the saturated-water condition is omitted from the present considerations. This energy is negligible as compared with the large quantity of energy available in the shock-layer air. Thus, the effect of this energy transfer to the droplet on the convective heat-transfer rate to the vehicle is negligible. The importance of the energy transfer to the droplet in the shock layer is that it places the droplet at the saturated-liquid state at the time it impacts on the liquid melt.

As was stated previously, the term $0.6\,(h_e - h_g)$ represents the approximate enthalpy rise of the steam that is required to bring the vaporized droplet to the mean boundary-layer temperature. The subscript e refers here to the condition at the outer edge of the boundary layer and the subscript g to the saturated-steam condition. The coefficient 0.6 is based on an assumed Prandtl number of 0.75. At high temperatures and pressures, neglecting dissociation, the specific heat of steam becomes relatively constant; the enthalpy difference therefore differs approximately from a temperature difference by a constant.

The heat-sink capacity of the water, $\Delta H_w'$, has to be related to the ablation rate of the reinforced plastic nose cone along a free-flight trajectory. In order to do this, an effective heat of ablation, H_e, was defined to be the ratio of the heat flux into the boundary layer to the mass ablation rate of the material. By taking the ratio $\Delta H_w'/H_e$, the decrease in the thermal ablation rate due to the particle heat-sink effect may be estimated crudely.

It is acknowledged that the effective heat of ablation is a fictitious quantity, and furthermore that the instantaneous ablation rate depends on the heat-flux history as well as the instantaneous heat flux. The melting-body problem could be resolved for the ablation rate as a function of time using a heat flux suitably modified by the particle heat-sink capacity. This type of analysis may also lead to a decreased melt thickness and, thus, greater particle damage than is indicated by a heat-of-ablation method. However, this approach is beyond the scope of the present program. Instead, the effective heat of ablation was used to determine the effect of the particle heat sink. The effective heat of ablation was obtained from average heat fluxes and ablation rates over various regions of the trajectory being studied.

The equation describing the effect of particles on a melting body derived previously will now be modified to account for heat-sink effects. The material loss due to thermal effects is

$$\dot{m}_{th} = \dot{m}_o - \frac{0.6\, c_{gf}(T_e - T_w)}{H_e}\,\dot{m}_p - \frac{\Delta H_w'}{H_e}, \qquad (29)$$

which is the same as Equation (14), except for the last term, which represents the cooling effect of the particles.

The expression for $\dot{m}_{th}$ may be expanded on the basis of Equations (13) and (28). The result is

$$\dot{m}_{th} = \dot{m}_o - \frac{0.6\, c_g f\,(T_e - T_w)}{H_e} \frac{F}{2g_o JHf} \eta w_p V_i^2 e^{-3\rho_L \delta / 2\rho_p d_p}$$

$$- \left[h_{fg} + 0.6(h_e - h_g) - \frac{V_i^2}{2g_o J} \left(1 - e^{-3\rho_L \delta / 2\rho_p d_p} \right) \right] \frac{\eta w_p}{H_e} . \qquad (30)$$

Rearrangement yields

$$\dot{m}_{th} = \dot{m}_o - \left[\frac{0.6\, c_g F\,(T_e - T_w)}{H} \right] \frac{\eta w_p V_i^2}{2g_o JH_e} e^{-3\rho_L \delta / 2\rho_p d_p} - \Delta H_w / H_e , \qquad (31)$$

where

$$\Delta H_w = \left[h_{fg} + 0.6(h_e - h_g) - \frac{V_i^2}{2g_o J} \right] \eta w_p . \qquad (32)$$

Equation (13) is rewritten here for convenience:

$$\dot{m} = \frac{F \eta w_p V_i^2}{2g_o JHf} e^{-3\rho_L \delta / 2\rho_p d_p} + \dot{m}_{th} . \qquad (13)$$

Substituting into Equation (13) the expression for $\dot{m}_{th}$ in Equation (31) and rearranging yields

$$\dot{m} - \dot{m}_o = [1 - H_g] \frac{F \eta w_p V_i^2}{2g_o JHf} e^{-3\rho_L \delta / 2\rho_p d_p} - \Delta H_w / H_e , \qquad (33)$$

where

$$H_g = \frac{Hf}{H_e F} + \frac{0.6\, c_g f\,(T_e - T_w)}{H_e} . \qquad (34)$$

It was shown previously that

$$\frac{\delta}{\delta_o} = \sqrt{\frac{\dot{m}}{\dot{m}_o}} .$$

Using this expression and rearranging Equation (33) yields

$$\frac{\rho_L \delta_o}{\rho_p d_p} = -\ln \left\{ \frac{2g_o JHf\,[(\dot{m} - \dot{m}_o) + \Delta H_w / H_e]}{F \eta w_p V_i^2\,[1 - H_g]} \right\}^{\frac{2}{3}} \left\{ \frac{\dot{m}}{\dot{m}_o} \right\}^{-1/2} , \qquad (35)$$

which is similar to the equation used to correlate the data from the 3.5 AHT tests. This last expression is used to estimate the effect of atmospheric-moisture particles on a re-entry vehicle along both a 3000-NM trajectory and a 500-NM trajectory.

As was seen in the preceding discussion, a number of assumptions had to be made in order to estimate the thermal effect of particles on the erosion rate. It will be seen later in this report that the cooling effect is computed to be of the same order of magnitude as the damage effect. Therefore, it would be desirable to conduct an experiment where particle thermal effects are simulated. For example, this could be some sort of small-scale flight test. The purpose of the experiment would be to shed light on the actual physical mechanisms involved in the energy transfers discussed herein.

Liquid-Melt Thickness

It will be recalled that the parameter $\rho_p d_p / \rho_L \delta_o$ exerts a strong influence on the effect of particles on the erosion rate of a melting body. The value of the product $\rho_p d_p$ may be obtained from information available for the particles, whereas the product $\rho_L \delta_o$ must be obtained from other considerations. The product $\rho_L \delta_o$ was obtained for Micarta specimens and the conditions in the 3.5 AHT exhaust jet by plotting the data in an appropriate manner, as shown in Figure 9. The value of δ_o from this analysis was found to agree qualitatively with measurements made on slices of fired specimens. As data are not available for free flight, the product $\rho_L \delta_o$ cannot be determined in the same manner as for the 3.5 AHT experiments. A scaling method was utilized to determine the average ratio of $\rho_L \delta_o$ for a Micarta nose cone in free flight to $\rho_L \delta_o$ for Micarta specimens in the 3.5 AHT exhaust. The development of the scale factor used will be presented now.

The shear stress at the liquid-melt-gas boundary-layer interface is given by

$$(\tau_g)_i = (\rho_e u_e^2/2)\, c_f = (\tau_L)_i . \tag{36}$$

It is assumed that the velocity varies linearly in the melt layer, so that

$$(\tau_L)_i = \left(\frac{u_i}{\delta_o}\right)(\mu_L) . \tag{37}$$

Following the example of Lees[27], the conservation of mass for the melt layer for axially symmetric flow is

$$2\pi r_o (1 - f)\, \dot{m}_o = \frac{d}{dx}\left(2\pi r_o \int_o^{\delta_o} \rho_L u_L dy\right) \tag{38}$$

where x is measured along the surface, and y is the coordinate normal to the surface.

For an incompressible liquid melt,

$$\int_o^{\delta_o} \rho_L u_L dy = \Lambda \rho_L u_i \delta_o \tag{39}$$

where $\Lambda = 1/2$ for a linear variation of velocity in the y-direction within the melt.

Therefore, continuity may be expressed as

$$r_o (1 - f) \dot{m}_o = \left(\frac{dr_o}{dx}\right) \Lambda \rho_L u_i \delta_o, \tag{40}$$

assuming that, for small distances along the melt, ρ_L, u_i, and δ_o are not functions of x. This assumption is not considered to be critical, because (1) large variations are not expected and (2) the effect of considering these quantities as variables will tend to cancel when ratios are taken, later in this discussion.

For a spherical body,

$$r_o = R \sin \theta$$

and

$$x = R\theta.$$

The function $\frac{dr_o}{dx}$ may be expressed as

$$\frac{dr_o}{dx} = \frac{dr_o}{d\theta} \frac{d\theta}{dx},$$

but for a sphere

$$\frac{dr_o}{d\theta} = R \cos \theta,$$

and

$$\frac{d\theta}{dx} = \frac{1}{R},$$

which leads to

$$\frac{dr_o}{dx} = \cos \theta.$$

The equation of continuity may now be rewritten as

$$R \tan \theta (1 - f) \dot{m}_o = \Lambda \rho_L u_i \delta_o. \tag{41}$$

This expression may be solved for the velocity at the gas-liquid-melt-layer interface, yielding

$$u_i = \frac{R \tan \theta (1 - f) \dot{m}_o}{\Lambda \rho_L \delta_o}. \tag{42}$$

Combining this with the two expressions [Equations (36) and (37)] for the shear stress at the melt-gas interface yields

$$\left(\frac{p_e u_e^2}{2}\right) c_f = \frac{R \tan\theta\,(1-f)\,\dot{m}_o \mu_L}{\Lambda \rho_L \delta_o^2}\,, \tag{43}$$

which can be solved for $\rho_L \delta_o$ to yield

$$\rho_L \delta_o = \sqrt{\frac{2R \tan\theta\,(1-f)\,\dot{m}_o \mu_L \rho_L}{\Lambda \rho_e u_e^2 c_f}} \tag{44}$$

The following assumptions are made to relate flow quantities in the 3.5 AHT test setup to free-flight conditions:

(1) $\Lambda_t = \Lambda$

(2) $(c_f)_t = c_f$

(3) $(\rho_L)_t = \rho_L$

(4) $\dfrac{(p_e u_e^2)_t}{\rho_e u_e^2} = \dfrac{p_{o_t}}{p_o}$

It is obvious that each of the assumed qualities is at least approximately correct.

If the comparison between test and flight conditions is carried out to the same value of the angle, θ, then

$$\frac{\rho_L \delta_o}{(\rho_L \delta_o)_t} = \sqrt{\left(\frac{R}{R_t}\right)\left(\frac{p_{o_t}}{p_o}\right)\left(\frac{\mu_L}{\mu_{L_t}}\right)\left(\frac{\dot{m}_o}{\dot{m}_{o_t}}\right)}\,, \tag{45}$$

which is the desired ratio.

As was stated previously, the value of $(\rho_L \delta_o)_t$ was determined for the test conditions on the basis of the experimental data. Using the predetermined value of $(\rho_L \delta_o)_t$, it becomes possible to compute the average value of $\rho_L \delta_o$ for flight conditions, and then $\rho_p d_p / \rho_L \delta_o$ for flight conditions.

The effect of vehicle deceleration was neglected in the preceding analysis. This is considered to be valid on the basis of the results presented by Tellep[28]. Tellep theoretically analyzed the problem of the effect of vehicle deceleration on the liquid-melt properties, and showed that the effect of vehicle deceleration on the melt thickness is small when the shear stress is high. Recent theoretical results reported by Fanucci and Lew[29] agree qualitatively with those of Tellep. These results indicate that the effect of deceleration on the melt layer is felt at some distance from the stagnation point.

An interesting point that might be mentioned now is that the ratio $\rho_L \delta_o / (\rho_L \delta_o)_t$ might be considered to be one of the parameters that should be simulated in ground tests in order to obtain similarity with free-flight conditions. A value of the ratio of

unity expresses the condition that the average melt thickness attained in the experiment is approximately the same as that attained in free flight. Furthermore, if the average melt thickness is obtained for a particular set of operating conditions in a ground-test facility, it becomes a simple matter to estimate the average melt thickness at various flight conditions for the same material.

For the purposes of the present investigation, wherein particle effects are being studied, it becomes desirable to conduct experiments where the value of $\rho_p d_p / \rho_L \delta_o$ is of the same order of magnitude as the value to be expected for free-flight conditions. The constancy of this ratio approximately insures the constancy of the ratio of solid-body impact energy to initial particle energy on the basis of the liquid-melt protection mechanism discussed previously in this report. On the basis of the preceding derivation, it is seen that

$$\left(\frac{\rho_p d_p}{\rho_L \delta_o}\right)_t \Bigg/ \left(\frac{\rho_p d_p}{\rho_L \delta_o}\right) = \frac{(\rho_p d_p)_t}{\rho_p d_p} \sqrt{\left(\frac{R}{R_t}\right)\left(\frac{p_{o_t}}{p_o}\right)\left(\frac{\mu_L}{\mu_{L_t}}\right)\left(\frac{\dot{m}_o}{\dot{m}_{o_t}}\right)} \qquad (46)$$

This might be considered to be a similarity parameter for particle impact experiments.

Calculations for Typical Re-Entry Profiles

Calculations were carried out to determine the effects of atmospheric-moisture particles along the 3000-NM trajectory and the 500-NM trajectory mentioned earlier. The various common clouds listed in Table 2 were chosen for this calculation, and the change in erosion rate was computed at various altitudes within these clouds. Environmental and ablation data for Micarta 259-2 were available for these trajectories from ABMA. The computations of the ratio $\rho_L \delta_o / (\rho_L \delta_o)_t$ are discussed first; and then the computations of the particle effects are discussed. Erosion calculations are discussed, assuming the particle cooling effect discussed previously and also assuming that there is no particle cooling effect.

The test conditions chosen for comparison with free flight are R_t = 2.6 inches, p_{o_t} = 8.3 atmosphere, $\dot{m}_{o_t}$ = 1.5 g/sec = 0.074 g/sec-cm^2 for Micarta 259-2, and a melt temperature of approximately 3000 R, leading to $\mu_{L_t} = 10^{1.9}$ poises for Corning Glass E, which is the glass reinforcer for the Micarta. It is to be recalled that $(\rho_L \delta_o)_t$ for these test conditions was found from the data to be 77.7 micron-g/cc.

Data obtained from ABMA supplied $\dot{m}_o$ at each flight condition considered. A value of p_o was computed, for each flight condition considered, on the basis of the known altitude and Mach number for the trajectory. The usual computation techniques were employed for the calculation of p_o. Thermodynamic data, as presented by Korobkin and Hastings[30], were used in the calculations. This computation also yielded shock-layer temperatures, and these were in turn, used, to make a rough estimate of the melt-layer temperatures. The melt-layer temperature was used to determine μ_L at each flight condition.

Figure 13 shows the results of the calculations of $[\rho_L \delta_o / (\rho_L \delta_o)]$. In this figure, $\rho_L \delta_o / (\rho_L \delta_o)_t$ is plotted as a function of altitude. It is recalled that $(\rho_L \delta_o)_t$ and ρ_L are constant; hence, the figure shows the variation of the average melt-layer thickness as a function of altitude. It is seen that the melt-layer thickness first decreases with

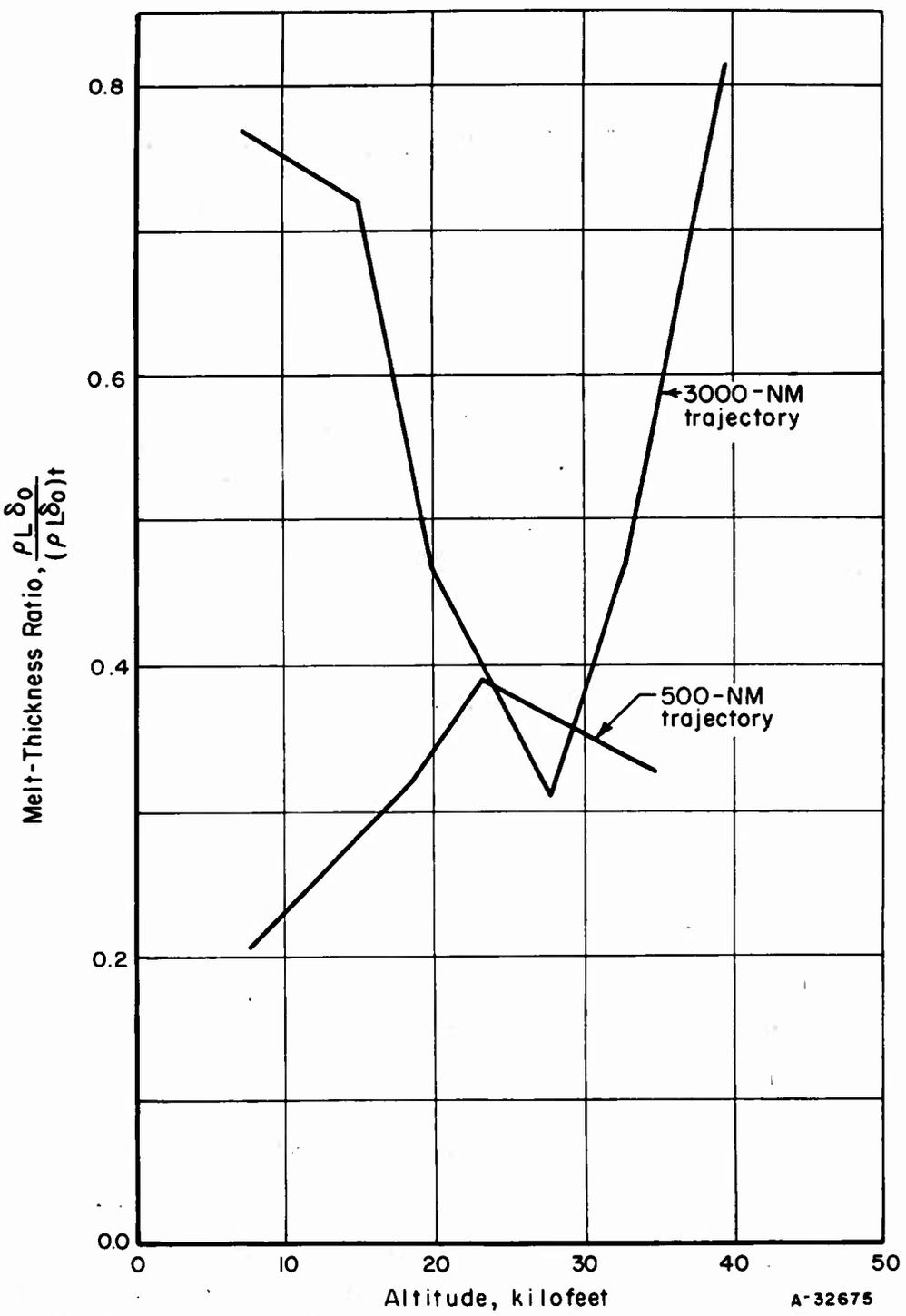

FIGURE 13. MELT-THICKNESS RATIO AS A FUNCTION OF ALTITUDE FOR MICARTA ALONG THE 3000-NM TRAJECTORY AND THE 500-NM TRAJECTORY

decreasing altitude, reaches a minimum at about 28,000 feet (8.5 kilometers), and then increases with decreasing altitude for the 3000-NM trajectory.

A physical explanation of the results plotted in Figure 13 is that, from an altitude of 40,000 feet down to 28,000 feet, the ablation rate is decreasing rapidly, and this controls the melt thickness down to 28,000 feet. Below this altitude, the ablation rate is relatively constant and the melt thickness increases primarily because of a decreasing stagnation pressure. The ablation rate below 25,000-foot altitude along the 500-NM trajectory continually decreases, so that no increase in melt thickness with decreasing altitude was found.

The value of $\rho_L \delta_o$ in Equation (45) should increase slightly with increasing vehicle velocity at constant altitude, because $\dot{m}_o$ is probably a stronger function of U_∞ than p_o.

Recalling the melt-protection mechanism discussed previously, it is seen that for the 3000-NM trajectory, the minimum protection is offered at the 28,000-foot altitude. That is, at this altitude, the 3000-NM vehicle is most vulnerable to particle-impact damage.

Calculations of the effect of particles on a re-entry vehicle were carried out along the 3000-NM and the 500-NM trajectories, considering passage through the various clouds listed in Table 2. Because of the large frontal area and low density of the cloud elements found in the high clouds listed in Table 2, impact with these elements was not considered. It is probably safe to assume that these cloud elements are deflected and evaporated by the shock-layer gases. The opposite case was assumed for the other cloud elements listed in Table 2. That is, for cloud elements found in middle, low, and vertical clouds, it was assumed that the impaction efficiency on the vehicle was 100 per cent, that the particles do not evaporate in the shock layer, and also that they do not break up in the shock layer.

The calculations were made both using the assumption that the particles act as a heat sink in the manner discussed earlier in this section and also using the assumption that the particle cooling effect is negligible. The results of both sets of computations are presented.

Assuming that the particle cooling effect is important, calculations were made using the equation derived earlier in this discussion:

$$\frac{\rho_L \delta_o}{\rho_p d_p} = -\ln \left\{ \frac{2 g_o J H f \left[(\dot{m} - \dot{m}_o) + \Delta H_w / H_e \right]}{F \eta w_p V_i^2 \left[1 - H_g \right]} \right\}^{\frac{2}{3} \left(\frac{\dot{m}}{\dot{m}_o} \right)^{-1/2}} , \qquad (35)$$

where the values of $\Delta H_w / H_e$ and H_g were determined through use of the methods described earlier. The value of $\rho_L \delta_o$ was obtained from Figure 13; ρ_p was taken as 1 g/cc; and d_p was taken from Table 2 for the various clouds considered.

The computation is iterative in nature. The left-hand side is computed, and then various values of $\dot{m}/\dot{m}_o$ are assumed in order to allow computation of the right-hand side. When the value of the right-hand side of the equation that matches the left-hand side is computed, the calculation stops and the value of $\dot{m}/\dot{m}_o$ used in the calculation

TABLE 3. RESULTS OF CALCULATIONS ON THE EFFECT OF MOISTURE PARTICLES ON A RE-ENTRY VEHICLE FOR A 3000-NM TRAJECTORY

Altitude, kilometers	Cloud Type	Average Particle Size, microns	Concentration of Particles, cc	Change in Ablation Rate (Heat Sink), $\dot{m}/\dot{m}_0$	Change in Ablation Rate (No Heat Sink), $\dot{m}/\dot{m}_0$
12	Altostratus or altocumulus	11	5×10^2	1.00	1.00
10	Altostratus or altocumulus	11	5×10^2	1.08	1.12
8.5	Altostratus or altocumulus	11	5×10^2	1.42	1.74
8.5	Nimbostratus	13.5	5×10^2	1.99	2.49
6	Altostratus or altocumulus	11	5×10^2	0.72	1.16
6	Nimbostratus	13.5	5×10^2	0.85	1.44
6	Cumulus congestus	15	1×10^2	1.01	1.27
4.6	Altostratus or altocumulus	11	5×10^2	0.35	1.01
4.6	Nimbostratus	13.5	5×10^2	0.33	1.07
4.6	Cumulus congestus	15	1×10^2	0.33	1.20
2.2	Altostratus or altocumulus	11	5×10^2	0.24	1.01
2.2	Nimbostratus	13.5	5×10^2	0.18	1.02
2.2	Cumulus congestus	15	1×10^2	0.55	1.01
2.2	Stratus	13	5×10^2	0.17	1.02
2.2	Stratocumulus	8	5×10^2	0.62	1.00

is taken to be the sought-for ratio of the ablation rate with impact to ablation rate without impact. The results of these computations for the 3000-NM trajectory are presented in Table 3.

Also shown in Table 3 are the results of the calculations made where the heat-sink effect was assumed to be negligible. The procedure for these calculations was similar to the one just outlined, except that here

$$\Delta H_w / H_e = 0$$

and

$$H_g = \frac{0.6\, c_g (T_e - T_w)}{H_e} .$$

It is evident from the results presented in Table 3 that there is a significant difference between the results obtained using the heat-sink assumption and those obtained by neglecting the heat-sink effect. This is especially true at the lower altitudes, where the heat-sink effect may even lead to a decrease in the ablation rate as a result of particle impact. It may also be noted that, at the 12-kilometer altitude, the effect of particles is found to be negligible. As altitude decreases, damage increases, reaches a maximum, and then decreases. The primary reason for this is the variation in melt thickness shown in Figure 13. The damage thus appears to be a strong function of melt thickness. This leads to the conclusion that, when hypersonic velocities are maintained at low altitude, which might lead to thin melt layers for various materials, the damage produced by atmospheric-moisture particles may increase erosion rates by a factor of 2 or more. It might also be noted that, at the higher altitudes, where thermal ablation rates are high, the smaller change in ablation rates shown in Table 3 could lead to higher weight losses than greater fractional increases in erosion at lower altitudes.

The divergence in the results of calculations using the two alternative assumptions described previously accents the statement made earlier in this section with regard to the need for closer examination of particle heat-sink effects.

The results of calculations made along the severe 500-NM trajectory are summarized in Table 4.

TABLE 4. RESULTS OF CALCULATIONS ON THE EFFECT OF MOISTURE PARTICLES ON A 500-NM RE-ENTRY VEHICLE DURING FLIGHT THROUGH A NIMBOSTRATUS CLOUD

Altitude, kilometers	Change in Ablation Rate, $\dot{m}/\dot{m}_0$
10.9	1.40
9	1.32
7.2	1.22
5.5	1.31
3.9	1.43
2.3	1.78

The erosion rates shown in Table 4 were computed assuming that the particles had no cooling effect. The calculations indicated that the total erosion of the re-entry portion of the 500-NM missile considered might increase by 8 per cent as a result of flight through a nimbostratus cloud extending in altitude between 10.9 kilometers and 2.3 kilometers.

CONCLUSIONS AND RECOMMENDATIONS

The emphasis during the present study has been on the effects produced by impacts between atmospheric-moisture particles in the form of cloud elements and a melting re-entry body. The conclusions of this study with respect to physical phenomena, magnitude of effects, and test facilities are presented below. Recommendations for future researches follow the presentation of the conclusions.

This study showed that the melt layer present on Micarta nose cones during ablation offers a certain amount of protection against the damaging effects of particle impact. Particles strike the melt layer and are decelerated by it prior to impact onto the solid body. The damage produced by the impact appears to depend on the energy of the particle at the solid-liquid melt-layer interface. Both solid- and liquid-particle impacts produce the same effect on Micarta. Calculations carried out along sample missile trajectories showed that the damage produced by particle impacts depended strongly on the liquid-melt-layer thickness.

The calculations carried out along sample trajectories indicated that, under certain conditions, the instantaneous ablation rate of a nose cone may be increased by as much as a factor of 2 during flight through a cloud. The over-all amount of material eroded during re-entry along one of the sample trajectories was found to be increased by 8 per cent as a result of flight through a nimbostratus cloud. The particle-impact problem will generally become more severe as the missile trajectories are changed to include longer periods of time during which hypersonic velocities are maintained at altitudes of less than 12 kilometers. This would come about with ballistic missiles having higher weight-drag ratios and with hypersonic low-altitude missiles. Particle-impact effects also become more severe as smaller nose radii are utilized for re-entry vehicles. Some of the materials currently being investigated for high-heat-flux applications do not form a melt layer and therefore might be more vulnerable to particle-impact damage than those that do melt during ablation.

In certain of the tests in the 3.5 AHT facility, ablation rates as great as 17 times the ablation rates resulting from thermal effects alone were obtained using particles as small as 88 microns in diameter and Micarta test specimens. It might be possible to optimize the damage and design a relatively low-cost missile-defense system around the particle-impact phenomenon.

A rocket-engine test facility, such as the 3.5 AHT facility, can be used for simulation of particle impaction on aerodynamically shaped melting bodies. Those aspects of the impact phenomena not simulated in a rocket-engine facility are impaction efficiencies, droplet breakup, droplet evaporation, and particle cooling effects. These aspects may be studied analytically or in a limited number of flight tests, and the results applied to the interpretation of rocket-engine test results.

Several areas of recommended future research are, briefly:

(1) Detailed theoretical analysis of the motion of particles in the shock layer and the resulting impaction efficiencies and impact velocities

(2) Analytical and/or experimental studies of the cooling effect produced by moisture-particle impacts on a melting body

(3) Experimental studies of the effect of heat fluxes higher than those produced in the 3.5 AHT facility on particle-impact phenomena

(4) A study of hypersonic velocity impacts of large particles, such as rain drops, on melting aerodynamic surfaces

(5) A study of the missile-defense implications of the results presented herein.

REFERENCES

(1) Li, T. Y., and Geiger, R. E., "Stagnation Point of a Blunt Body in Hypersonic Flow", Journal of the Aeronautical Sciences, Vol 24, No. 1, January, 1957, p 25.

(2) Putnam, A. A., and Ungar, E. W., "Basic Principles of Combustion-Model Research", Journal of Engineering for Power, ASME Transactions, Vol 81, Series A, No. 4, October, 1959, p 383.

(3) Scala, S. M., "Aerothermochemical Scaling Laws for Ablation Model Testing", (Unclassified), in "Re-Entry Ablation", General Electric Report 57SD736, October, 1957. (Secret).

(4) Boison, J. C., and Curtiss, H. A., "An Experimental Investigation of Blunt Body Stagnation Point Velocity Gradient", American Rocket Society Journal, Vol 29, No. 2, February, 1959, p 130.

(5) Golovin, M. N., and Putnam, A. A., "The Inertial Impaction of Small Particles", AEDC TN 58-36, ASTIA Document No. AD 157135, January, 1958.

(6) Agosta, V. D., "A Theoretical Investigation on the Use of Combustion Products for the Simulation of Hypersonic Flow", WADC TN 59-81, ASTIA Document No. AD 211916, March, 1959.

(7) Nagamatsu, H. T., Geiger, R. E., and Sheer, R. E., "Hypersonic Shock Tunnel", American Rocket Society Journal, Vol 29, No. 5, May, 1959, p 332.

(8) McDonough, J. P., and Hegge, E. N., "Observations of Projectile Impacts of Sand Particles at Velocities Ranging From 2900 Ft/Sec to 7000 Ft/Sec", Watertown Arsenal Laboratories TR 892/17, ASTIA Document No. AD 200194, July, 1958.

(9) McDonough, J. P., personal communication.

(10) "NASA-ARPA Re-entry Detection Research", Astronautics, Vol 4, No. 8, August, 1959, p 29.

(11) Sutton, G. W., "The Hydrodynamics and Heat Conduction of a Melting Surface", Journal of the Aeronautical Sciences, Vol 25, No. 1, January, 1958, p 29.

(12) Friedlander, S. K., "Particle Impaction on Spheres at High Mach Numbers", American Rocket Society Journal, Vol 29, No. 4, April, 1959, p 296.

(13) Lighthill, M. J., "Dynamics of a Dissociating Gas, Part I - Equilibrium Flow", Journal of Fluid Mechanics, Vol 2, 1957, p 1.

(14) Engel, O. G., "Mechanism of Rain Erosion, Part 8 - On The Breakup of a Water-Drop in the Zone Behind a Detached Shock Wave", WADC TR 53-192, ASTIA Document No. AD 101271, May, 1956.

(15) Engel, O. G., "Mechanism of Rain Erosion, Part 9 - Observation of the Fragmentation of Waterdrops in a Zone Behind an Air Shock", WADC TR 53-192, ASTIA Document No. AD 130909, July, 1957.

(16) Engel, O. G., personal communication, May 8, 1959.

(17) Hinze, J. O., "Forced Deformations of Viscous Liquid Globules", Applied Scientific Research, A, Vol 1, 1949, p 263.

(18) Hinze, J. O., "Critical Speeds and Sizes of Liquid Globules", Applied Scientific Research, A, Vol 1, 1949, p 273.

(19) Lord Rayleigh, The Theory of Sound, Vol II, Dover Publications, 1945, p 371.

(20) Hanson, A. R., Domich, E. G., and Adams, H. S., "An Experimental Investigation of Impact and Shock-Wave Break-Up of Liquid Drops", University of Minnesota, Rosemount Aero Lab, Research Report 125, November, 1955.

(21) Masugi, N. I., "Theoretical and Experimental Study of the Deformation and Atomization of a Liquid Drop in a High-Velocity Gas Stream", ARS Preprint No. 355-56, presented at 11th Annual Meeting, November 26-30, 1956.

(22) Lane, W. R., "Shatter of Drops in Streams of Air", Industrial and Engineering Chemistry, Vol 43, No. 6, June, 1951, p 1312.

(23) Jakob, M., Heat Transfer, Vol. 1, John Wiley & Sons, Inc., New York, 1949, pp 270-281.

(24) McAdams, W. H., Heat Transmission, McGraw-Hill Book Company, Third Edition, 1954, p 265.

(25) Roberts, L., "A Theoretical Study of Stagnation-Point Ablation", NACA TN 3492, November, 1955.

(26) Eckert, E.R.G., Introduction to the Transfer of Heat and Mass, McGraw-Hill Book Company, New York, 1950, p 140.

(27) Lees, L., "Similarity Parameters for Surface Melting of a Blunt-Nosed Body in a High-Velocity Gas Stream", American Rocket Society Journal, Vol 29, No. 5, May, 1959, p 345.

(28) Tellep, D. M., "The Effect of Vehicle Deceleration on a Melting Surface", in General Research in Flight Sciences, Vol 1, Lockheed Aircraft Corporation, LMSD-48381, ASTIA Document No. AD 210401, January, 1959, p 115.

(29) Fanucci, J. B., and Lew, H. G., "Effect of Mass Transfer and Body Forces on Two-Phase Boundary Layers", General Electric Report R59SD380, April, 1959.

(30) Korobkin, I., and Hastings, S. M., "Mollier Chart for Air in Dissociated Equilibrium at Temperatures of 2,000 K to 15,000 K", NAVORD Report 4446, ASTIA Document No. AD 135454, May, 1957.

EWU/all

SYMBOLS

A_p = cross-sectioned area of particle

B = arbitrary coefficient

b_1 = coefficient of first-power term in Taylor series expansion of gas velocity around the stagnation point

C = velocity coefficient, defined by Equation (26)

C_D = drag coefficient

c_f = local friction coefficient

c_g = specific heat of the gases evolved from decompositon of the plastics

d_p = particle diameter

E_R = ablation-energy parameter, defined by Equation (22)

F = fraction of particle impact kinetic energy transmitted to the plastic filler

F_p = force on particle

f = mass fraction of plastic filler in the undamaged material

g_c = consistent conversion factor

H = energy necessary to start the decomposition of the plastic filler

H_e = effective heat of ablation

H_g = energy ratio, defined by Equation (34)

ΔH_w = energy absorbed by particles, as defined in Equation (32)

$\Delta H_w'$ = energy absorbed by particles in gas-boundary layer-melt layer-solid body system

h = particle enthalpy per unit weight

h' = heat-transfer coefficient

h_{fg} = latent heat of vaporization of water at shock-layer pressure

J = conversion factor to energy units

K = impaction parameter

KE = kinetic energy

k = thermal conductivity

L = characteristic length, e.g., nozzle length, nozzle exit-to-specimen distance

M = Mach number

m_p = particle mass

$\dot{m}$ = total ablation rate

$\dot{m}_l$ = rate at which material crosses the liquid-solid interface

$\dot{m}_p$ = portion of ablation rate due to particle impact

$\dot{m}_{Stored}$ = rate at which the mass contained in the melt layer changes

$\dot{m}_{th}$ = portion of ablation rate due to heat transfer

p = static pressure

p_o = stagnation pressure

R = nose radius of curvature

Re = Reynolds number

r_o = distance measured radially from axis of body

S = particle displacement

T = temperature

t = time

$\bar{t}$ = λ/U_∞ = characteristic time

U_∞ = free-stream velocity

u = velocity in x-direction

V = particle velocity

V_r = relative velocity between particle and gas

w_p = mass flow rate of particles

α = $\dfrac{18\,\mu_g\,L}{\rho_p d_p^2 u_F}$

β = function of α defined in Equation (B-9)

γ = ratio of specific heats

δ = average melt-layer thickness

ϵ = index of variation from uniform particle velocity

ζ = distance defined by Figure C-1

η = impaction efficiency

θ = angle measured from stagnation point

Λ = constant defined by Equation (39)

λ = shock-detachment distance

μ = viscosity

π = 3.14...

ρ = density

τ = shear stress

ψ = parameter defined by Equation (B-14)

Subscripts

E = condition at x' = o

e = edge of gas boundary layer

F = nozzle exit gas velocity

f = solid-liquid interface

g = gas

i = gas-liquid interface

L = liquid

o = "no particle" impact condition

p = particle

s = shock-wave location

t = test conditions

x = component in x-direction

y = component in y-direction

z = component in z-direction

SYMBOLS

A_p = cross-sectioned area of particle

B = arbitrary coefficient

b_1 = coefficient of first-power term in Taylor series expansion of gas velocity around the stagnation point

C = velocity coefficient, defined by Equation (26)

C_D = drag coefficient

c_f = local friction coefficient

c_g = specific heat of the gases evolved from decompositon of the plastics

d_p = particle diameter

E_R = ablation-energy parameter, defined by Equation (22)

F = fraction of particle impact kinetic energy transmitted to the plastic filler

F_p = force on particle

f = mass fraction of plastic filler in the undamaged material

g_c = consistent conversion factor

H = energy necessary to start the decomposition of the plastic filler

H_e = effective heat of ablation

H_g = energy ratio, defined by Equation (34)

ΔH_w = energy absorbed by particles, as defined in Equation (32)

$\Delta H_w'$ = energy absorbed by particles in gas-boundary layer-melt layer-solid body system

h = particle enthalpy per unit weight

h′ = heat-transfer coefficient

h_{fg} = latent heat of vaporization of water at shock-layer pressure

J = conversion factor to energy units

K = impaction parameter

KE = kinetic energy

k = thermal conductivity

L = characteristic length, e.g., nozzle length, nozzle exit-to-specimen distance

M = Mach number

m_p = particle mass

$\dot{m}$ = total ablation rate

$\dot{m}_l$ = rate at which material crosses the liquid-solid interface

$\dot{m}_p$ = portion of ablation rate due to particle impact

$\dot{m}_{Stored}$ = rate at which the mass contained in the melt layer changes

$\dot{m}_{th}$ = portion of ablation rate due to heat transfer

p = static pressure

p_o = stagnation pressure

R = nose radius of curvature

Re = Reynolds number

r_o = distance measured radially from axis of body

S = particle displacement

T = temperature

t = time

$\bar{t}$ = λ/U_∞ = characteristic time

U_∞ = free-stream velocity

u = velocity in x-direction

V = particle velocity

V_r = relative velocity between particle and gas

w_p = mass flow rate of particles

α = $\dfrac{18\,\mu_g\,L}{\rho_p d_p^{\,2} u_F}$

β = function of α defined in Equation (B-9)

γ = ratio of specific heats

δ = average melt-layer thickness

ϵ = index of variation from uniform particle velocity

ζ = distance defined by Figure C-1

η = impaction efficiency

θ = angle measured from stagnation point

Λ = constant defined by Equation (39)

λ = shock-detachment distance

μ = viscosity

π = 3.14...

ρ = density

τ = shear stress

ψ = parameter defined by Equation (B-14)

Subscripts

E = condition at x′ = o

e = edge of gas boundary layer

F = nozzle exit gas velocity

f = solid-liquid interface

g = gas

i = gas-liquid interface

L = liquid

o = "no particle" impact condition

p = particle

s = shock-wave location

t = test conditions

x = component in x-direction

y = component in y-direction

z = component in z-direction

APPENDIX A

PERFORMANCE OF THE 3.5 AHT ENGINE

APPENDIX A

PERFORMANCE OF THE 3.5 AHT ENGINE

The injector used in the 3.5 AHT engine was especially designed to allow the injection of a particle-kerosene slurry for erosion studies. The oxidizer, 90 per cent hydrogen peroxide, is passed through a catalyst bed, where it decomposes to oxygen and steam with an accompanying energy release. The particle-kerosene slurry is injected along the axis of the burner, and clear kerosene is injected radially outward through eight holes in the injector into the annular stream of decomposed hydrogen peroxide. The decomposed products mix with the clear, radially injected kerosene, and then flow into the combustion chamber, where they can mix with the axially injected slurry.

As a physical model of the processes occurring in the combustion chamber, it was hypothesized that slurry fuel injected axially into the chamber does not burn, and the fuel injected radially burns with an efficiency of 95 per cent. The flame produced by the oxidation of the radially injected fuel, thus constituting the principal combustion flame, will be referred to hereafter as the "pilot" flame. Approximate performance calculations were made on the basis of this assumed model. The method of calculation is outlined below, by which the performance of the motor was predicted prior to any test firings.

A weight flow of slurry, a chamber pressure, and a pilot-flame mixture ratio were selected, and 95 per cent of the theoretical pilot-flame temperature was determined from thermodynamic data. The fraction of the total propellant weight flow that consists of slurry was assumed. An average specific heat of 0.45 Btu/lb_m - °R was chosen for the slurry and an average specific heat of 0.6 Btu/lb_m - °R was chosen for the pilot-flame combustion products. An average temperature was then computed for the mixture of slurry and combustion products on the basis of the assumption that the slurry is heated to the combustion-chamber temperature without any accompanying exothermic chemical reactions. The resulting computed average chamber temperature was then reduced by 11 per cent to account for losses resulting from wall heat losses and the cracking and change of phase of the kerosene in the slurry. The 11 per cent figure was chosen because it allowed the exact matching of theoretically and experimentally determined combustion temperatures for one operating condition for a similar injector installed in a smaller ABMA engine for which some operating experience was available. The chamber temperature, calculated by the method described above, was used to compute the theoretical total weight flow rate at the throat of the exhaust nozzle, neglecting the small effect of the particles on the average molecular weight of the combustion products. Using this weight flow, a new weight fraction of slurry was computed. The calculation procedure was then repeated on the basis of the new weight fraction of slurry. When a weight fraction of slurry was found that satisfied the assumed value for that calculation, the computations were considered to be completed and the chamber temperature found for that calculation was taken as a final value. The associated propellant flow rates could be easily obtained from the calculated over-all flow rate, the slurry flow rate, and the pilot-flame mixture ratio. The per cent of theoretical characteristic exhaust velocity, c*, could be obtained easily by taking the square root of the ratio of the calculated chamber temperature to the theoretical temperature for the over-all mixture ratio. The small differences in molecular weight were neglected. The results of these calculations were compared with the data obtained from nine calibration firings of the 3.5 AHT engine.

Figure A-1 summarizes the performance data obtained from the calibration firings. It is a plot of per cent of theoretical characteristic exhaust velocity, c*, as a function of over-all mixture ratio (pounds of H_2O_2 per pound of kerosene). The curves shown on the plot were calculated theoretically by the procedure described above, whereas the points shown in the figure were calculated from experimental data for two fractional weight flows of particles and various over-all mixture ratios. The slurry-fuel rate was held constant and the composition of the slurry varied in order to vary the particle flow rate. All of the particles used in the calibration firings were 500-grit, fused aluminum oxide. The 500-grit fused aluminum oxide is approximately spherical and has an average particle diameter of 16 microns.

As might be expected, there is considerable scatter in the data. This results from both experimental difficulties and the limiting assumptions necessary in the theoretical calculation of temperatures and c* values. However, it appears that the general trends indicated by the theoretical curves are followed by the experimental data. The difference between the 0.625 and the 5 per cent curves is too small to be shown by the experimental data. This correlation indicates that the assumption that the fuel in the slurry does not burn within the chamber is approximately correct, and that the assumption is adequate for first-order calculations of combustion temperature. It was found that a maximum flame temperature of 3800 R could be obtained at an over-all mixture ratio of 5.5:1. This mixture ratio yields the highest possible combustion temperature, as it corresponds to a stoichiometric pilot flame.

In addition to the combustion studies, an attempt was made during the calibration to obtain the distribution of both temperature and particles in the exhaust jet. This was done by exposing, during three of the calibration firings, a steel cross to which nine small steel rods were welded. None of the three specimens tested showed any particular pattern that might have resulted from a nonuniform distribution of particles or temperature.

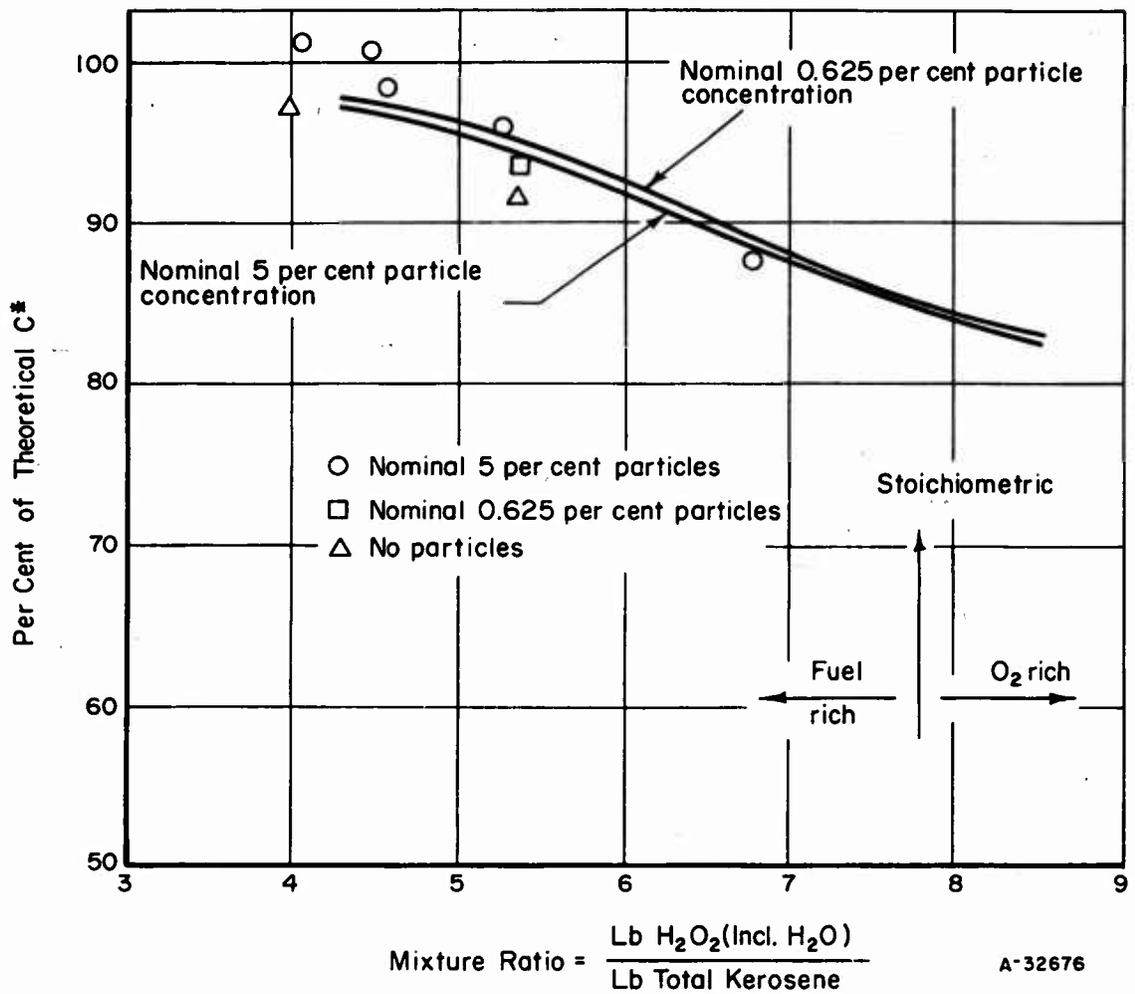

FIGURE A-1. VARIATION OF PER CENT OF THEORETICAL CHARACTERISTIC EXHAUST VELOCITY AS A FUNCTION OF OVER-ALL MIXTURE RATIO IN THE 3.5 AHT FACILITY

APPENDIX B

ACCELERATION OF PARTICLES IN A ROCKET EXHAUST JET

APPENDIX B

ACCELERATION OF PARTICLES IN A ROCKET EXHAUST JET

In order to simulate the erosion of a re-entry body by atmospheric-moisture particles, a technique was used wherein inert particles were accelerated in a rocket exhaust nozzle and then made to impinge on a model nose cone. The actual particle velocity at the specimen location must be known in order to allow interpretation of test results. Following a derivation of the equation of motion for particles in a rocket exhaust jet, exact solutions are presented for the two cases where the gas velocity, u, is a linear function of x and where the gas velocity is constant in x. Then an approximate solution is obtained for the case where the gas velocity is much greater than the particle velocity. Finally, the results obtained are applied to the numerical computations of aluminum oxide particle velocities at the specimen location in the 3.5 AHT exhaust jet.

The x-momentum equation for a single particle immersed in an accelerating gas stream is

$$F_{p_x} = \frac{d}{dt}(m_p V_x), \qquad \text{(B-1)}$$

where the coordinate system is chosen such that x is the axial direction in the nozzle and the origin is located at the initial point in the system that is considered, normally the nozzle entrance.

The following assumptions will be made initially: (1) the fluid flow is one-dimensional; (2) the particles are spherical; (3) Stokes drag law is applicable, thus implying a Reynolds number with respect to the particle of the order of unity; (4) the particle density is much greater than the gas density; and (5) the force resulting from the pressure gradient in the x-direction is negligible. The assumed drag law is improved later in this discussion when the approximate solution is considered.

The force acting on the particle is given by

$$F_{p_x} = 3\pi\mu_g d_p(u - V_x), \qquad \text{(B-2)}$$

which is Stokes drag law. Combining Equations (B-1) and (B-2) yields

$$m_p \frac{dV_x}{dt} - 3\pi\mu_g d_p(u - V_x) = 0. \qquad \text{(B-3)}$$

The term $(u - V_x)$ in Equation (B-3) is the relative velocity between the particle and the gas. As the gas accelerates through the nozzle, the particles are accelerated in turn by the gas stream. The absolute velocity of the particle, V_x, is at all times less than the absolute velocity of the gas, u, such that the velocity of the particle relative to the gas stream is always rearward or directed toward the combustion chamber. As the absolute gas velocity, u, becomes very high in the divergent portion of the nozzle, the absolute velocity of the particle, V_x, may be sufficiently low that, at some location in the nozzle, the particle becomes supersonic with respect to the gas surrounding it. The central point of the detached shock wave associated with this supersonic flow thus trails the particle in the exhaust nozzle. The condition wherein the particle is supersonic with respect to the gas is discussed when the approximate solution is considered.

For the one-dimensional steady-state condition being studied:

$$\frac{dV_x}{dt} = V_x \frac{dV_x}{dx},$$

and for spherical particles:

$$m_p = \rho_p \frac{\pi d_p^3}{6}.$$

Equation (B-3) now becomes

$$V_x \frac{dV_x}{dx} - \frac{18\mu_g}{\rho_p d_p^2}(u - V_x) = 0, \qquad \text{(B-4)}$$

which can be nondimensionalized by multiplying through by L/u_F^2 to yield

$$\frac{V_x}{u_F}\frac{d(V_x/u_F)}{d(x/L)} - \frac{18\mu_g L}{\rho_p d_p^2 u_F}\left(\frac{u}{u_F} - \frac{V_x}{u_F}\right) = 0. \qquad \text{(B-5)}$$

Let:

$$V' = V_x/u_F$$

$$u' = u/u_F$$

$$x' = x/L$$

$$\alpha = \frac{18\mu_g L}{\rho_p d_p^2 u_F},$$

whereupon Equation (B-5) becomes

$$V'\frac{dV'}{dx'} + \alpha V' = \alpha u'. \qquad \text{(B-6)}$$

The viscosity, μ, is a function of gas temperature, and hence of x'. However, in order to simplify the equation, μ_g will be assumed constant and equal to the average viscosity. Hence, α is not a function of x'.

Exact Solutions

Equation (B-6) is, in general, nonlinear and of degree greater than one in x'. Solutions to the equation may be obtained for a particular nozzle geometry and a particular value of α by means of a computing machine. The sole boundary condition required is the particle velocity at x' equal to zero.

Closed-form solutions to Equation (B-6) may be readily obtained for two special cases: (1) where u' is linear in x', and (2) where u' is constant The first case corresponds to the condition where

$$u = u_E + (u_F - u_E)\, x' \tag{B-7}$$

and α is assumed to be constant.

In order to obtain a solution of Equation (B-6) for the first case, the substitution $V_x = \frac{dx}{dt}$ is made The equation is then second order and linear for the condition of Equation (B-7) with the boundary conditions at

$$t' = 0,\ x' = 0 \text{ and } \frac{dx'}{dt'} = V'_E,$$

where

$$t' = \frac{t u_F}{L} .$$

The transformed equation is

$$\frac{d^2x'}{d(t')^2} + \alpha \frac{dx'}{dt'} - (1 - u'_E)\, \alpha x' = \alpha u'_E . \tag{B-8}$$

The solution to Equation (B-8) is

$$x' = \left[\frac{\beta - 1}{2\beta} \frac{u'_E}{1 - u'_E} - \frac{V'_E}{\alpha\beta} \right] \exp\left[- \frac{\alpha}{2}(1 + \beta)t' \right] \tag{B-9}$$

$$+ \left[\frac{\beta + 1}{2\beta} \frac{u'_E}{1 - u'_E} + \frac{V'_E}{\alpha\beta} \right] \exp\left[\frac{\alpha}{2}(\beta - 1)t' \right] - \frac{u'_E}{1 - u'_E},$$

where

$$\beta = \sqrt{1 + \frac{4}{\alpha}(1 - u'_E)} .$$

Equation (B-9) may be differentiated once to obtain V', the result being

$$V' = \frac{1}{2\beta} \left\{ \left[V'_E(\beta + 1) - 2u'_E \right] \exp\left[- \frac{\alpha}{2}(\beta + 1)t' \right] \right. \tag{B-10}$$

$$\left. + \left[V'_E(\beta - 1) + 2u'_E \right] \exp\left[\frac{\alpha}{2}(\beta - 1)t' \right] \right\} .$$

Cross-plotting Equations (B-9) and (B-10) yields graphically V' as a function of x'. This solution is important if a linear gas velocity distribution is approached in the nozzle, or if the gas velocity distribution can be approximated by a series of linear functions, each function being applicable to a small range of x'.

A solution to Equation (B-6) can also be obtained for the second case,

where

$$u' = \text{constant}.$$

This case corresponds to the conditions of a constant-area duct. The constant will be chosen equal to unity. The solution to Equation (B-6) for this case is

$$\frac{(1 - V') \exp V'}{(1 - V'_E) \exp V'_E} = \exp(-\alpha x'). \tag{B-11}$$

An Approximate Solution

An approximate solution to Equation (B-6) is to be obtained. Equation (B-6) is integrated as follows:

$$\int_{V' = V'_E}^{V' = V'_F} V' dV' + \int_{x' = 0}^{x' = 1} \alpha V' dx' = \int_{x' = 0}^{x' = 1} \alpha u' dx'. \tag{B-12}$$

As before, the viscosity variation is neglected, and therefore α is not a function of x', and Equation (B-12) becomes

$$\frac{(V'_F)^2}{2} - \frac{(V'_E)^2}{2} + \alpha \int_0^1 V' dx' = \alpha \int_0^1 u' dx'. \tag{B-13}$$

It may be observed that

$$\int_0^1 V' dx' = V'_{\text{average}}.$$

Let $V'_{\text{average}} = \frac{V'_F}{2}(1 + \epsilon)$, where ϵ may vary from -1 to +1. Furthermore,

$$\int_0^1 u' dx'$$

may be obtained from nozzle geometry.

Let

$$\psi = 2\alpha \int_0^1 u' dx' + (V'_E)^2. \tag{B-14}$$

The resulting equation, after rearrangement, and noting that only positive values of V_F' are admissible, may be expressed as

$$\frac{V_F'}{\alpha} = -\frac{1+\epsilon}{2} + \sqrt{\frac{1+\epsilon^2}{2} + \frac{\psi}{\alpha^2}} \qquad \text{(B-15)}$$

Figure B-1 is a plot of V_F'/α as a function of ψ/α^2 for $\epsilon = -1$, 0, and +1. If $K/\alpha^2 > 40$, then the effect of ϵ can be considered to be negligible. If, furthermore, $(V_E')^2$ is negligible compared with

$$2\alpha\int_0^1 u'dx',$$

then

$$\frac{\psi}{\alpha^2} = \frac{1}{9}\left(\frac{dp}{L}\right)\left(\frac{\rho p}{\rho g}\right)\left(\frac{u_{avg}\rho g d_p}{\mu}\right) \qquad \text{(B-16)}$$

The term in the last bracket of Equation (B-16) is the average Reynolds number with respect to the particle diameter. $\psi/\alpha^2 > 40$ implies, for the conditions in a rocket exhaust, a Reynolds number on the particle of the order of 600, or more. It is recalled that Stokes drag law was assumed in the derivation of the differential equation. Stokes drag law is valid for Reynolds numbers up to the order of unity and is only approximate for Reynolds numbers up to about 600. Nevertheless, a simple modification can be made to take account of this deviation in the approximate solution.

Recalling that

$$V_F' \approx \sqrt{\psi}$$

when $\psi/\alpha^2 > 40$, algebraic manipulation gives

$$\frac{1}{2} m_p V_F^2 = \int_0^L 3\pi\mu d_p u dx. \qquad \text{(B-17)}$$

Thus, for $\psi/\alpha^2 > 40$, and neglecting the kinetic energy of the particle at the entrance, the kinetic energy of the particle at the nozzle exit can be computed directly on the basis of the gas velocity. The integrated form of the exact equation is

$$\frac{1}{2} m_p \left(V_F^2 - V_E^2\right) = \int_0^L 3\pi\mu d_p (u - V)\, dx, \qquad \text{(B-18)}$$

where, when ψ/α^2 is large, it can be assumed that $u \gg V$, and V can be neglected. When $\epsilon = -1$, $V = 0$ up to the exit and $V_F = \sqrt{\psi}$ exactly.

The result of the exact analysis may be stated, therefore, as follows: The increase in kinetic energy of the particle equals the drag force integrated over the nozzle length. Neglecting the initial kinetic energy of the particle,

$$(KE)_F = \int_0^L F dx, \qquad \text{(B-19)}$$

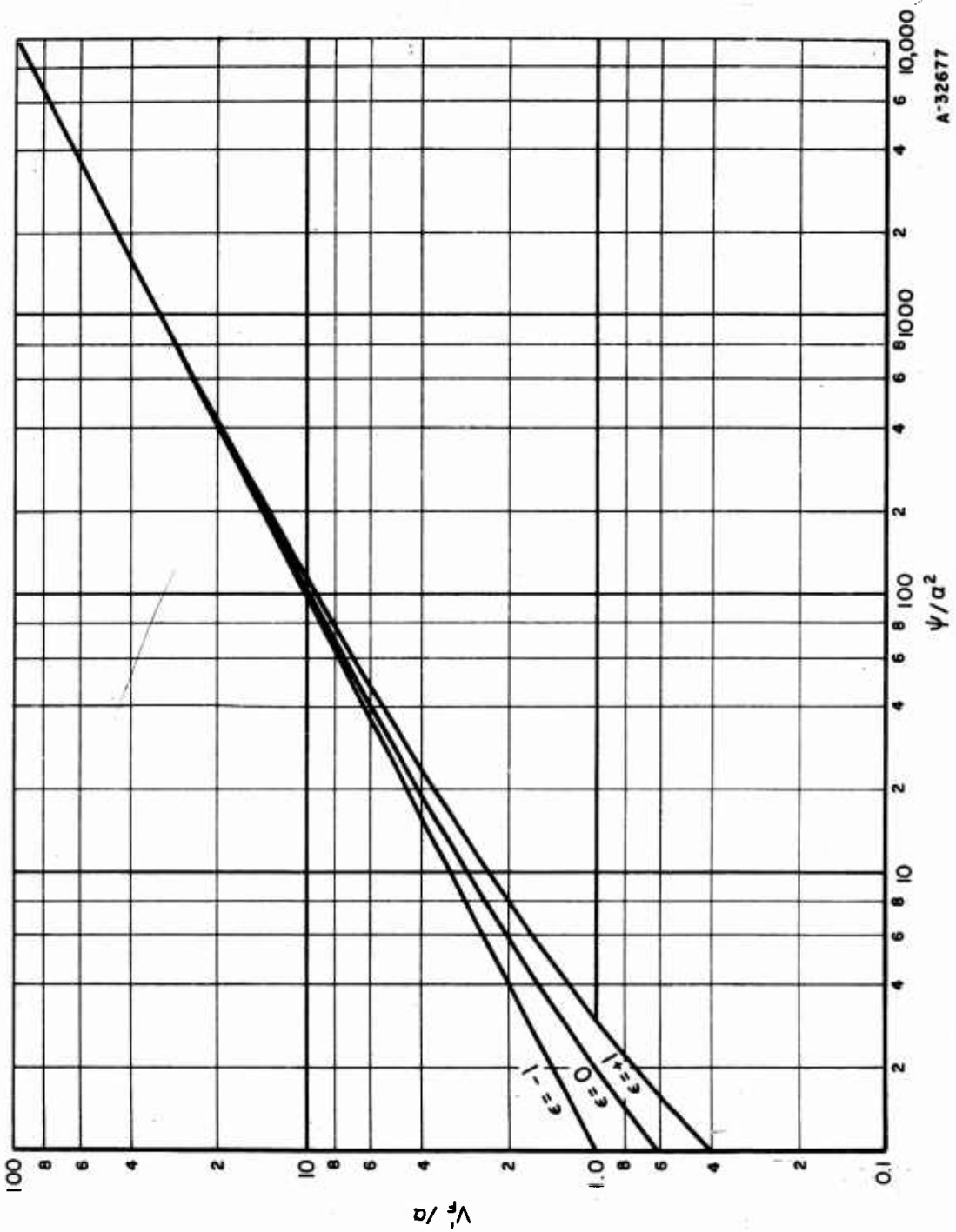

FIGURE B-1. SIGNIFICANCE OF ϵ WITH RESPECT TO PARTICLE VELOCITY AS ψ/α VARIES

where F is the drag force on the particle. The analysis could have begun with the exact energy relationship in differential form. Nonlinearities in the equation would have been found, just as was found when starting with the momentum equation.

It should be noted that a more general drag law than Stokes law may be substituted into Equation (B-19). A valid drag law exists for Reynolds numbers up to 1000 in subsonic flow:

$$\frac{C_D Re_p}{24} = 1 + \frac{Re_p^{\frac{2}{3}}}{6}$$

As was pointed out previously, it is possible for supersonic relative velocities to occur in the rocket-engine exhaust system. A supersonic drag law, such as the one obtained by Kane*, can be used in Equation (B-19). The equation obtained by Kane is applicable to spheres in the range of Reynolds numbers from 1 to 1000 in supersonic flow. It may be written as

$$C_D = \frac{8}{\pi}\left[K_D^1 + \frac{0.52}{\sqrt{Re_2}}\right]\left[1 + \frac{1}{\sqrt{Re_2}}\right]^2,$$

where C_D is the drag coefficient, Re_2 is the Reynolds number based on sphere diameter and conditions within the shock layer, and K_D^1 is a constant that variers slightly with Mach number. For the Mach-number range from 1 to 1.5, the value of K_D^1 was found by Charters and Thomas** to be approximately 0.35. This value of K_D^1 was used.

The ratio of the Reynolds number on the upstream side of the shock wave that trails the particle to that on the downstream side was next calculated for M = 1.5. The resulting value was 0.924 for an assumed specific-heat ratio, γ, of 1.2. Thus, the Reynolds-number ratio varies between 1 at M = 1 and 0.924 at M = 1.5. The ratio was assumed to be 1. The equation presented by Kane was then expanded and the drag coefficient was calculated for a Reynolds number of 300. The first term in the expansion was (0.35) (8/π), the second term was (0.0705) (8/π), and subsequent terms were considered to be negligible. The drag coefficient was then assumed to be constant and equal to (0.42) (8/π). This is in agreement with Kane's result, which shows C_D to be approximately constant for a Reynolds number greater than 130. Kane obtained a value of (0.45) (8/π), based on a value of 0.38 for K_D^1. The drag force may now be written as

$$F_p = 0.42\gamma\tilde{p}M^2 d_p^2.$$

Computations of Particle Velocities in the 3.5 AHT Exhaust Jet

The results of computations of the velocities of aluminum oxide particles in the 3.5 AHT exhaust jet are presented now. After being accelerated by the gases within the exhaust nozzle, the particles are additionally accelerated in the 6-inch space between the nozzle exit and the test specimens. It is assumed herein that this free expansion is at a constant gas velocity; hence, the flow in the space between the nozzle exit and the test specimen is equivalent to that of frictionless flow in a constant-area duct.

*Kane, E. D., "Sphere Drag Data at Supersonic Speeds and Low Reynolds Numbers", Journal of the Aeronautical Sciences, Vol 18, April, 1951, p 259.

**Charters, A. C., and Thomas, R. N., "The Aerodynamic Performance of Small Spheres From Subsonic to High Supersonic Velocities", Journal of the Aeronautical Sciences, Vol 12, October, 1945, p 468.

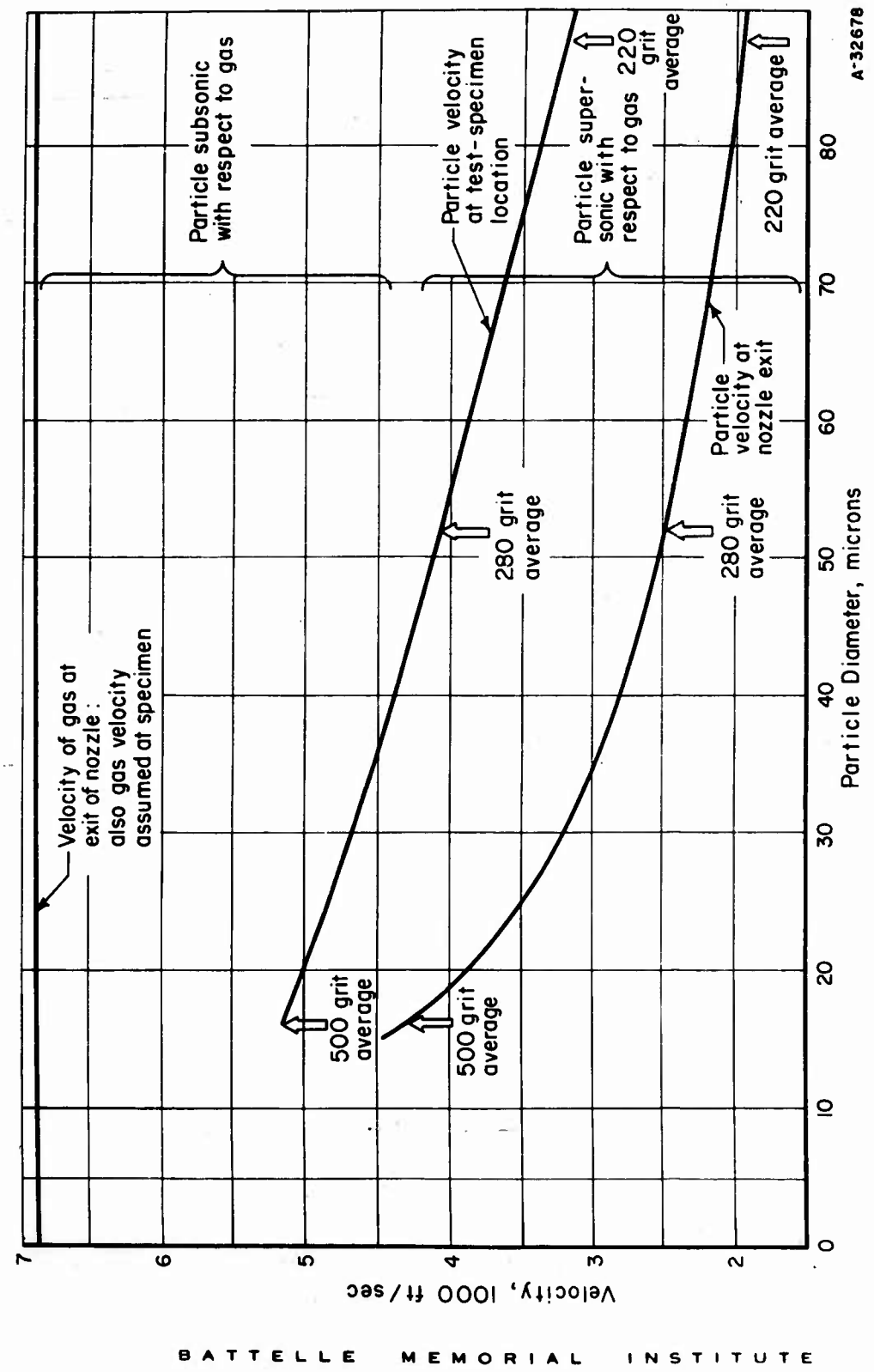

FIGURE B-2. VARIATION OF PARTICLE VELOCITY WITH PARTICLE DIAMETER IN THE 3.5 AHT EXHAUST JET

APPENDIX C

MOTION OF A PARTICLE IN THE SHOCK LAYER IN THE MODEL STUDY

APPENDIX C

MOTION OF A PARTICLE IN THE SHOCK LAYER IN THE MODEL STUDY

The objective in studying the particle motion in the shock layer is to determine what fraction of the particles will reach the body, that is, the impaction efficiency of the particles. This appendix develops, from theoretical considerations, a set of equations that determine the minimum possible value of the impaction efficiency. The case of alumina particles impinging upon test specimens is considered in detail. The results indicate, for example, that the impaction efficiency is between 92 and 100 per cent for all particles used in the first series of tests.

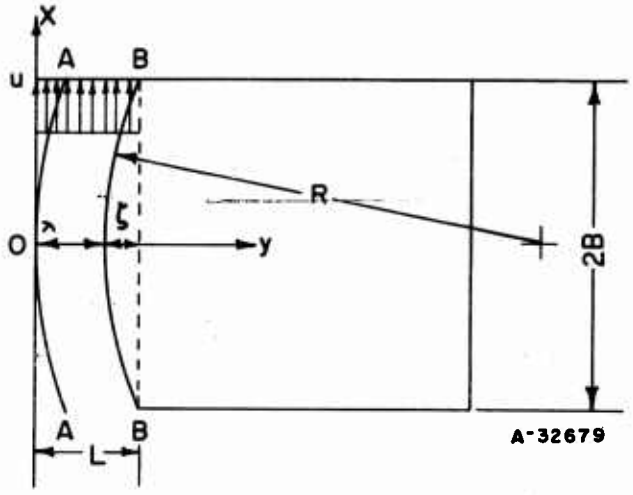

FIGURE C-1. NOSE-CONE TEST SPECIMEN AND BOW SHOCK WAVE

Impaction Efficiency for Test Specimen

Figure C-1 shows the test specimen used in the first series of tests, together with the detached bow shock wave, denoted by A-A. The shock-detachment distance at the stagnation point is represented by λ.

The minimum value of the impaction efficiency for the test specimen is found from the following considerations. First, the fluid conditions between the shock and the body are chosen such that any particle entering the shock layer will experience the maximum possible deflection, thereby giving the minimum impaction efficiency. In order to produce the maximum particle deflection, the air velocity in the shock layer is assumed to have no component in the y direction and a uniform velocity in the x direction denoted

by u, as shown in Figure C-1. Secondly, in order to simplify the mathematics, the curved surface of the test specimen is replaced by Plane B-B and the shock wave is replaced by the x-axis. By choosing these plane surfaces as the hypothetical boundaries of the shock wave and the body, it is apparent that any particle impinging on the plane surface must also strike the curved surface. In addition, the particle traveling through the hypothetical shock layer will be deflected more than the particle in the real shock layer because of the increased thickness of the shock layer. Therefore, it is assured that the impaction efficiency of the hypothetical surface must be less than the impaction efficiency of the actual surface.

Figure C-2 shows a particle at Point P in the shock layer. The particle is traveling with velocity V oriented at an angle θ from the gas velocity u. The gas velocity is assumed to be uniform and parallel to the x-axis. The components of the particle velocity in the x and y directions are denoted by V_x and V_y, respectively. The velocity of the particle with respect to the gas, V_r, is at an angle α from the y-axis. The drag force acting on the particle is represented by F and is shown acting in a direction opposite to the relative velocity. The components of the drag force are shown as F_x and F_y. The initial conditions are that the particle enters the shock layer parallel to the y-axis with a velocity V_s.

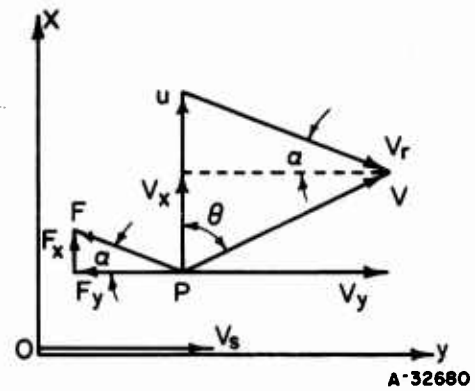

FIGURE C-2. FORCE AND VELOCITY DIAGRAM FOR PARTICLE IN SHOCK LAYER

The particle is assumed to be traveling supersonically with respect to the gas at all times. This assumption will be justified in the following analysis. The drag force acting on the particle is given by

$$F = \frac{1}{2} C_D A_p \rho_g V_r^2 \quad . \qquad \text{(C-1)}$$

Referring to Figure C-2, the relative velocity is given by

$$V_r^2 = u^2 + V^2 - 2uV\cos\theta \quad , \qquad \text{(C-2)}$$

or

$$V_r^2 = u^2 + V_x^2 + V_y^2 - 2uV_x = (u-V_x)^2 + V_y^2 \quad . \qquad \text{(C-3)}$$

The drag force in the y direction is

$$F_y = -F\cos\alpha = -F\frac{V_y}{V_r} = -\frac{1}{2} C_D A_p \rho_g V_r V_y \quad . \tag{C-4}$$

Similarly, the drag in the x direction is given by

$$F_x = F\sin\alpha = F\frac{u-V_x}{V_r} = \frac{1}{2} C_D A_p \rho_g V_r (u-V_x) \quad . \tag{C-5}$$

The equations of motion in the x and y directions are, respectively,

$$\frac{1}{2} C_D A_p \rho_g V_r (u-V_x) = m_p \frac{dV_x}{dt} \tag{C-6}$$

$$-\frac{1}{2} C_D A_p \rho_g V_r V_y = m_p \frac{dV_y}{dt} \quad . \tag{C-7}$$

Dividing Equation (C-6) by Equation (C-7) and rearranging gives

$$\frac{dV_x}{V_x - u} = \frac{dV_y}{V_y} \quad . \tag{C-8}$$

Integrating, and using the initial condition that $V_x = O$ when $V_y = V_s$, gives

$$V_y = \frac{V_s}{u}(u-V_x) \quad . \tag{C-9}$$

Inserting Equations (C-3) and (C-9) into Equation (C-7) permits the equation of motion to be expressed in integrable form:

$$\frac{dV_y}{dt} = -kV_y^2 \sqrt{1 + (u/V_s)^2} \quad , \tag{C-10}$$

where

$$k = \frac{C_D A_p \rho_g}{2m_p} = \frac{3}{4} \frac{\rho_g}{\rho_p} \frac{C_D}{d_p} \quad . \tag{C-11}$$

Integrating this expression and inserting the initial conditions gives

$$V_y = \left(\frac{V_s}{1 + k\, V_s t \sqrt{1 + (u/V_s)^2}} \right) \quad . \tag{C-12}$$

The value of V_x is found by combining Equations (C-9) and (C-12) to give

$$V_x = u - \frac{u}{1 + kV_s t \sqrt{1 + (u/V_s)^2}} \quad . \tag{C-13}$$

Integrating Equations (C-12) and (C-13) and combining with the initial conditions gives

$$y = \frac{1}{k\sqrt{1 + (u/V_s)^2}} \log\left(1 + kV_s t\sqrt{1 + (u/V_s)^2}\right) \qquad \text{(C-14)}$$

$$x = ut - \frac{u/V_s}{k\sqrt{1 + (u/V_s)^2}} \log\left(1 + kV_s t\sqrt{1 + (u/V_s)^2}\right) \qquad \text{(C-15)}$$

The trajectory of the particle may be found by eliminating t from Equations (C-14) and (C-15), which yields

$$x = \frac{u/V_s}{k\sqrt{1 + (u/V_s)^2}}\left[e^{yk\sqrt{1 + (u/V_s)^2}} - yk\sqrt{1 + (u/V_s)^2} - 1\right] \qquad \text{(C-16)}$$

Similarly, the velocity components may be written in terms of y:

$$V_y = V_s\, e^{-yk\sqrt{1 + (u/V_s)^2}} \qquad \text{(C-17)}$$

$$V_x = u\left[1 - e^{-ky\sqrt{1 + (u/V_s)^2}}\right] \qquad \text{(C-18)}$$

The original assumption that the particle velocity relative to the gas stream, V_r, remains supersonic can now be examined. Substitution of Equations (C-17) and (C-18) into Equation (C-3) gives the relative velocity as

$$V_r = V_s\sqrt{1 + (u/V_s)^2}\; e^{-yk\sqrt{1 + (u/V_s)^2}} \qquad \text{(C-19)}$$

Thus, it is seen that the relative velocity decreases as the axial displacement increases, so that V_r is smallest at y = L. The parameters y and k appearing in Equation (C-19) are evaluated below.

Evaluation of Parameters for First Test Series

Referring to Figure C-1, the total separation distance between the hypothetical shock wave and target is given by

$$L = \lambda + \zeta \quad , \qquad \text{(C-20)}$$

which overestimates the true detachment distance, thereby assuring a minimum impaction efficiency and minimum relative velocity. From the geometry of the figure, it is seen that

$$\zeta = R - \sqrt{R^2 - B^2} = 0.20 \text{ inch} \quad .$$

The detachment distance at the stagnation point of the curved surface, λ, is 0.15 R or 0.39 inch*. Substitution of these values into Equation (C-20) gives L = 0.59 inch.

The parameter k is defined by Equation (C-11). The gas density in the shock layer in the first series of tests was about 2.2×10^{-3} slug/ft^3, and the alumina particle density about 8.0 slugs/ft^3. The drag coefficient for a spherical particle can be taken as a constant equal to unity in the transonic and supersonic regions. Using these values, the value of k is found to be $5.24/d_p$ inches^{-1}, where d_p represents the particle diameter in microns. Substitution of the above values for k and L into Equation (C-19) and rearranging gives

$$\left(\frac{V_r}{V_s}\right)_{y=L} = \sqrt{1 + (u/V_s)^2}\; e^{-\frac{3.09}{d_p}\sqrt{1 + (u/V_s)^2}} \quad . \qquad \text{(C-21)}$$

This equation is used below to determine the correctness of the original assumption that the relative velocity always remains supersonic.

Figure C-3 shows the relationship between V_r/V_s and u/V_s as stated in Equation (C-21) for a range of particle sizes. The values of the initial particle velocity, V_s, are found in Figure B-2 of Appendix B. For the particle sizes considered, these values are:

Particle Size, microns	V_s, ft/sec
5	6000
16.4	5200
52.2	4100
87.8	3160

Physically, the velocity of the gas stream in the shock layer is limited to sonic velocity. The velocity of sound in the shock layer is considered to be a constant determined by the gas temperature at the stagnation point of 3740 R and a ratio of specific heats of 1.20. The sonic velocity corresponding to these conditions in the shock layer is 2780 ft/sec. Therefore, u must be less than 2780 ft/sec, and for the 5-micron particle, for example, then $u/V_s < 2780/6000 = 0.463$. This maximum value of u/V_s and the corresponding values for the other particle sizes are noted on Figure C-3 by the dashed curve. Similarly, for V_r to be supersonic, then $V_r/V_s > 0.463$ for the 5-micron particle. From Figure C-3 it is seen that V_r is always supersonic for all particles considered, regardless of the value of u. Therefore, in the calculations, any subsonic value of u can be used, as long as u is also larger than the maximum true value of u in the region, in order to assure the maximum particle deflection, that is, the minimum

*Ting-Yi Li and Geiger, R. E., "Stagnation Point of a Blunt Body in Hypersonic Flow", Journal of the Aeronautical Sciences, January, 1957.

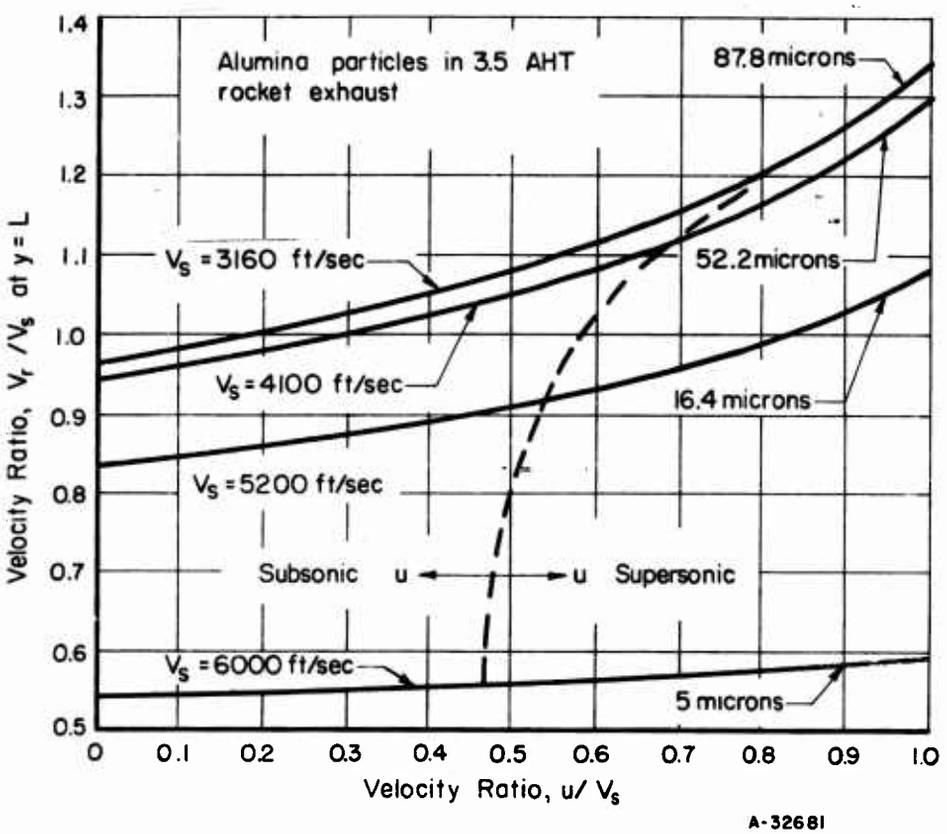

FIGURE C-3. RELATIONSHIP BETWEEN GAS VELOCITY AND RELATIVE VELOCITY OF THE PARTICLE IN THE SHOCK LAYER

impaction efficiency. Taking u as being equal to sonic velocity, and denoting it by u*, the corresponding values of u^*/V_s for the various particle sizes are:

Particle Size, microns	u^*/V_s	$\sqrt{1 + (u^*/V_s)^2}$	k, in.$^{-1}$	$k\sqrt{1 + (u^*/V_s)^2}$, in.$^{-1}$
5.0	0.463	1.102	1.047	1.152
16.4	0.534	1.134	0.3270	0.3710
52.2	0.678	1.208	0.1005	0.1210
87.8	0.880	1.332	0.0596	0.0795

where the values of k and $\sqrt{1 + (u^*/V_s)^2}$ are tabulated for convenience in the subsequent calculation.

Calculation of Impaction Efficiency

The minimum impaction efficiency, η, is defined by

$$\eta_{min} = \left(\frac{B - x_{max}}{B}\right)^2 = 1 - \left(\frac{x_{max}}{B}\right)^2 , \qquad \text{(C-22)}$$

where B is the cross-sectional radius of the target, as shown in Figure C-1. The impaction efficiency is evaluated from Equation (C-16), which gives

$$\frac{x_{max}}{B} = \frac{u^*/V_s}{kB\sqrt{1 + (u^*/V_s)^2}} \left[e^{kL\sqrt{1 + (u^*/V_s)^2}} - kL\sqrt{1 + (u^*/V_s)^2} - 1 \right], \qquad \text{(C-23)}$$

where the values B = 1.0 inch and L = 0.59 inch are to be taken from Figure C-1 and where k and u^*/V_s are taken from the preceding tabulation.

Figure C-4 shows the minimum impaction efficiency as determined by Equations (C-22) and (C-23) for a range of particle sizes. The curve applies only to the test specimen shown in Figure C-1 and also applies only to alumina particles injected into the 3.5 AHT rocket exhaust. For the 16.4-micron particles used in the first series of tests, the curve shows that the impaction efficiency is above 92.2 per cent. The 52.2- and 87.8-micron particles have an impaction efficiency above 97 per cent.

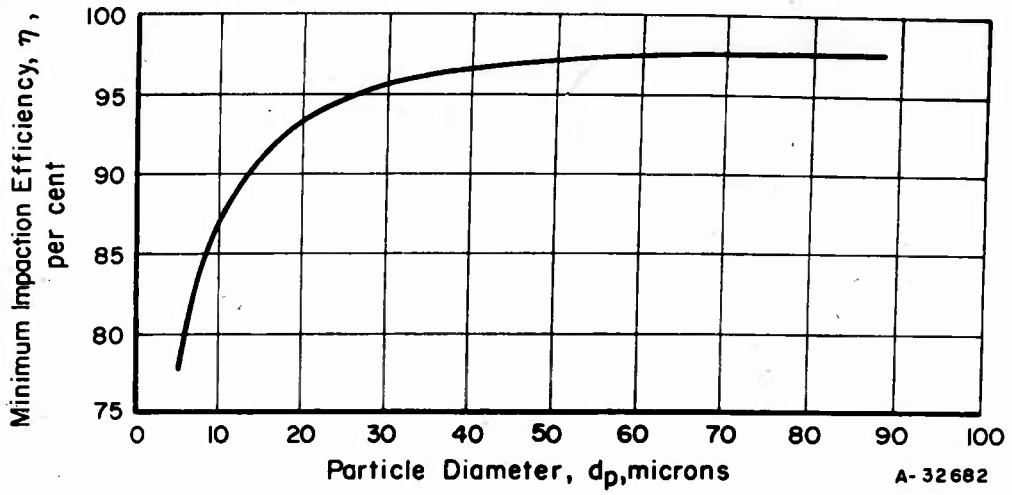

FIGURE C-4. MINIMUM IMPACTION EFFICIENCY FOR ALUMINA PARTICLES IN 3.5 AHT ROCKET EXHAUST

Possible Refinements of the Calculations

The accuracy of the determination of the minimum impaction efficiency may be improved by assuming other values for the gas velocity, u, which are more representative of the true physical problem. As shown previously, the relative velocity, V_r, remains supersonic for all values of u. Therefore, as long as u is equal to or greater than the value of u occurring in the actual problem, the impaction efficiency will be a minimum. The average value of the true gas velocity, u, can be found by consideration of the mass continuity relations for the shock-layer region. Refinements of this nature are not considered significant for the analysis of test-specimen exposure.

UNCLASSIFIED

UNCLASSIFIED